University of Southern Queensland
Faculty of Engineering & Surveying

Internal Combustion Engine Heat Transfer-Transient Thermal Analysis

A thesis submitted by

Abdalla Ibrahim Abuniran Agrira

B.Sc., M.Sc.

in fulfilment of the requirements for the degree of

Doctor of Philosophy

Submitted: May, 2012

To my mother and my Siblings,

To my wife, my son and my little daughter.

Acknowledgments

First and foremost I would like to express my gratitude to Allah (God) for providing me the blessings to complete this work. I also would like to offer my profound gratitude to the Libyan government through the Libyan Embassy in Canberra for giving me the sponsorship to complete my studies and to pursue my dreams.

Thanks for everyone who helped me in completing this work. I take immense pleasure to express my sincere gratitude to my advisor, Prof. David R. Buttsworth, who helped in every step of the way and for the continuous support of my study, for his patience, motivation and the guidance. I also would like to thank A.Prof Talal Yusaf for his help and support in the early stage of my study.

I wish to extend my gratitude to the mechanical workshop technicians Mr Chris Galligan and Mr Brian Aston for their help and kind cooperation in making and fabricating some of the tools used in my experiments. I sincerely acknowledge my friend and colleague Mr. Mior Azman Said for his support and help in my research work. I also extend my thanks to my colleague Dr. Ray Malpress for his support, guidance and the valuable suggestions in many technical matters. I also would like to thank Mr. Sudantha Balage, Mr. Dean Beliveau and Dr. Paul Baker for their help and technical advices. I also would like to thank Mrs. Avril Baynes for the editorial support for my dissertation and the valuable comments and suggestions. Many thanks to Ms. Sue Stapleton for her generous hospitality on first arriving in Australia.

My friends and colleagues Mr. Abdurazaq Mustafa and Mr. Anwar Saqr had always been there with a helping hand throughout the period of my work. My sincere gratitude for your help, co-operation and hustle during the tenure of my work.

Finally, it is with immense pleasure I express my thankfulness to my family: my mother, my wife, my Siblings and my little kids for all the support and motivation in all my efforts during the course of my work.

Abdalla Agrira

University of Southern Queensland

May 2012

Certification of Dissertation

I certify that the ideas, designs and experimental work, results, analyses and conclusions set out in this dissertation are entirely my own effort, except where otherwise indicated and acknowledged.
I further certify that the work is original and has not been previously submitted for assessment in any other course or institution, except where specifically stated.

Abdalla Agrira

W0076717

_____

Signature of Candidate

_____

Date

ENDORSEMENT

_____

Signature of Supervisor/s

_____

Date

Abstract

Heat transfer to the cylinder walls of internal combustion engines is recognized as one of the most important factors that influences both engine design and operation. Research efforts concerning heat transfer in internal combustion engines often target the investigation of thermal loading at critical combustion chamber components. Simulation of internal combustion engine heat transfer using low-dimensional thermodynamic modelling often relies on quasi-steady heat transfer correlations. However unsteady thermal boundary layer modelling could make a useful contribution because of the inherent unsteadiness of the internal combustion engine environment.

In this study, a computational and experimental study is presented. The experiments are performed on a spark-ignition, single-cylinder engine under motored and fired conditions. In the present study, decoupled simulations are performed, in which quasi-steady heat transfer models are used to obtain the gas properties in the core region. A scaled Eichelberg's model is used in the simulation of the motored test under wide open and fully closed throttle settings. In the fired case the scaled Woschni's model was used. The scaling factor is used to achieve a good agreement between measured and simulated pressure histories.

An unsteady heat transfer model based on the unsteady thermal boundary layer is presented in this study. Turbulent kinetic energy in the core of the cylinder is modelled by considering the balance between production and dissipation terms as suggested by previous authors. An effective variable thermal conductivity is

applied to the unsteady model with different turbulent Prandtl number models and turbulent viscosity models, and a fixed value is assumed for the thermal boundary layer thickness. The unsteady model is run using the gas properties identified from the quasi-steady simulation.

The results from the quasi-steady modelling showed that no agreement was achieved between the measured and the simulated heat flux using the scaled Eichelberg's model for the motored case and the scaled Woschni's model for the fired case. A significant improvement in the simulation of the heat flux measurements was achieved when the unsteady energy equation modelling of the thermal boundary layer was applied. The simulation results have only a small sensitivity to the boundary layer thickness. The simulated heat flux using the unsteady model with one particular turbulent Prandtl number model, agreed with measured heat flux in the wide open throttle and fully closed throttle cases, with an error in peak values of about 6 % and 35 % for those cases respectively. In the fired case, a good agreement was also observed from the unsteady model and the error in the peaks between the measured and the simulated heat flux was found to be about 9 %.

The turbulent Prandtl number and turbulent viscosity models are derived from quasi-steady flow experiments and hence their general applicability to the unsteady internal combustion engine environment remains uncertain. The thermal boundary layer thicknesses are significant relative to the internal combustion engine clearance height and therefore, the assumption of an adiabatic core is questionable. Investigation of a variable thermal boundary layer thickness and more closely coupled simulation to account for heat loss from the entire volume of the gas should be targeted in the future.

Associated Publications

During the course of this thesis, some journal and conference papers were produced. These publications presented the major results discovered during the course of this thesis. The papers are listed as follows:

Journal Papers

[1] A. Agrira, D. Buttsworth, and M. Said, "Instantaneous Heat Flux Simulation of a Motored S.I. Engine: Unsteady Thermal Boundary Layer with Variable Turbulent Thermal Conductivity" , Submitted to the ASME Journal of Heat Transfer.

[2] D. Buttsworth, A. Agrira, R. Malpress, and T. Yusaf, "Simulation of instantaneous heat transfer in spark ignition internal combustion engines: unsteady thermal boundary layer modelling," *Journal of Engineering for Gas Turbines and Power*, vol. 133, pp. 022802, 2011.

Conference Papers

[1] A. Agrira, D. Buttsworth, and T. Yusaf, "Instantaneous heat flux simulation of si engines: comparison of unsteady thermal boundary layer modelling with experimental data," *3rd International Conference on Energy and Environment, 2009 (ICEE 2009)*, Malacca, Malaysia, Dec. 2009 pp. 12-19.

Contents

List of Figures

List of Tables

Abbreviations

AF	Air/Fuel ratio
ATDC	After Top Dead Centre
BDC	Bottom Dead Centre
BMEP	Break Mean Effective Pressure
BTDC	Before Top Dead Centre
CA	Crank Angle
DI	Direct Injection
FA	Fuel/Air ratio
FCT	Fully Closed Throttle
IDI	Indirect Injection
TDC	Top Dead Centre
WOT	Wide Open Throttle

Nomenclature

Notation

A	surface area
a	constant
B	cylinder bore
b	constant
C_m	mean piston speed
c_p	specific heat at constant pressure
C_μ	constant
D	specific length
d	diameter
f_μ	damping function
h	heat transfer coefficient
k	thermal conductivity
k_t	turbulent thermal conductivity
K	turbulence kinetic energy
l	length scale
m	mass
N	engine speed
P	pressure
Pr	Prandtl's number
Pr_t	turbulent Prandtl's number
$\dot{Q}$	rate of heat generation per unit volume

q	heat flux
Re	Reynold's number
Re_t	turbulent Reynold's number
S	cylinder stroke
St	Stanton number
T	temperature
U_T	transport velocity
u	turbulent fluctuating velocity
$\acute{u}$	intensity of turbulence
V	volume
V_j	jet velocity
w	gas velocity

Greek symbols

α	thermal diffusivity
α_s	scaling factor
α^*	constant ($k-\omega$ model)
β^*	constant ($k-\omega$ model)
θ	crank angle
ω	angular speed
ω	specific dissipation rate ($k-\omega$ model)
ρ	density
ϵ	emissivity
ϵ	dissipation rate ($k-\epsilon$ model)
Δ	difference
ϕ	equivalence ratio the temperature ratio
ϕ	the temperature ratio ($\mathrm{T/T_\infty}$)
μ	dynamic viscosity
μ_t	turbulent dynamic viscosity
μ^+	the ratio of turbulent viscosity to molecular viscosity

ν	kinematic viscosity
ν_t	turbulent kinematic viscosity

Subscripts

b	burned gases
c	convection
cyl	cylinder
d	displacement
g	gas side
m	mean value
t	turbulent
u	unburned gases
w	wall side

Chapter 1

Introduction

1.1 Heat transfer in engines

In-cylinder heat transfer is a significant feature of internal combustion engines (ICEs) which affects engine performance and emissions. Measurements of heat transfer have been performed and models have been produced by a large number of researchers. The accuracy of predicting the wall heat transfer is required not only to calculate the heat transfer rate from the gas pressure and temperature data, but also necessary for the internal combustion engines to improve the overall engine simulation. The heat transfer process from the gases to the coolant through the combustion chamber wall has in general the three heat transfer elements. From the gases to the combustion chamber wall the heat is transferred mainly by convection with a contribution from radiation. The heat flux is conducted through the combustion chamber walls and then convected from the walls to the coolant, figure 1.1. In spark ignition engines the radiative component is less important than in compression ignition engine where the radiation heat transfer is significant due to the soot particles during the combustion process [3][10].

The total chemical energy that enters an engine in the fuel is converted into ap-

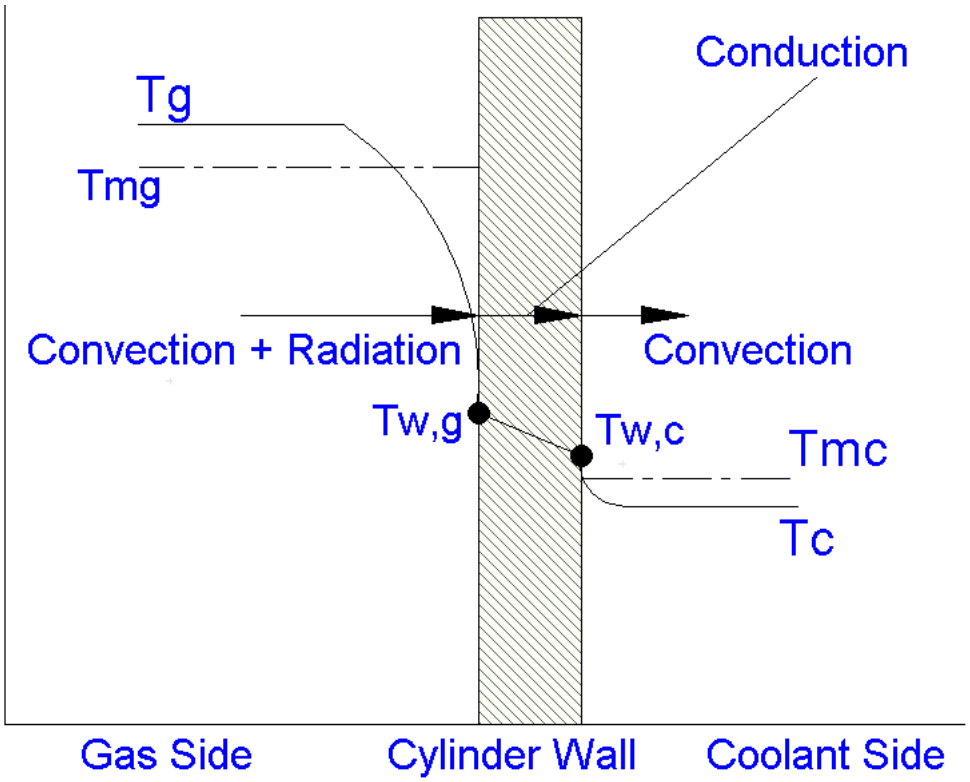

Figure 1.1: Schematic of temperature distribution and heat transfer modes across combustion chamber wall.

proximately 35 percent useful crankshaft work and about 30 percent is carried away from the engine in the exhaust flow. Approximately one third of the total energy is dissipated to the immediate surroundings via heat transfer. Gas temperatures in the combustion chamber during the combustion process may reach 2700 K. Metal components of the combustion chamber cannot tolerate this kind of temperature, which indicates that significant heat transfer must occur in the cylinders of internal combustion engines [2].

The heat transfer from the gases to the combustion chamber walls during the combustion period can reach approximately 10 MW/m^2. Components of the combustion chamber which are in contact with the high-temperature burned gases generally experience the highest heat flux. Thermal stress on these components must be kept under levels that would cause failure or serious engine damage. It is reported that temperature must be less than about 400 °C for cast iron and

300 °C for aluminium alloys [3]. However, the surface temperature of the piston and cylinder must generally be lower than 200 °C in order to avoid decomposition of the lubricating oil [2] [3].

For accurate simulation of engine performance and emission, robust models for in-cylinder heat transfer are essential. To date, in-cylinder convective heat transfer models have been largely empirical and the models are generally engine-specific and require 'tuning' for the different configurations to which they are applied.

1.2 Hypotheses

1. The majority of previous in-cylinder heat transfer models have emerged from steady-state, turbulent flow heat transfer correlations which are of limited applicability in the highly unsteady environment of ICEs.

2. New models for convective heat transfer in ICEs can be developed by accommodating the transient processes which occur in the engine environment.

3. These transient models will be more accurate and can be applied on a variety of engines with less reliance on empirical 'tuning' approaches used with earlier models.

1.3 Objectives of the thesis

The main objectives of this project are:

1. To implement and test the most popular heat transfer models obtained from the literature in an engine simulation program. An existing quasi one-dimensional spark ignition engine Matlab simulation program will be used to perform the simulation.

2. To contribute new experimental data on transient heat transfer in engines. For this contribution to be realised, the experimental work will focus on two objectives:

   (a) To design and construct fast response thermocouples suitable for measuring the transient surface temperatures of the engine cylinder wall.

   (b) To perform experiments on a spark ignition engine to aid the development of transient convective heat transfer models.

3. To deduce and develop a transient convective heat transfer model based on the experimental data. This will be implemented in a quasi one-dimensional spark ignition engine Matlab simulation program to check its reliability, accuracy and applicability for different engine configurations.

1.4 Outcomes of the study

The following outcomes are expected to be achieved from this study:

1. Development of a new unsteady convective heat transfer model which may be applicable for different engine configurations.

2. A credible implementation of existing and new convective heat transfer models in a quasi one-dimensional spark ignition engine Matlab simulation program.

1.5 Layout of the thesis

The research study presented in this thesis discovers experimentally and with the aid of numerical simulation the internal combustion engines heat transfer, and develops an unsteady heat transfer model based on the analysis of the unsteady

thermal boundary layer. The aim of this section is to make the thesis clear and easy to follow.

Chapter 2 is devoted to a literature review in order to provide the reader with an adequate overview of the fundamentals of internal combustion engines, engine heat transfer basics and some of the existing studies and heat transfer models and finally some of the available temperature and heat flux measurement methods in internal combustion engines.

In chapter 3, the derivation of the unsteady, one-dimensional heat conduction equation model developed in this study will be presented, and the turbulent thermal conductivity model which uses different models for the turbulent Prandtl number and the turbulent viscosity will also be discussed.

The implementation of some of the existing convective heat transfer models in a quasi one-dimensional spark ignition engine Matlab simulation program is presented in chapter 4. Some of the pressure and heat transfer data from the literature is assessed with the quasi one-dimensional simulation, and the heat flux from different quasi-steady heat transfer models and the unsteady thermal boundary layer model, with a constant turbulent thermal conductivity is investigated.

The engine specifications, the measuring devices, the thermocouple probe fabrication and the whole measurements procedure will be discussed in chapter 5.

In chapter 6, the experimental results for the pressure and heat flux obtained from the motored and fired tests, with the results from the simulation process using some of the existing quasi-steady heat transfer models, are presented.

Chapter 7 will demonstrate the unsteady model developed in this study with an effective variable thermal conductivity implemented in Matlab. This will be used to simulate the engine heat transfer to compare the measured heat flux with the predicted one, to illustrate the main findings and outcomes of this study.

In Chapter 8, a summary of this research study, overall conclusions and some recommendations for future work are presented.

Chapter 2

Literature Review

2.1 Introduction

The internal combustion engine is one of the most common and prefered sources of mechanical power in the modern world. This type of engine is used in different fields including but not limited to, transportation and electrical power generation. There are many designs and types of these engines, such as Spark Ignition (SI), Compression Ignition (CI) and Homogeneous Charge Compression Ignition (HCCI), however the spark ignition is the one of primary interest in this work. Heat transfer is an important issue for internal combustion engines, because it affects critical operating parameters of the internal combustion engines such as the in-cylinder pressure and temperature. However, engine heat transfer analysis and modelling are among the most complicated issues, because of the combustion process, the in-cylinder charge turbulence and the rapid motion of the piston within the combustion chamber. All of these factors contribute to the unsteadiness and local changes of the in-cylinder heat transfer. Moreover, heat transfer also has an effect on the engine exhaust emissions, because of the effect of the temperature changes on the NO_x formation. It was found that a reduction in the peak gas temperature of about (25-50 K) can halve the nitric oxides NO_x

emissions [11]. The examination of the engine's heat transfer and the thermal loading has a long and involved history. A variety of engine types and engine components have been tested and examined by a number of studies and research projects. In this chapter a brief introduction to the main concepts involved in the engines heat transfer will be presented, as well as some of the well known engine heat transfer correlations and review of the literature of some of the major studies that have been carried out on the engines heat transfer field. In addition, a review of engine heat transfer measurement techniques is included in this chapter.

2.2 Internal combustion engine - Fundamental concepts

The internal combustion engine (IC) is a heat engine that converts the chemical energy in the fuel into mechanical energy. The process of converting the chemical energy in the fuel is to convert it first to thermal energy by means of combustion with air inside the combustion chamber of the engine. This thermal energy increases the pressure and temperature of the gases within the combustion chamber. The high-pressure gas then expands against the mechanisms of the engine. This expansion is converted by the mechanical linkages of the engine to a rotating crankshaft, which is the output of the engine. The crankshaft is connected to a transmission and/or power train to transmit the rotating mechanical energy to the desired final use. There are two main types of internal combustion engines, namely two stroke cycle and four stroke cycle, based on the piston movement. In the four stroke engine, the piston experiences four movements over two engine revolutions for each cycle, whereas, in the two stroke engine the piston has only two movements over one revolution for each cycle. The four stroke engine is the primary interest of this study.

A diagram representing a four stroke internal combustion engine is shown in

figure 2.1. This type of engine uses the crankshaft and the connecting rod to generate a reciprocating motion in the piston. This motion is usually generated by the compression and expansion of the gases in the combustion chamber. The inlet and exhaust valves in the head of the engine allow the gas transfer process to take place, while the spark plug ignites the charge. The denoting 'four stroke' comes from the four major processes performed by these engines, which will be described later, after references [1] and [2].

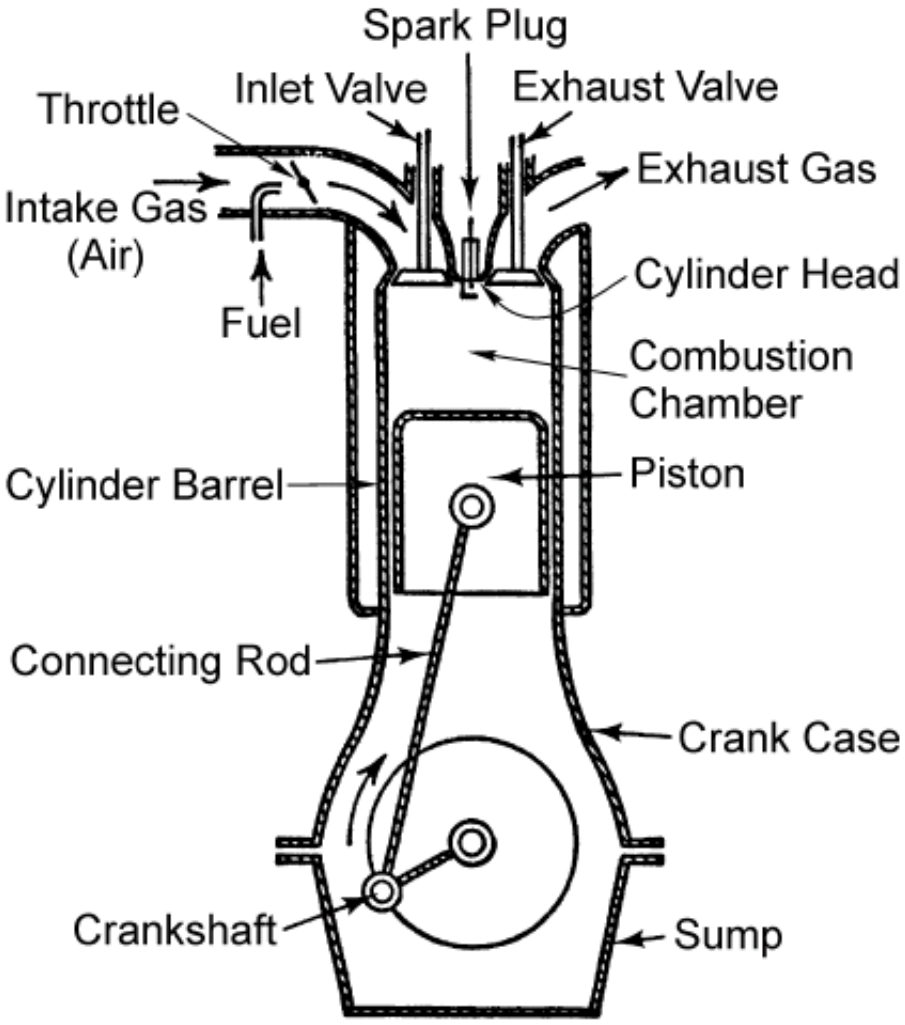

Figure 2.1: Diagram of a four stroke, spark ignition internal combustion engine. Figure taken from [1].

2.2.1 Internal combustion engine - Terminology

Some of the commonly used terms and abbreviations relating to internal combustion engines as used in this study are presented below.

Top Dead Centre: A position when the piston is at the furthest point away from the crankshaft. It also refers to the end of the compression and exhaust strokes. At this point the combustion chamber is at its smallest volume and it is abbreviated as TDC.

Bottom Dead Centre: A position when the piston is at the closest point to the crankshaft. This refers to the end of the intake and expansion strokes when the piston is at the bottom of its motion. The combustion chamber has its largest volume at this point and it is abbreviated as BDC.

Bore: Diameter of the cylinder or diameter of the piston face, which is about the same, with a very small clearance and it is abbreviated as B.

Stroke: The distance the piston moves from one extreme position to the other: TDC to BDC or BDC to TDC. It is abbreviated as S.

Clearance Volume: The minimum volume in the combustion chamber when the piston is at TDC.

Degrees Crank Angle: It refers to the position of the crank during the two revolution engine cycle. For the four stroke engine when the cycle covers two revolutions, the crank increases from 0° to 720° and then repeats. It is abbreviated as ° CA.

Compression Ratio: It refers to the amount of compression performed during the compression stroke and conversely the amount of expansion achieved during the expansion stroke. It is expressed as the ratio of the volume of the combustion chamber when the piston is at the BDC to the clearance volume. It is usually

abbreviated as r_c.

Volumetric Efficiency: Refers to the quantity of the actual air entering the cylinder during induction relative to the actual capacity of the cylinder. It is expressed as the ratio of the mass of air drawn to the mass of air that would exist in the cylinder when the piston is at BDC at a reference pressure and temperature.

Air-Fuel Ratio: It is the ratio of mass of air to mass of fuel input into engine and it is abbreviated as AF.

Fuel-Air Ratio: It is the ratio of mass of fuel to mass of air input into engine and it is abbreviated as FA.

Wide-Open Throttle: It refers to the condition when the engine operates with throttle valve fully open when maximum power is desired. It is abbreviated as WOT.

Direct Injection: When the fuel is injected into the main combustion chamber of an engine. Engines have either one main combustion chamber (open chamber) or a divided combustion chamber made up of a main chamber and a smaller connected secondary chamber. It is abbreviated as DI.

Indirect Injection: When the fuel is injected into the secondary chamber of an engine with a divided combustion chamber. It is abbreviated as IDI.

2.2.2 Internal combustion engine - Basic engine cycles

A brief description of the cycle of a four stroke engine is given here with an explanation of each stroke.

Intake Stroke or Induction: In this stroke the piston travels from TDC to BDC with the intake valve open and exhaust valve closed, figure 2.2-a. This movement

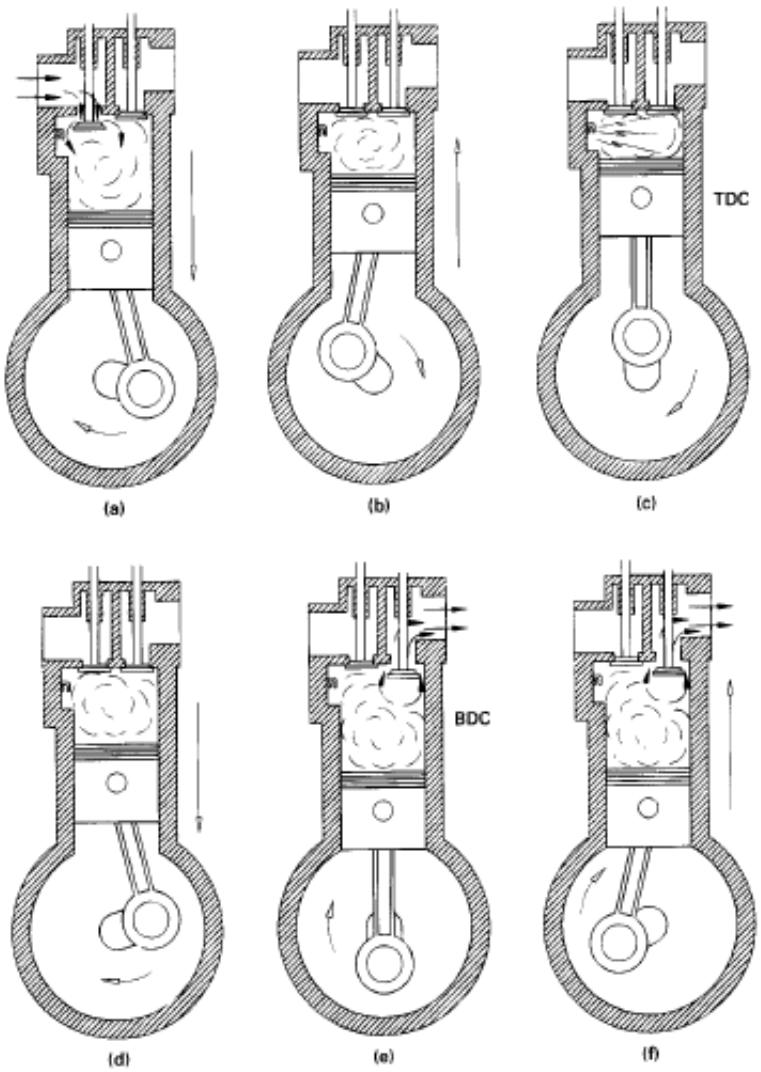

Figure 2.2: Four-stroke SI engine operating cycle. (a) Intake stroke. (b) Compression stroke. (c) Combustion at almost constant volume. (d) Power stroke. (e) Exhaust blowdown. (f) Exhaust stroke. Figure taken from [2].

of the piston increases the volume in the combustion chamber, which creates a partial vacuum. The resulting pressure differential, through the intake system from atmospheric pressure on the outside to the vacuum on the inside, causes air to be drawn into the cylinder. As the air passes through the intake system, fuel is added to it in the desired amount by means of fuel injectors or a carburetor.

Compression Stroke: Once the piston reaches BDC, the intake valve closes and the piston travels back to TDC with all valves closed, figure 2.2-b. The air-fuel mixture will be compressed and both the pressure and temperature in the cylinder will be raised. The finite time required to close the intake valve means that actual compression does not start until sometime after BDC. Near the end of the compression stroke, the spark plug is fired and combustion is initiated. The combustion of the air-fuel mixture occurs in a very short but finite length of time with the piston near TDC (i.e., nearly constant-volume combustion), figure 2.2-c. It starts near the end of the compression stroke slightly before TDC and continues into the power stroke slightly after TDC.

Expansion Stroke or Power Stroke: With both valves closed, the high pressure created by the combustion process pushes the piston away from TDC figure 2.2-d. This is the stroke which produces the work output of the engine cycle. When the piston starts to travel from TDC to BDC, cylinder volume is increased, causing pressure and temperature to drop. Late in the power stroke, the exhaust valve is opened and exhaust blowdown occurs, figure 2.2-e.

Exhaust Stroke: At the time the piston reaches BDC, exhaust blowdown is complete, but the cylinder is still full of exhaust gases at approximately atmospheric pressure. With the exhaust valve remaining open, the piston now moves from BDC to TDC in the exhaust stroke, figure 2.2-f. This movement of the piston pushes most of the remaining exhaust gases out of the cylinder into the exhaust system at about atmospheric pressure.

2.3 Internal combustion engine heat transfer - General concepts

To analyse the heat transfer in internal combustion engines, it is often convenient to divide the engine into six subsystems. Those subsystems include: 1- The intake port, 2- The exhaust port, 3- The combustion chamber, 4- The coolant medium, 5- The lubricating oil and 6- The solid components of the engine [12].

The intake and exhaust ports are important, due to their geometry and the unsteady flow by the inducted air and the fuel in non-direct injection systems, in addition to the exhaust charge. The most important and the most complex subsystem is the combustion chamber, where combustion occurs and the chemical energy in the charge is converted into thermal energy and the pressure and temperature vary very rapidly. The cooling medium is the engine coolant and radiator system for water-cooled engines. The fifth subsystem is lubricating oil which is used to cool the underside of the piston. The last subsystem is the solid components of the engine, which serve the other five subsystems [12]. The subsystem that will be examined in this study is the combustion chamber (the engine cylinder).

The high temperature of the remaining burned gases in the cylinder adds further heat to the combustion chamber components after the combustion process. Consequently, the new incoming charge will be heated, due to the high temperature of those components, and this can cause a pre-ignition in some critical cases. In order to avoid the problems that may occur due to the high temperature, those components are cooled by an external cooling medium. This process adds more complexity to the engine heat transfer phenomenon, because it occurs repeatedly, multiple times in a second. Furthermore, the process of the heat transfer itself is difficult and complex, because it is transient and subject to rapid changes in in-cylinder gas pressure and temperature. The combustion chamber itself, with its moving boundaries, adds further to this complexity. As a result of all these fac-

tors, the heat transfer from the gases to combustion chamber walls is a challenging phenomenon and many of its aspects need to be understood and elucidated.

The heat transfer in internal combustion engines is considered to be an important feature of the engines, because of its effect on the engine performance and emissions. As mentioned above, the cooling process is necessary in the engine. Insufficient cooling can increase the chance of knock occurring. On the other hand, excessive cooling and higher heat transfer to the combustion chamber walls will tend to reduce the availability of the energy in the combustion chamber and decrease the overall output work, by lowering the average combustion gas pressure and temperature [3]. During the combustion process, the thermal cycling causes wear on engine components, and the high temperature and thermal stress can cause failure or serious engine damage. The engine emissions are strongly dependent on the heat transfer and the temperature of the charge, and due to local, national and international legislation, engine emissions are important. Consequently, due to all these facts it can be seen that heat transfer is very important in the design of internal combustion engines.

2.4 Effect of engine variables on heat transfer

The heat transfer from the working fluids to the walls of the combustion chamber depends on many different variables, which makes it difficult to correlate one engine to another. These variables include, engine speed, load, spark timing, equivalence ratio, swirl and squish, inlet air temperature, engine size and wall material. A general comparison of some of those variables is described in the following sections, after references [2] and [3]:

2.4.1 Engine speed

As the engine speed increases, the gas velocity into and out of the engine will increase and this leads to a rise in turbulence and convection heat transfer coefficients. This effect increases the heat transfer occurring during intake and exhaust strokes and even during the early part of the compression stage, Whereas, during the combustion and power stroke, the gas velocities within the cylinder are independent of engine speed as they are controlled by swirl, squish and combustion motion. The convective heat transfer coefficient and thus, the convective heat transfer, are therefore independent of engine speed at this stage. It can be seen in figure 2.3 that as the engine speed increases, all the steady state temperatures go up. Consequently, heat transfer to the engine coolant increases with higher speeds.

When an engine runs at higher speeds, the time per cycle is less. The combustion in the engine occurs over about the same burn angle at all speeds, which means the time of combustion is less at higher speeds, resulting in less time for self-ignition and knock. However, the time for heat transfer per cycle will be less and that means the engine runs hotter, which leads to increased knock problems. Therefore, it can be observed that some engines have an increased knock problem at higher speeds where as some have less problems at higher speeds.

2.4.2 Compression ratio

Increasing the compression ratio in an SI engine up to $r_c = 10.0$ decreases the total heat flux to the coolant. Thereafter, increasing the compression ratio raises the heat flux slightly. The magnitude of the change is modest; for example, raising the compression ratio from 7.1 to 9.4 decreases the heat flux at the valve bridge by about 10 percent. Several of the combustion characteristics change as the compression ratio increases (at fixed throttle setting), such as cylinder gas pressure,

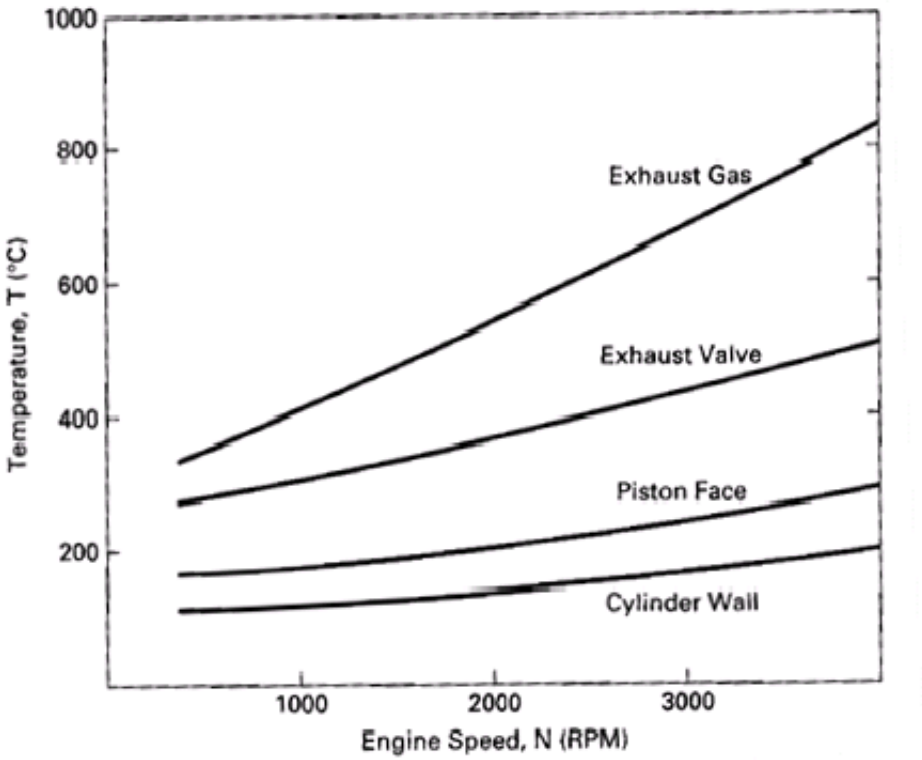

Figure 2.3: Engine temperature as a function of engine speed for typical SI engine. Figure taken from [2].

peak gas temperature and gas motion, which increase as the compression ratio increases, also the gas temperature late in the expansion stroke and during the exhaust stroke, which increases as well, and combustion becomes faster as the compression ratio increases. The component temperatures are affected by the increase of the compression ratio depending on location. In general, the higher the compression ratio, the more expansion cooling will occur during the power stroke, which leads to cooler exhaust, resulting in lowering head and exhaust valve temperatures. The piston and spark plug electrode temperatures generally increase slightly as the compression ratio increases, due to the higher peak combustion temperatures.

2.4.3 Spark timing

As the spark timing is retarded in the SI engine the heat flux is decreased, as shown in figure 2.4. The same trend would be expected in CI engines when the injection timing is retarded. Retarding the spark timing makes the combustion occur later when the cylinder volume is larger, and that decreases the burned gas temperature. Late ignition timing extends the combustion process further into the expansion stroke, which results in higher exhaust temperature and hotter valves and ports.

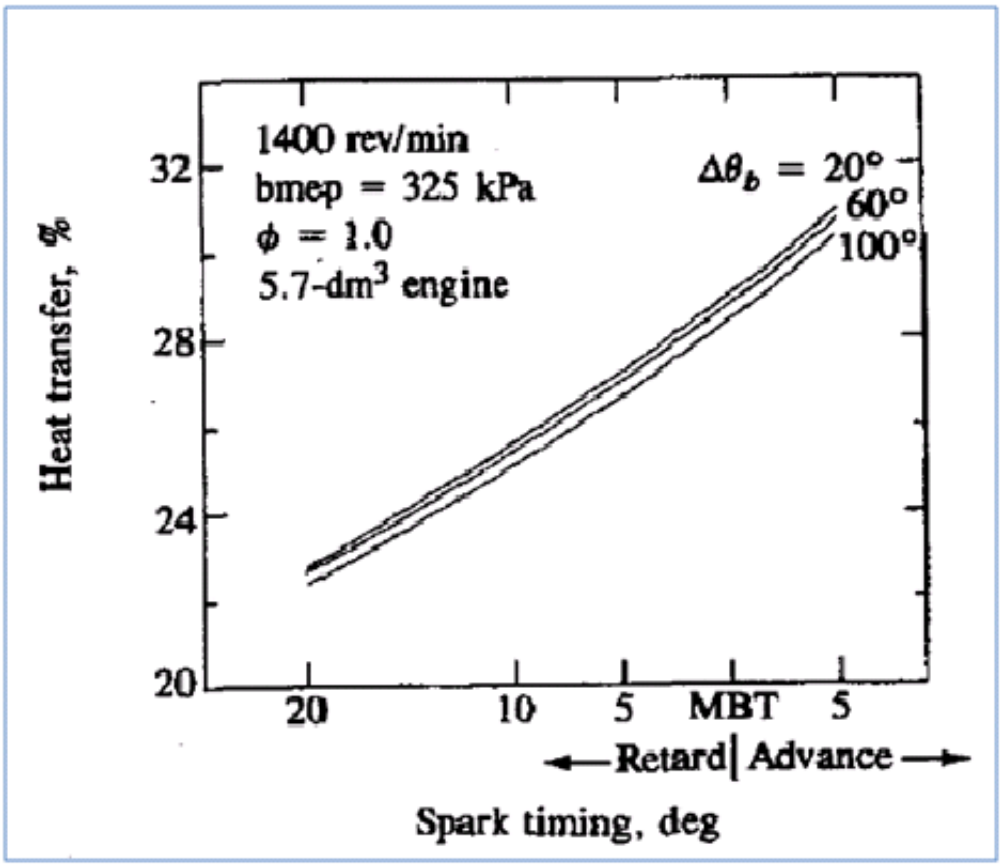

Figure 2.4: Effect of spark timing on heat transfer. Figure taken from [3].

2.4.4 Swirl and squish

Swirl or squish motion increases gas velocity, resulting in a higher heat transfer coefficient, which causes higher heat fluxes.

2.4.5 Equivalence ratio

In spark ignition engines the maximum power is gained at the mixture equivalence ratio $\phi = 1.1$, at which the peak heat flux occurs, and decreases as the engine runs leaner or richer. The maximum heat transfer per cycle as a fraction of fuel chemical's energy will be at stoichiometric condition $\phi = 1.0$, and it then decreases for leaner or richer mixture, as shown in figure 2.5.

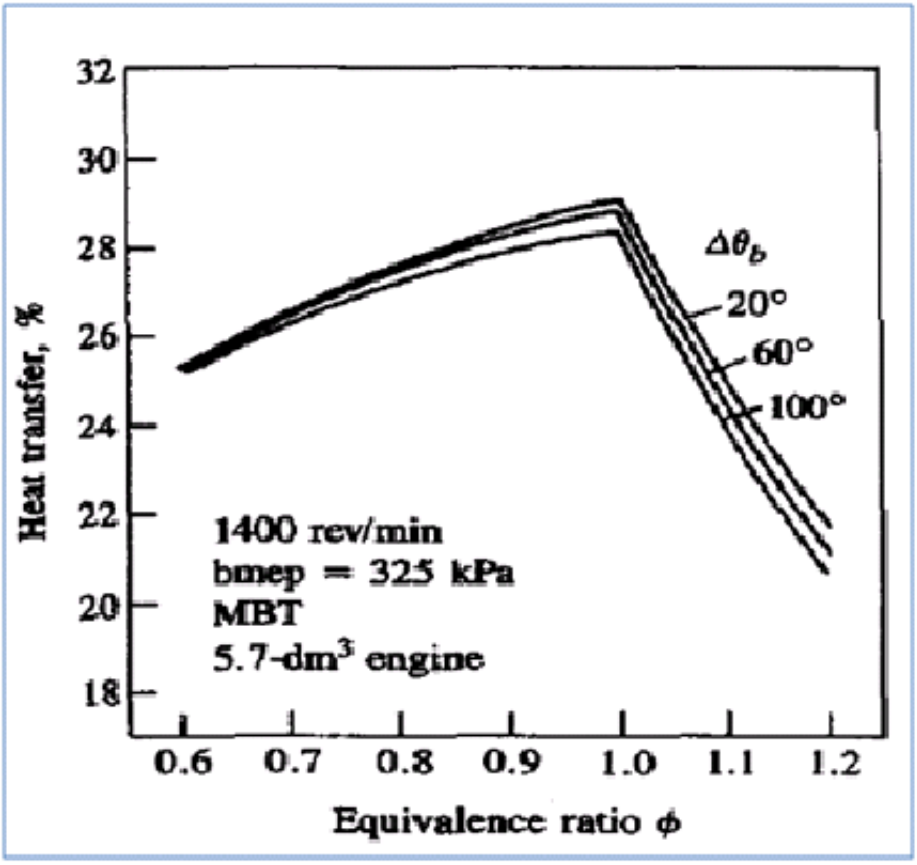

Figure 2.5: Effect of equivalence ratio on heat transfer. Figure taken from [3].

2.4.6 Inlet air temperature

The increase in temperature of the inlet air, increases the heat flux linearly; the gas temperatures throughout the cycle are increased. An increase of about 100 K gives about 10-15 percent increase in heat flux.

2.4.7 Wall material

Different materials are used in manufacturing the cylinder and the piston components of engines, which results in different operating temperatures. The commonly used materials are cast iron and aluminium, which have substantially different thermal conductivities. They both operate with combustion surface temperatures ($200 - 400^{\circ}$ C) which are relatively lower than burned gas temperatures. There is substantial interest in using materials that could operate at much higher temperatures so that the heat loses from the working fluid would be reduced.

2.5 Correlations for heat transfer in internal combustion engines

The heat flux from the working gases to the combustion chamber wall in internal combustion engines can be described using the following equations:

$$N_u = \frac{hl}{k} = CRe^n \tag{2.1}$$

$$q = h(T_g - T_w) \Rightarrow h = q/(T_g - T_w) \tag{2.2}$$

The equation 2.1 represents the typical correlation for the global heat transfer

models, where Nu is the non-dimensional Nusselt number, h is the overall heat transfer coefficient and l and k are the length scale and the thermal conductivity respectively. Re denotes the Reynolds number and C and n are the model constants. The overall heat transfer coefficient can be obtained from this equation, if the model constants and the Reynolds number are known.

Equation 2.2 shows the heat flux q, can be calculated from the overall heat transfer coefficient h, the in-cylinder gases temperature T_g and the wall temperature T_w.

Numerous studies and measurements have been carried out on internal combustion engines to investigate the heat transfer coefficients, and various ways were proposed to obtain these coefficients. The heat transfer coefficient is not non-dimensional, hence it is expressed here in kW/m^2.K unless indicated otherwise. Furthermore, when correlations involve other dimensional parameters, the pressure is expressed in MPa, the temperature in K, the mean piston speed in m/s, the cylinder volume in m^3 and the cylinder bore in m, unless indicated otherwise.

A heat transfer model proposed by Nusselt was the first model for heat transfer and was originally intended to predict the steady state heat flux. This model can also be used to predict the instantaneous heat flux if it is expressed in terms of instantaneous cylinder pressure and gas temperature [12]. Nusselt proposed his model as the sum of convection and radiation heat transfer correlations:

$$h = h_c + h_r \tag{2.3}$$

$$h_c = 5.41 \times 10^{-3}(1 + 1.24C_m)(P_{cyl}^2 T_g)^{1/3} \tag{2.4}$$

$$h_r = \frac{4.21 \times 10^{-4}}{(1/\epsilon_g + 1/\epsilon_w - 1)} \frac{(T_g/100)^4 - (T_w/100)^4}{(T_g - T_w)} \tag{2.5}$$

Nusselt's formula was modified by Brilling who gave the mean piston speed term

$(3.5 + 0.185C_m)$, instead of the original term $(1 + 1.24C_m)$; another modification was made by Van Tyen who gave the mean piston speed term $(3.22 + 0.864C_m)$ [12].

Eichelberg proposed a heat transfer coefficient to describe the instantaneous total heat transfer. He made the first instantaneous heat flux measurement on large two stroke and four stroke diesel engines [12]. Eichelberg's formula can be expressed as:

$$h = 7.67 \times 10^{-3}(C_m)^{1/3}(PT_g)^{1/2} \tag{2.6}$$

Annand [13] reviewed the existing formulae for instantaneous heat transfer rate and proposed his formula for instantaneous heat flux as follows:

$$h = a\frac{k}{B}R_e^{0.7} + b\frac{(T_g^4 - T_w^4)}{(T_g - T_w)} \tag{2.7}$$

where a is a constant ranging from 0.25 to 0.8 and b is a constant suggested to be 4.3×10^{-12} for spark ignition engines and 3.3×10^{-11} for diesel engines. In this formula it can be observed that the second term of Annand's equation represents the radiative heat transfer term.

A formula to calculate the heat transfer coefficient for internal combustion engines was introduced by Woschni [14]. Woschni's formula can be written as follows [12]:

$$h_c = 0.820B^{-0.2}P^{0.8}w^{0.8}T^{-0.53} \tag{2.8}$$

Woschni stated that the characteristic speed w (average gas velocity) depends on two terms. One is due to piston motion and is modelled as the mean piston speed C_m. The other term is due to swirl initiation from the combustion event, which

is modelled as a function of the pressure rise due to combustion. The average gas velocity is assumed to be:

$$w = C_1 C_m + C_2 \frac{V_d T_1}{P_1 V_1}(P - P_m) \tag{2.9}$$

where T_1, P_1 and V_1 are the temperature, pressure and volume at initial condition respectively and P_m is the motored pressure. $C_1 = 2.28$, $C_2 = 0.0$ during the compression stroke. $C_1 = 2.28$, $C_2 = 3.24 \times 10^{-3}$ during the combustion and expansion strokes.

This formula is applicable for only one type of engines and to be valid for different types of engines, different constants must be determined to be applied in this formula.

Woschni's formula was modified by Hohenberg to give better prediction of time averaged heat flux based on experimental observations. The modifications of this formula included the use of instantaneous cylinder volume instead of cylinder bore, and changes of the characteristic speed w (average gas velocity) term to be $(C_m + 1.4)$, and the temperature term exponent to be (-0.4) instead of (-0.53) [15] [16]. Hohenberg's formula can be presented as follows, where the heat transfer coefficient is expressed in W/m^2.K and the pressure is expressed in bar.

$$h = C_1 V^{-0.06} P^{0.8} T_g^{-0.4} (C_m + C_2)^{0.8} \tag{2.10}$$

where C_1 and C_2 are constants and their mean values are $C_1 = 130$ and $C_2 = 1.4$.

Sitkei and Ramanaiah [17] proposed a formula for the instantaneous heat transfer coefficient. This formula was presented in separate convection and radiation terms, in order to recognise the importance of radiation in diesel engines. The equivalent diameter d_e was used instead of the cylinder bore as the characteristic length. The convective heat transfer coefficient was given by the following for-

mula [15], where the heat transfer coefficient is expressed in kW/m^2.K and the pressure in bar.

$$h_c = 0.046(1+b)\frac{P^{0.7}C_m^{0.7}}{T_g^{0.2}d_e^{0.3}} \tag{2.11}$$

The diameter d_e was defined as follows:

$d_e = 4\frac{V}{A}$

The constant b was found to be as follows:

$b = 0.0 - 0.03$ for a direct combustion chamber.

$b = 0.05 - 0.1$ for a piston chamber.

$b = 0.15 - 0.25$ for a swirl chamber.

$b = 0.25 - 0.35$ for a pre-combustion chamber.

Han et al. [18] determined a new empirical formula for instantaneous heat transfer coefficient. The purpose in developing this formula was to analyse the instantaneous value of heat transfer from gas to wall in the combustion chamber of spark ignition engines, where h is expressed in kW/m^2.K and the pressure in bar.

$$h = 687P^{0.75}w^{0.75}D^{-0.25}T^{-0.465} \tag{2.12}$$

$$w(\theta) = 0.494C_m + 0.73 \times 10^{-6}(1.35P\frac{dV}{d\theta} + V\frac{dP}{d\theta}) \tag{2.13}$$

where D is the specific length which was considered as the cylinder diameter. (Note that in the original paper by [18], there is a typographical error in the presentation of equation 2.13).

The heat transfer per cycle to the combustion chamber surface of spark ignition engines for quasi-steady and transient conditions was investigated by Shayler and co-workers [19] . They obtained a correlation between heat transferred, peak

cylinder pressure, engine speed and the cylinder bore. The heat transfer per cycle has been identified in the form:

$$q\ (kJ/cycle) = 9.0 \times 10^{-5} \frac{P(bar)B^{4.5}(cm)}{N^{0.8}(rpm)} + 0.04 \tag{2.14}$$

A new model was proposed by Wu et al. [6] for heat transfer for small-scale spark-ignition engines. The Stanton number was used in this model and they considered the heat transfer surface area to be two times the piston area. The proposed model is:

$$h = St\rho C_p u \tag{2.15}$$

where h is expressed in W/m^2.K and u is the gas turbulent fluctuating velocity which can be approximated as $0.5C_m$. The Stanton number can be expressed as:

$$St = 0.718 \times e^{(-0.145C_m)} \tag{2.16}$$

Sharief et al. [20] proposed a heat transfer correlation based on experiments on a motored diesel engine. In the Reynolds number in this correlation the intake jet velocity was applied instead of mean piston velocity. Their correlation for estimating the heat transfer from engines is:

$$h = 20P^{0.6}V_j^{0.6}T_g^{-0.222}d^{0.4} \tag{2.17}$$

where h is expressed in W/m^2.K and the pressure in bar.

Rao and Bardon [21] presented a formula for the instantaneous heat transfer coefficient in a reciprocating engine. This formula was developed based on the

turbulent diffusion and it relates the convective heat transfer coefficient to the turbulent intensity in the charge. This formula can expressed in the form:

$$h = \rho C_p U_T = 0.058 \rho C_p \acute{u} \tag{2.18}$$

2.6 Studies on heat transfer in internal combustion engines

Much research has been performed regarding the measurement, investigation and estimation of heat transfer from the working fluid to the wall in internal combustion engines. From the literature it can be found that different approaches and methods have been applied to obtain measurements. Different engines were tested, considering different parameters such as air to fuel ratio, engine speed and engine load.

2.6.1 Experimental studies

Experimental studies with correlations evaluation and development

Woschni [14] introduced a formula to calculate the heat transfer coefficient for internal combustion engines, equation 2.8. He established his formula based on convection heat transfer similarity laws. The Nusselt experiments were repeated in this study, and other formulas, based on the Nusselt's formula, were represented and compared with the author's formula. According to this study, the heat transfer in the internal combustion engine was controlled by forced convection due to the piston motion and the combustion. Thus the heat transfer was considered only by free convection after the combustion process was complete. The study showed that in the combustion phase, the heat transfer coefficient increases, mainly be-

cause of the additional convection caused by combustion. Furthermore, it also demonstrated that, for a local mean heat transfer coefficient, the local mean gas velocity must be applied in the definition of the Reynolds number. This formula is applicable for only one category of engines and to be valid for different types of engines, different constants must be determined to be applied in this formula.

Oguri [22] investigated the heat transfer rate from the working gases to the combustion chamber walls of a four stroke spark-ignition engine. From this study it was concluded that the estimated heat transfer coefficients experimentally coincide well with those calculated by Eichelberg's formula (equation 2.6), in the combustion period and the first half of the expansion stroke. It was also found that the experimental values of heat flow in the compression stroke coincide with the values calculated using the heat transfer coefficient using Eichelberg's formula, and there are no extreme differences between them, as was found when the heat transfer coefficients were compared. This study also observed that, in the latter half of the expansion stroke, the values of the heat transfer coefficient and the heat flow estimated experimentally are smaller than those calculated by Eichelberg's formula. From this study a new dimensionless formula was obtained and was satisfactory when applied in the expansion stroke, but it is difficult to apply this formula to large engines.

Hassan [23] described a new approach for the unsteady heat transfer prediction in internal combustion engine cylinders, using the existing empirical heat transfer data of forced convection for the flat plates or pipes. Experimental data were obtained and compared with the data from the existing empirical correlations. Results showed that there was an agreement between experimental data and existing data on heat transfer from a flat plate in turbulent flow. The results also showed that the use of the existing flat plate and pipe flow data to predict the convection heat transfer in internal combustion engine cylinders could be supported.

Shayler and others [19] investigated the heat transfer per cycle to the combustion chamber surface of spark ignition engines, for quasi-steady and transient

conditions. The Woschni correlation for heat transfer was applied. A correlation between heat transferred, peak cylinder pressure, engine speed and the cylinder bore was obtained. It was observed that the cyclic variations in heat transfer dependent on variations in peak pressure. This study included the heat flux distribution over the surface of the chamber and it showed that the heat flux is dependent on location along the liner.

Wu et al. [6] proposed a new model for heat transfer for small-scale spark-ignition engines. According to this study, the previous heat transfer models were not suitable for small engines, because they were originally developed for large-scale engines. The Stanton number was used in this model. In this study the heat transfer surface area was considered to be twice the piston area. The results showed that the proposed model has better predictive capability than previous models.

Sharief and others [20] proposed a heat transfer correlation based on experiments on a motored diesel engine. In the Reynold's number in this correlation, the intake jet velocity was applied instead of mean piston velocity. According to this study, the intake jet velocity takes into account the inlet port and piston diameters. Thus it represents the gas velocity better than the mean piston speed. Comparing this correlation with earlier correlations at different loads, showed an agreement between this correlation and Eichelberg's correlation (equation 2.6) at the combustion and expansion periods. It was observed that the heat transfer rate increased with an increase in the load and engine speed.

Enomoto and Furuhama [24] determined the local heat transfer coefficients at different locations on the wall surface of a combustion chamber of a four-stroke gasoline engine. They concluded that the heat transfer coefficient starts to rise simultaneously with rise of the pressure in the combustion chamber, due to the ignition at most measuring points on the piston surface and the piston head. Those values of the heat transfer coefficient were several times greater than those calculated by Eichelberg's formula. At some points on the piston surface, the cylinder

head and all measuring points on the cylinder surface, the peak values of the heat transfer coefficient and the phase were similar to those calculated by Eichelberg's formula. The heat transfer coefficient was affected by the geometry of a cylinder head. The study also showed that, at higher engine speed, the heat transfer coefficient values calculated by Eichelberg or Woschni formulas substantially differ from the measured values.

Sanli et al. [25] examined numerically the effects of spark timing and the engine load on the in-cylinder heat transfer of a spark ignition engine, using experimental engine test data. A four-stroke, air-cooled, single-cylinder SI engine was tested. The Woschni, Hohenberg and Han models were employed to perform the investigation on this engine at 2000 rpm engine speed and different spark timings and engine loads. It was concluded that the in-cylinder heat transfer coefficient and the heat flux at constant load and speed conditions increased slightly when the spark timing is advanced, and their peak values occur at earlier crank angle than that of the original spark timing. It was also demonstrated that the in-cylinder heat transfer coefficient and the heat flux were slightly decreased when the spark timing retarded from the original timing. On the other hand, the effect of changing the engine load at constant spark timing was investigated as well, and it was found that the magnitude of the in-cylinder heat transfer coefficient and the heat flux were increased when the engine load was increased. In comparison between the three heat transfer models used in this study, it was observed that the Han model gave higher heat transfer coefficient and heat flux than the other two models. Furthermore, the values of the heat transfer coefficient and the heat flux were higher for each model relative to the original spark timing from the beginning of spark timing toward the peak point at the advanced spark timing, whereas their values were lower at the retarded spark timing. Towards the end of the compression stroke, each model gave higher values for the heat transfer coefficient and heat flux at the retarded spark timing, in contrast to the original timing while those values were lower at the advanced spark timing.

Wang et al. [26] investigated the effect of the ignition timing, air-fuel ratio and the mixture preparation on the engine heat flux. The investigation was conducted on a spray-guided, direct-injection, spark-ignition, single-cylinder research engine. A thermodynamic simulation code was implemented to predict the heat transfer from the gases to the combustion chamber walls, using different heat transfer correlations. It was concluded that the peak heat flux value became higher by advancing the ignition timing. Furthermore, advancing the ignition timing increased the peak cylinder pressure and temperature, which increased the magnitude of the peak heat flux. When analysing the effect of the air-fuel ratio, it was found that when the mixture was stoichiometric or richer than stoichiometric, the magnitude of the heat flux was higher and showed an earlier phasing. Two modes were used to investigate the effect of the mixture preparation, DI (Direct Injection) and PI (Plenum Injection). In the DI mode the data were presented for two cases with injection in the intake stroke and one case in the compression stroke. In the latter, the peak heat flux was higher than the mean value for the other tested conditions. Comparison of the two modes at different air-fuel ratios revealed that the heat flux increased as the mixture became richer in the two injection modes. But the increase was larger in the PI mode than in the DI mode. The heat transfer correlations of Eichelberg, Woschni and Hohenberg were used to predict the heat transfer from the gases to the walls of the combustion chamber. The results obtained from the experimental measurements were compared with the data obtained from these models. It was found that Hohenberg's correlation seemed to be the most accurate model, as Woschni's model underestimated and over-estimated the heat flux before and after the top dead centre respectively. Some modifications were made to Woschni's model to make it more accurate in the low-load low-speed testing operating conditions on the engine used in this study.

Experimental studies with the examination of measuring location and operating condition

Uchimi and coworkers [27] studied the conditions of heat loss to combustion chamber walls in a direct injection diesel engine. To characterise the heat loss to the entire piston surface of this engine, measurements of instantaneous heat flux were conducted at different points. Those points were the piston crown, and the side and bottom of the cavity. Results showed that there were differences in the piston surface instantaneous temperature waveform, the instantaneous heat flux waveform amplitude and the peak phase between different measuring points. The results also showed that the heat loss to the piston surface relative to the calorific value of fuel was higher than those of the gasoline engine measured in earlier studies.

Hoag [28] measured the instantaneous temperature at three positions on the cylinder head of a direct injection diesel engine. The study found that the instantaneous heat flux was sharply concentrated near the top dead centre during combustion and dropped off rapidly during the expansion processes. The study showed that the heat flux reached its minimum values late in the expansion process and then increased throughout the exhaust process. This study also showed that the increase in the wall temperature led to an increase in heat transfer to the charge during the intake process and reduction in heat rejection during the compression process. During combustion and early in the expansion process there were no detectable differences in the instantaneous heat flux with increase in wall temperature.

Alkidas [29] measured the transient heat flux at four positions on the cylinder head of a four-stroke single-cylinder spark ignition engine. This engine was tested under fired and motored conditions. The variations of engine speed and spark timing was investigated in this study. This study concluded that at fired conditions, the initiation of the rapid increase of heat flux at each position of measurement

is correlated reasonably with the time of flame arrival. However, at the motored conditions, the increase of heat flux during the compression stroke occurs simultaneously at the four positions of measurement. The study also showed that varying the position of measurement on the cylinder head considerably varies the peak heat flux. Moreover, it also showed that advancing the spark timing and increasing the engine speed increased the peak heat flux at each position of measurement.

In another study Alkidas and Myers [30] measured the heat flux at several positions on the cylinder head and liner of a four-stroke, single cylinder, and spark ignition engine. The influence of air-fuel ratio and volumetric efficiency on heat transfer was investigated. This study illustrated that the variations of the air-fuel ratio did not strongly affect the local transient heat transfer at constant engine speed and volumetric efficiency. Furthermore, at near-stoichiometric mixture combustion the peak heat flux reached a maximum, while it decreased at leaner and richer mixture combustion. The peak heat flux increased about 30 %, due to the increase in volumetric efficiency from 40 to 60 percent. The amount of heat transferred to the walls of the combustion chamber during the closed portion of the cycle, which was calculated using the integrated form of the first law of thermodynamics, matched well with the corresponding transient heat flux measurements values. Cycle-to-cycle variations in the surface temperature and the heat flux were noted at each location of measurements, due to the variation of the propagation of the flame through the combustion chamber.

Harigaya et al. [31] estimated the instantaneous local heat transfer coefficient on the combustion chamber wall. A four stroke, L-type, single cylinder spark-ignition engine was used in this experimental study. This study investigated the effects of gas flow and flame propagation on the heat transfer coefficient. Local heat flux at twenty four locations was measured on the cylinder head. It was concluded that the gas velocity in the combustion chamber increased with decreasing the throat area, and particulary the velocity near the throat was higher than that in

the other parts of the chamber. Furthermore, the gas flow and flame propagation have a strong influence on the local instantaneous heat flux. The heat transfer coefficient varies with measuring positions and it increases with increasing the flame velocity. The study also observed that there is a strong correlation between the Nusselt number based on the local heat transfer coefficient and the Reynolds number based on flame velocity.

Gilaber and Pinchon [32] examined the effects of some parameters on the heat transfer in spark ignition engines. The effects of varying the spark timing, the volumetric efficiency, the engine speed, the equivalence ratio and the swirl number were tested on a single cylinder spark ignition engine. A laser doppler velocimeter (L.D.V) was used to analyse the effect of fluid dynamics on heat transfer and four heat flux gauges were installed in the combustion chamber. The spark timing was changed from 0 to 40 degrees BTDC. Examination of the effect of changing the spark timings showed that the maximum peak value of the measured heat flux was found to be at spark advance of 40 degrees BTDC. Moreover, it was observed that the peak heat flux values decreased from 2500 kW/m^2 to 1200 kW/m^2 when the spark advance decreased from 40 to 0 degrees at location 1, and the same trend was observed at the other three locations. However, no significant changes were obtained on the turbulence levels in the L.D.V measurement volume when the spark timings were changed. When analysing the effect of the volumetric efficiency, three values were chosen, these being 0.9, 0.8 and 0.5. It was concluded that, when the volumetric efficiency increased from 0.5 to 0.9 the peak values of the heat flux increased from 1500 kW/m^2 to 2800 kW/m^2 at location 1. It was also observed that the turbulence levels did not depend on the volumetric efficiency. In the analysis of the engine speed, three different speeds were tested, 500 rpm, 1500 rpm and 2500 rpm. This analysis showed that the peak heat flux values increased from 2000 kW/m^2 to 3100 kW/m^2 as the engine speed increased from 500 rpm to 2500 rpm. Furthermore, it was found that, the heat transfer duration declined from 17 milliseconds at 500 rpm to 7 milliseconds at 2500 rpm. To examine the influence of the equivalence ratio, five equivalence

ratios ranging from 0.7 to 1.1 were chosen. The maximum value of the heat flux increased from 800 kW/m^2 to 2200 kW/m^2 at the equivalence ratios 0.7 and 0.9 respectively, and then reached a limit of 2400 kW/m^2 when the equivalence ratios of 1.0 and 1.1 were reached. The swirl conditions were also analysed and for this analysis three swirl conditions were studied, a high swirl, a medium swirl and a low swirl. The effect of the swirl could be clearly observed at locations 3 and 4, where the peak heat flux increased from 2000 kW/m^2 to 3000 kW/m^2 when the swirl condition changed from low to high swirl. However, no significant changes could be found on the turbulence levels as the swirl conditions were changed. It was also concluded from this study that the turbulence intensity was found to be the main parameter which affected the heat transfer when the engine speed was varied.

Prasad and Samaria [33] investigated the effect of the insulation coating applied on the cylinder wall, on the temperature and the heat loss of a semi-adiabatic diesel engine. The cylinder wall was coated externally with a 2 mm thin layer of oxide based ceramic insulation material. The investigations concluded that as the thickness of the insulation coating was increased, the overall body temperature of the piston increased. It was also found that with a 2 mm-thick insulation coating, the reduction in heat loss through the piston was found to be about 6 percent. The study also concluded that the heat loss through the air in the crank-case increased, while the heat loss through the cooling water decreased. It was also demonstrated that the effect of cooling medium temperature was dominant at low loads, whereas at high loads the effect of the hot gas temperature was obvious.

Enomoto et al. [34] investigated the heat losses during knocking in a four-stroke gasoline engine. The effect of advancing the ignition timing and varying the gasoline octane number were examined. Two thin-film thermocouples were embedded in the piston crown. In the normal combustion without knocking it was concluded that the temperature started to rise later as the distance of flame propagation

from the spark plug became greater. In the case of combustion with knocking, in the zone where the temperature of the wall surface began to rise due to the arrival of the normal combustion flame, the temperature was raised further by knocking. Furthermore, by advancing the ignition timing and lowering the gasoline octane number, the temperature fluctuation became greater. During the knocking the heat loss was greater during the working stroke in proportion to the knock intensity. It was also found, when the knock intensity exceeded a certain value, the heat loss during the working stroke became greater than the total heat loss during a cycle. On the other hand, when the ignition timing advanced, the heat loss during the compression stroke increased, but the heat loss during the working stroke was greater. The increase in heat loss during the working stroke caused by knocking, was higher when the octane number was made smaller, than the case when the ignition timing was advanced. It was also observed that the measured values of the heat transfer coefficient increased in proportion to the knock intensity, whereas the values calculated by Woschni's and Eichelberg's equations were hardly changed by the knock intensity.

Kimura et al. [35] investigated the effect of combustion chamber specifications, swirl ratios and injection timing on the transient heat transfer characteristics. A single-cylinder, direct injection diesel engine was used in this investigation. Four thin film thermocouples on the piston were used to measure the instantaneous temperature, in order to determine the transient heat flux rates. The heat flux was investigated at two locations, the piston cavity and the piston head. In examining the effect of the cavity diameter on the heat flux, it was found that at 7° CA BTDC injection timing the heat flux peak decreased with a larger cavity diameter, and the heat flux started to increase after 30° CA ATDC. At the piston crown however, the heat flux was not affected by the cavity diameter. For 2° CA ATDC injection timing, the heat flux did not change at either location. In investigating the effect of the swirl ratio on the heat flux at the two locations, it was found for the 7° CA BTDC injection timing in the piston cavity, that the heat flux peak increased with a higher swirl ratio, however the heat flux started to reduce at 10°

CA ATDC. In the piston head the heat flux peak was found not to be affected by the swirl ratio. For the 2° CA ATDC injection timing, the heat flux peak increased at both locations with a higher swirl ratio. From this study it can be concluded that the heat flux at the piston crown is not influenced by the cavity diameter and the swirl ratio and it only relates to the injection timing.

Harigaya et al. [36] conducted an experimental study to measure the local surface temperature and heat flux on the combustion chamber wall of a four-stroke, single-cylinder spark ignition engine under knocking and non-knocking conditions, using thin film thermocouples. From this study it was found that under normal conditions, the maximum heat fluxes decrease and the time for the maximum heat flux occurs later, as the distance from the spark plug increases. It was also clear that the positions near the ignition point experience higher heat fluxes. On the other hand, under knocking conditions at positions away from the knock zone, the maximum heat fluxes were almost the same as those under normal conditions. In the knock zone however, the maximum heat fluxes were higher. Moreover, it was also found that the heat fluxes were higher than those under normal conditions during the expansion stroke. It was also demonstrated that the maximum heat fluxes in each position were approximately constant for knock intensities less than 0.3 MPa. It was observed that the maximum value of heat flux was about 2.0 times and the time-averaged value 1.24 times larger than those under the non-knocking conditions. Furthermore, it was also concluded that the heat transfer coefficient was not affected by the knock intensities under 0.3 MPa, and it was found at the knock zone for the knock intensity 0.6 MPa, that the heat transfer coefficient was about 2.6 times larger than was found under normal conditions.

Wang et al. [37] studied the burn rate and the instantaneous in-cylinder heat transfer in a spray-guided, direct-injection, spark-ignition engine. Three different fuels, gasoline, iso-octane and toluene were used in this study. Four thermocouple probes were installed in the combustion chamber walls to measure the surface temperature. This study investigated the effects of the ignition timing, air-fuel

ratio, fuel injection timing and the injection strategy on the burn rate and the in-cylinder heat transfer. Investigating the effect of varying the ignition timings on the peak heat flux and its phasing showed that, as the ignition was advanced the peak heat flux increased and its phasing was advanced. It was also found that the cyclic heat transfer was slightly increased as the ignition timing was advanced from 35° to 45° CA BTDC. In studying the effect of the air fuel ratio, it was concluded that the peak heat flux and the cyclic heat transfer were reduced as the mixture became weakened and the phasing of the peak heat transfer was advanced when the mixture was lean. When the effect of the injection strategy was investigated, two different ways of injection were examined, the direct injection DI and the port injection PI. The peak heat flux and the cyclic heat transfer were higher in the PI mode than in the DI mode for toluene and gasoline, but this difference became smaller when the mixture became lean. The influence of the injection timing was examined as well, and it was observed that, for the late direct injection during the compression stroke, the peak heat flux was comparable to those with early injection. In overall comparison between the three fuels, it was found that the gasoline showed the lowest peak heat flux and cyclic heat transfer among the three fuels. A modified Woschni correlation was used to model the in-cylinder heat transfer, and constant scaled factor was used for all cases. The prediction showed a good agreement with the experimentally obtained results.

Desantes et al. [38] investigated the effect of the intake conditions on the local instantaneous heat flux in a direct injection diesel engine. The effect of the injection pressure, the intake air temperature and the oxygen concentration at the intake were investigated. A fast response thermocouple was installed in the combustion chamber of a single cylinder, direct injection diesel engine, to measure the instantaneous wall temperature. In examining the effect of the injection pressure on the instantaneous heat flux, it was found that the heat flux peak increased as the injection pressure increased. It was also found that the heat flux peaks occurred earlier than the in-cylinder pressure peaks, and it was observed that the higher the injection pressure, the closer the peak to the top dead centre (TDC). In

order to evaluate the influence of the intake air temperature, it was concluded that warming the intake air temperature to about 70 °C increased the fire wall temperature uniformly by about 20°C. It was also observed that increasing the intake air temperature to 120 °C led to a higher heat flux. Examining the effect of the oxygen concentration at the intake showed that the local heat flux was sensitive to the composition of the charge.

Experimental studies accounting for engine load and/or speed

Enomoto et al. [39] obtained the surface temperature variation and instantaneous heat flux of the piston and the cylinder of a four-stroke gasoline engine for each stroke and identified the heat loss ratio which appears to be the amount of heat loss to a particular component relative to the fuel energy. Results showed that the heat transfer ratio for the piston was 2-3 % and 3-6 % at full and partial load respectively. The heat transfer ratio for the cylinder liner was 2-3 % at both full and partial load. Under knocking conditions the heat flow into the piston increased by 70 % in the working stroke compared with the amount under normal combustion. The overall heat transfer ratio for the piston and cylinder was about 4-6 % at full load, 8 % under knocking and 5-9 % at partial load.

In addition to the previous study, Enomoto et al. [40] determined the surface temperature variation and instantaneous heat flux of the cylinder head and the suction and exhaust valves of a four-stroke gasoline engine. The results illustrated that the heat transfer ratio for the cylinder head was 2.5-3.5 % at full load and 3-6.3 % at partial load. The heat transfer ratio for the intake and exhaust valves was 0.5-0.8 % and 0.6-1.2 % at full and partial load respectively. Under the knocking conditions the ratio of heat transfer increased during the working stroke. The overall heat transfer ratio in a cycle was 4.5 % for the cylinder head, 1.0 % for suction and exhaust valves and 13.5 % for the entire combustion chamber surfaces.

Sanli et al. [41] investigated the heat transfer characteristics between gases and in-

cylinder walls at fired and motored conditions in a diesel engine. A four-cylinder, indirect injection diesel engine was tested. The Woschni correlation was used, to calculate the heat transfer coefficient by using the experimental data that they obtained. Results showed that the increase of engine speed at low constant load slightly decreased the in-cylinder peak heat fluxes and heat transfer coefficients, while increasing the engine speed at higher loads caused an increase in the in-cylinder heat transfer coefficients. However, the peak heat fluxes remain approximately the same for the higher loads case. Increasing the engine load at constant speed increased the peak heat fluxes and the heat transfer coefficients. Under motored conditions, increasing the engine speed increased the peak heat fluxes and the heat transfer coefficients.

Wang and Stone [37] studied the instantaneous heat transfer during the warm-up stage on a Rover K16 four-cylinder spark-ignition engine. In this study they investigated the effects of engine loads and engine speeds on the instantaneous heat transfer. The Woschni and Hohenberg correlations were applied in a simplified single-zone model to model the engine heat transfer. It was found that both correlations gave very similar results under both steady state motoring and firing conditions. Consequently, only the Hohenberg correlation was further used for modelling the heat transfer during the warm-up stage. They found that the measured peak heat flux increased when the wall temperature increased, and the measured heat flux phasing became earlier. This was a result of the increasing burn rate and higher burned gas temperature with rising wall temperature. They also found that the rate of change in the peak heat flux is greater and its phasing is earlier at higher loads and higher engine speeds. It was also concluded that both the modelled and the experimentally calculated heat transfer coefficients were found to increase with increasing wall temperature, which led to an increase in the heat flux as the wall temperature rose.

2.6.2 Analytical and computational studies

Han et al. [18] developed a new empirical formula for the analysis of instantaneous heat transfer coefficient and the instantaneous value of heat transfer from gas to wall in the combustion chamber of a spark ignition engine. Predicting the heat transfer coefficient on the wall of a combustion chamber by using the existing empirical formula, showed that the time averaged values matched the experimental data, whereas the instantaneous values during the cycle showed big differences between the empirical results and the experimental data. However, the results from the new empirical formula revealed a good match with experimental data.

Rao and Bardon [21] developed a formula for computing the instantaneous convection heat transfer coefficient between the charge and the confining walls in a reciprocating engine, equation 2.18. The formula was developed from basic considerations of turbulent diffusion and also it relates the convection heat transfer coefficient with the turbulence intensity in the charge. This formula is expected to be more accurate and applicable to all engine types, and relative to the previous heat transfer correlations, it involves less empiricism. According to this study, the numerical factors which were used in developing the formula were suggested based on the best information available at that time. The study illustrated that the value of the final constant can be conveniently adjusted as better measurements of turbulence intensities in the charge become available.

Depcik and Assanis [42] presented a universal quasi-steady heat transfer correlation for the intake and exhaust flow of an internal combustion engine. This correlation was developed from the micro scales of turbulence and it allows only for one engine-dependent parameter. According to this study, a single correlation was presented to describe the intake and exhaust side heat transfer data.

Lawton [43] measured the instantaneous heat flux at the surface of a cylinder head in a motored diesel engine at different speeds. This study found that the observed heat flux was different from the predicted one according to existing quasi-steady

theories. However, when the gas temperature external to the boundary layer and the wall temperature were equal, in particular it was found that there was a significant heat flux. The maximum heat flux was found to occur at about 8° before top dead centre. Furthermore, it also concluded that the heat flux during compression was larger than that during expansion. The solution of the equation of thermal energy gave a very good prediction of the observed heat flux at all engine speeds. After a simple modification, Annand's equation gave good results and it was recommended for general cycle calculations.

Mohammadi et al. [44] used a CFD code to compute the average heat flux and heat transfer coefficient on the cylinder head, liner, piston and intake and exhaust valves of a spark ignition engine. In this study the Woschni correlation was used to compare with the computationally determined total heat transfer on the combustion chamber. From this comparison, close agreement was observed. Results showed that maximum heat flux in each part occurred at maximum cylinder pressure. It also showed that the higher heat flux was on the intake valves, and the heat flux on the cylinder head was more than on the piston. In this study new correlations to estimate the maximum and minimum variation in convective heat transfer coefficients in spark ignition engines were proposed.

Nijeweme et al. [11] investigated the unsteady heat transfer in a spark ignition engine. Their measurements of the instantaneous heat flux showed that there is a heat transfer from the wall into the combustion chamber, even when the bulk gas temperature was higher than the wall temperature. They explained their result by modelling the unsteady flow and heat conduction within the gas side thermal boundary layer. They reported that it is impossible for the widely used correlations (of the form $Nu = Re^a Pr^b$) to give the correct phasing when the bulk gas temperature is being used. Therefore, in their CFD heat flux calculations, the work term within the boundary layer and the convection term need to be included, if accurate results are to be obtained. Twelve fast response thermocouples were installed through the combustion chamber of the tested engine. The sur-

face heat fluxes were calculated for the motored and fired conditions at different speeds, throttle settings and ignition timings. The combustion system was modelled with computational fluid dynamics to compare the measurements. The CFD prediction gave a very poor agreement with the experimental measurements. The one-dimensional energy conservation equation has been linearised and normalised and solved in the gas side boundary layer for the motored case. The heat conduction, the energy equation with work term in the boundary layer and a convective flow normal to the surface were implemented as well. The results showed that the work term causes a phase shift of the heat flux forward in time, and the convective flow term contributes significantly to the magnitude of the heat flux.

Noori and Rashidi [45] determined the locations where the heat flux and the heat transfer coefficient are the highest. A spark ignition engine with a flat roof combustion chamber was used in this study. The KIVA-3V CFD code was used to simulate the flow, combustion and heat transfer on this engine. Some locations on the cylinder head and the centerline of the piston surface were considered, to estimate the heat flux and the heat transfer coefficient. From this investigation it was concluded that during the compression stroke, the distribution of the heat transfer coefficient was only influenced by the gas velocity distribution. However, during the combustion period, it was affected by both the local gas velocity and the density. Furthermore, it was found at the arrival of the flame at any location, the heat flux increased rapidly at that location and the maximum value occurred at the time of the peak cylinder pressure and temperature. Some locations experienced the highest heat flux when the flame arrived at the time of the peak cylinder pressure. It was also concluded that the heat flux on the cylinder head was found to be higher than that on the piston and the cylinder walls, and that would be due to the fact that most of the combustion and the higher gas velocities take place at the cylinder head. Moreover, it was observed that the average area heat flux and the heat transfer coefficient were found to have the highest values at the cylinder head and the lowest values at the cylinder walls. In comparison between the average area heat flux calculated using the CFD simulation and Woschni's

correlation, it was found that the calculated heat flux using the Woschni's correlation was lower than that calculated using the CFD simulation. Furthermore, in comparing the local heat flux obtained with the CFD simulation and the average area heat flux estimated by Woschni's correlation, it was demonstrated that the heat flux values predicted using the two methods were approximately the same before and after the combustion period.

Section summary Most of the studies mentioned in this section showed that the previous heat transfer models are engine-specific and to apply them to different engines configurations, different parameters are required. Furthermore, it can also be concluded that in the heat transfer model proposed by Woschni, which is widely used, the velocity term with pressure-dependent parameters would cause an over-prediction of heat transfer, except in the cases under low speed and low load operating conditions where the effect of pressure increase on heat transfer is quite low. Moreover, it is concluded that in the small scale engines, the existing heat transfer models might not be able to predict the heat transfer rates as originally proposed for large scale engines. It is also observed that the prediction of heat transfer using the existing models, showed some agreement in evaluating the phase of the predicted heat transfer in most of the cases studied, with a reasonable difference in the magnitude. It can be clearly demonstrated that no universal heat transfer model existed and to apply the currently available models the application of scaling factors and tuning parameters are required, as will be presented in this study when different heat transfer models are examined. It is also observed that the heat transfer models by Woschni, Eichelberg and Annand were the models most used among the existing heat transfer models. Although there are some deficiencies in the existing models, they remain the best available and they were used in the current study as a starting point for further analysis.

The effect of different operating parameters and measuring locations on heat transfer were investigated. Most of the studies mentioned earlier obtained the same results from their investigations. In investigating the effect of the ignition

timing, it was observed that advancing the spark timing increases the peak heat flux values. Moreover, in the examination of the influence of the air/fuel ratio on the heat flux it was found that the weaker the mixture, the lower the heat flux. It is also concluded that increasing the volumetric efficiency increases the peak heat flux values. When the effect of engine load and engine speed were tested, it was found that increasing the engine load reduces the heat transfer rates, whereas increasing the engine speed increases the peak heat flux values. The heat flux was examined in different measuring locations and it is believed that the heat flux varies from one location to another, which has also been concluded from the study conducted in this research. The current study also observed that the heat flux values become lower as the distance from the spark increased, a finding which was supported by the conclusion of some of the studies presented earlier.

2.7 Methods of measuring heat flux in internal combustion engines

The heat transfer between gases in the cylinder and the cylinder wall of internal combustion engines needs to be measured and estimated accurately. Two possible ways are available for estimating heat transfer in internal combustion engines. The first one is to use the heat balance. The drawback of using the heat balance method is that only a cycle averaged heat flux can be measured. This method is not suitable for the modern research as instantaneous heat transfer data is really required to progress state-of-the-art modelling. The second method is to use heat flux and temperature sensors which are specifically designed for the measurement of the instantaneous temperature and heat flux [4].

Heat flux sensors

The measurements of the cylinder wall surface temperature are necessary to estimate the instantaneous heat flux. The surface temperature at the combustion chamber walls varies very quickly due to the unsteady boundary conditions. The fast variation in the temperatures at the surface makes it necessary to choose the size of the the temperature sensor (which can be used to measure those temperatures) to be as small as possible and as close to the surface as possible. In the design of a temperature sensor, a wide range of options are open to the engineer. The temperature sensor materials must be selected to be compatible with the requirements for minimal thermal distribution and thermal response times. Further to this point, strong demands on the construction of the surface temperature sensors need to be considered as the thermophysical properties of those sensors have to be close to those of the wall material. Moreover, the temperature sensor 'the gauges' should not interfere with the fluid flow (gases in cylinder) [12] [4]. A discussion and a brief outline of some of the most common sensors follows.

Film type thermocouple gauges

The thermocouple elements are thin layers of different materials which are deposited on each other. The small mass of the thin film thermocouples make their response to the temperature fluctuations very rapidly. It was reported by Demuynck et al. [4] that the surface thermocouple used by Annand [46] was made from three different films (aluminum, magnesium-fluoride and antimony). This thermocouple was attached directly to the cylinder head surface. Dent and Suliaman [47] as mentioned by Borman and Nishiwaki [12] used another example of this type. They used vacuum deposited films of two materials (iron and constantan) [12] [4].

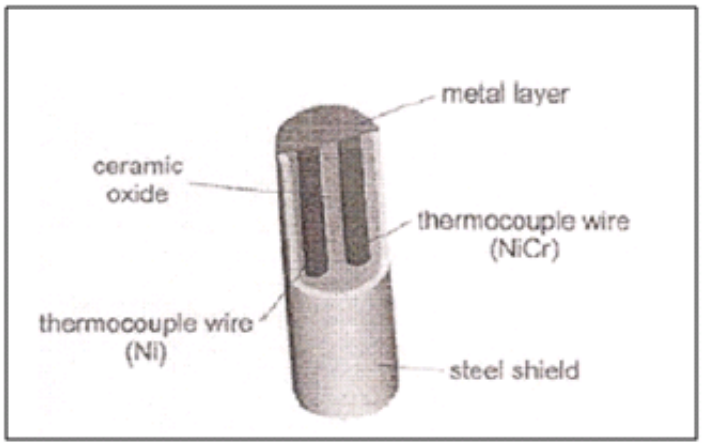

Figure 2.6: Pair wire type thermocouple. Figure taken from [4].

Pair-wire type thermocouple gauges

An example of a pair-wire thermocouple is shown in figure 2.6. As can be seen in the figure, the two leads of the thermocouple are made of metals and inserted into an insulation tube. These two leads are surrounded by a ceramic oxide layer as an insulation medium, to prevent contact between the leads and the tube. The ends of the pair leads are connected by a vacuum-deposited plating as a hot junction. Demuynck et al. [4] stated that Hohenberg [48] and Wimmer et al. [49] used this type of thermocouple [12] [4].

A pair ribbon type is an example of this category but with pair ribbons instead of wires. The pair ribbon type is shown in figure 2.7. The two thin ribbons replace the wires and the mica sheets are used as an electrical insulation. This type of thermocouple was used by Alkidas [29]. Buttsworth [50] showed that, there is a degree of inaccuracy in the derived heat flux measurements due to the influence of the two-dimensional transient heat conduction effects on the surface temperature measurements using this type of thermocouples [12] [4].

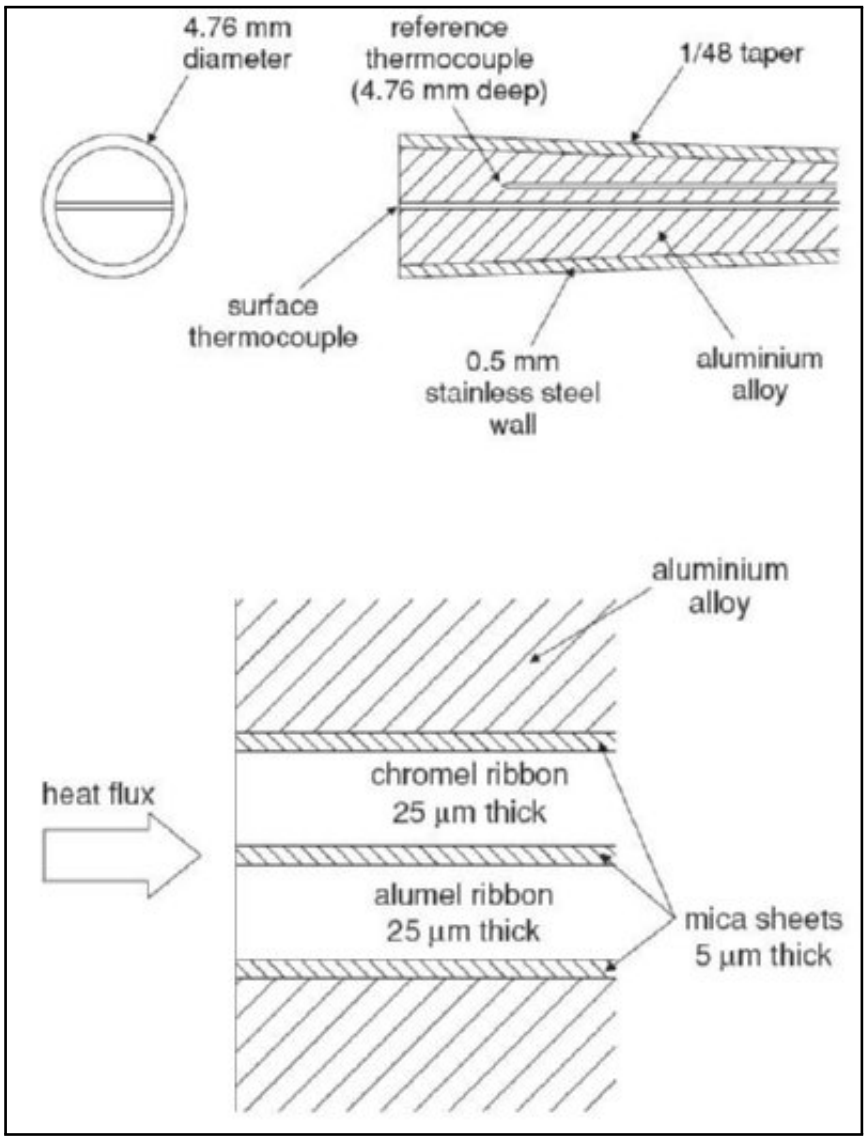

Figure 2.7: Pair ribbon type thermocouple. Figure taken from [4].

Coaxial type thermocouple gauges

This type of thermocouple was first used by Bendersky [51] to measure gun bore surface temperatures. Since his paper, many surface thermocouples of this type have been designed and refined to meet the needs for heat transfer measurements in engine research. A typical coaxial-type surface thermocouple can be seen in figure 2.8. Borman and Nishiwaki [12] reported that this type of thermocouple was used by LeFeurve et al. [52], Oguri and Aizawa [53] and Sihling

and Woschni [54]. As seen in the figure, the centre wire (second thermocouple element) was made of nickel or constantan, coated with insulation and put into the iron tube, (first thermocouple element). The iron tube was threaded for insulation. The end of the probe was plated with a vacuum-deposited thin layer of metal (in the order of $1\mu m$ thick). A hot junction was formed at the interface between the metal plating and the end of the body [12] [4].

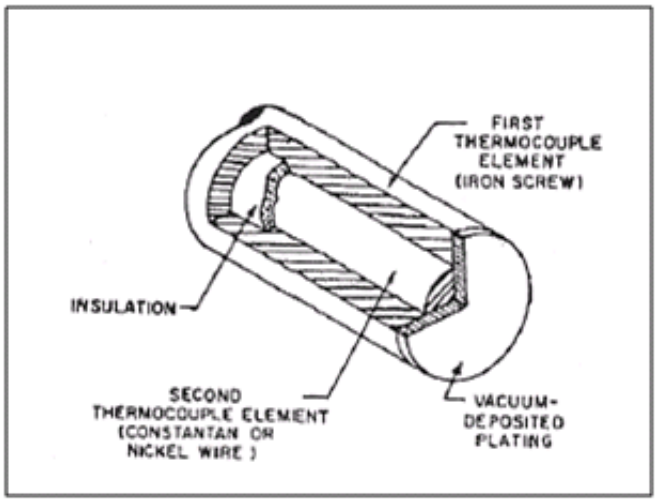

Figure 2.8: Coaxial type thermocouple. Figure taken from [4].

Yoshida et al. [55] made and used the surface thermocouple shown in figure 2.9. This thermocouple has the same construction in principle as the co-axial thermocouple. The constantan cylinder has two inner wires made of copper, one being used to detect the instantaneous surface temperature, and the other used to obtain the steady heat flux component. Ceramic was used as an insulation medium between those two wires and the constantan, as well as around the constantan, to ensure one-dimensional heat flow [12] [4].

The general aim and the principle of the application of the coaxial type thermocouple for the heat flux measurement, is to measure the surface temperature of a body which can be considered as a semi-infinite solid. This type of thermocouple can be made very small, which decreases the response time, due to the smaller thermal mass that needs to be heated to a specific temperature. A very important

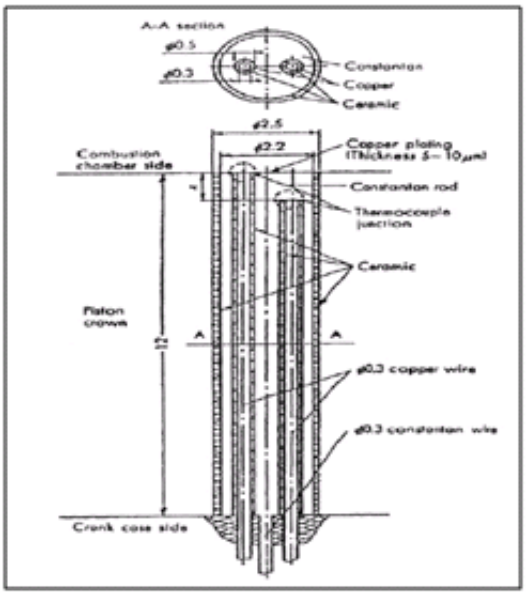

Figure 2.9: Yoshida type thermocouple. Figure taken from [4].

issue which needs to be considered when using the coaxial type of thermocouple is to ensure that the physical properties of the thermocouple are closely matched with the physical properties of the wall material. Furthermore, the thermal product ($\rho k c_p$) of the thermocouple and that of the wall should be similar or very close to each other (see section 5.2.2 for details about the thermal product and its values). This feature is possible if it is considered that the thermocouple can be made from almost any two materials. The thermocouple can be made to have physical properties close to that of the wall, by using one material with thermophysical properties as those of the wall, and the other material as a very thin wire. The average value of the two coaxial thermocouple material properties can be used for the thermocouple thermal product [56] [57], provided these properties are not too different.

In this study the coaxial type thermocouple was chosen to measure the surface temperature for the following reasons:

- The coaxial thermocouples can be made very small.
- They can be installed flush with the surface and therefore not interfere with

the gases flow over the surface.

- The material of these thermocouples can be chosen with physical properties which are very close to that of the wall.
- Due to their design, the coaxial thermocouples are easy to use, very robust and they are able to tolerate the harsh environmental conditions such as those in internal combustion engines.

In addition to the above reasons, there are two more advantages of the coaxial thermocouple technique which are, its fast response time ($\sim 50\mu s$) and very good durability [57].

Chapter 3

Turbulent Thermal Conductivity and the Unsteady Model

3.1 Introduction

The analysis of the turbulence motion in internal combustion engines is important in the development of engine performance. The turbulence can be created by the flow over the inlet valves. The intake jet in the form of swirl, tumble or combinations thereof creates a large scale rotating charge motion. Close to top dead centre the turbulence increases due to tumble breakdown in engine designs which generate tumble. More turbulence around top dead centre is created by late inlet valve closing, combined with low valve lift. Local changes and unsteadiness in the in-cylinder heat transfer is strongly affected by the turbulence motion. The significant effect of the combustion process on engine heat transfer is due to the rapid increase of density, temperature and pressure during the combustion stage. Particulary in SI engines, the flame propagation separates the in-cylinder charge into two zones, burned and unburned, which creates a great local change in heat transfer. During the intake and compression strokes the turbulence has strong effects on the mixing of air, fuel and residual gases. The piston speed

also affects the turbulence in internal combustion engines because the Reynolds number is proportional to piston speed.

In the numerical studies and simulations of internal combustion engines, the modelling of engine heat transfer is a very important issue. The prediction of thermal condition in engines strongly depends on the accuracy of engine heat transfer prediction. Inaccurate prediction of cylinder thermal conditions would have an adverse effect on the accurate simulation of engine performance and combustion process. Thus, accuracy in predicting engine heat transfer is a precondition for the accuracy in predicting the engine performance.

A thermal boundary layer model which employed a turbulent conductivity was proposed by Yang and Martin [58]. In this model, the empirical correlation for turbulent thermal conductivity was used to solve the linearised thermal boundary layer equation. The results of their model showed a good agreement when compared to a motored experimental data. The characteristic length which is a function of fluctuation velocity was involved in the turbulent conductivity, which makes their model strongly dependant on the selection of fluctuation velocity. The model proposed by Han and Reitz [59] considered a variable density but assumed that the kinematic viscosity is constant. The KIVA 3V heat transfer model [60] is widely used and it considers the turbulent conductivity effects. However, in this model the density and viscosity across the thermal boundary layers are assumed to be constant. Moreover, the laminar thermal conductivity and turbulent Prandtl number variation are not considered. In this study, a heat transfer model is presented in which the effect of the variation of turbulent Prandtl number and turbulent viscosity on the turbulent thermal conductivity through the boundary layer is considered.

In this chapter the derivation of the unsteady, one-dimensional heat conduction equation will be presented. An effective variable turbulent thermal conductivity model with the application of different models for the turbulent Prandtl number and the turbulent viscosity will also be discussed in order to apply it to the

unsteady heat transfer model. The variation of the turbulent kinetic energy during the engine cycle is also needed and a model for this quantity is also discussed.

3.2 Unsteady thermal boundary layer model.

In this section the derivation of the unsteady one-dimensional heat conduction equation that can be conveniently implemented via a finite difference formulation is presented [61].

The unsteady energy equation can be expressed as (e.g. [62] [63])

$$\rho \frac{Dh}{Dt} = \frac{Dp}{Dt} + \nabla . k \nabla T + \dot{Q} \tag{3.1}$$

where $\frac{D}{Dt}$ is the total derivation composed of the local time derivative and the convective derivative.

$$\frac{D}{Dt} = \frac{d}{dt} + V . \nabla \tag{3.2}$$

Equation 3.1 is quite general in that it applies to an unsteady, compressible, viscous, heat conducting fluid. The final term of the right hand side of equation 3.1 is a source term and refers to the rate at which energy is delivered into the volume of fluid by means other than conduction.

To apply equation 3.1, a Cartesian coordinate system is considered and x is taken as the direction perpendicular to the wall and property gradients along the wall (i.e. in directions y and z) are neglected. The pressure is assumed to be uniform throughout the boundary layer and the viscous dissipation is neglected.

The unsteady energy equation can therefore be written as.

$$\rho\frac{\partial h}{\partial t} + \rho u\frac{\partial h}{\partial x} = \frac{\partial p}{\partial t} + \frac{\partial}{\partial x}(k\frac{\partial T}{\partial x}) + \dot{Q} \tag{3.3}$$

Approximating the boundary layer gas as calorically perfect, the energy equation in Cartesian coordinates becomes:

$$\rho c_p\frac{\partial T}{\partial t} + \rho u c_p\frac{\partial T}{\partial x} = \frac{\partial p}{\partial t} + \frac{\partial}{\partial x}(k\frac{\partial T}{\partial x}) + \dot{Q} \tag{3.4}$$

Some positions within the engine may be best described by cylindrical or spherical coordinates systems, rather than Cartesian. When this is the case, the equivalent approximation used to arrive at equation 3.4 is that gradients in the θ and z directions in the cylindrical case, and θ and ϕ in the spherical case can be neglected. Therefore, equation 3.4 can be rewritten in a more general form as:

$$\rho c_p\frac{\partial T}{\partial t} + \rho u c_p\frac{\partial T}{\partial x} = \frac{\partial p}{\partial t} + \frac{\partial}{\partial r}(k\frac{\partial T}{\partial r}) + \frac{\sigma}{r}k\frac{\partial T}{\partial r} + \dot{Q} \tag{3.5}$$

Where σ is a switch corresponding to the different coordinate systems: $\sigma = 0$ for Cartesian; $\sigma = 1$ for cylindrical and $\sigma = 2$ for spherical.

Dividing throughout by T_∞, the time-dependent temperature external to the boundary layer (independent of the spatial coordinate) and the product ρc_p yields:

$$\frac{1}{T_\infty}\frac{\partial T}{\partial t} - \frac{1}{\rho c_p}\frac{1}{T_\infty}\frac{\partial p}{\partial t} - \dot{Q} = \frac{1}{\rho c_p}\frac{1}{T_\infty}\frac{\partial}{\partial r}(k\frac{\partial T}{\partial r}) + \frac{\sigma}{r}\frac{k}{\rho c_p}\frac{1}{T_\infty}\frac{\partial T}{\partial r} - u\frac{1}{T_\infty}\frac{\partial T}{\partial r} \tag{3.6}$$

Defining the temperature ratio as.

$$\phi = \frac{T}{T_\infty} \tag{3.7}$$

The first term on the left hand side of equation 3.6 can be expressed as.

$$\frac{1}{T_\infty}\frac{\partial T}{\partial t} = \frac{\partial \phi}{\partial t} + \frac{\phi}{T_\infty}\frac{\partial T_\infty}{\partial t} \tag{3.8}$$

Taking the equation of state as:

$$\rho = \frac{P}{RT} \tag{3.9}$$

Substitution of equation 3.8 into equation 3.6 gives:

$$\frac{\partial \phi}{\partial t} + \frac{\phi}{T_\infty}\frac{\partial T_\infty}{\partial t} - \frac{R}{c_p}\frac{\phi}{p}\frac{\partial p}{\partial t} - \frac{R}{c_p}\frac{\phi}{p}\dot{Q} = \frac{1}{\rho c_p}\frac{\partial}{\partial r}(k\frac{\partial \phi}{\partial r}) + (\frac{\sigma}{r}\alpha - u)\frac{\partial \phi}{\partial r} \tag{3.10}$$

where α is the thermal diffusivity. Equation 3.10 can be rewritten as:

$$\frac{\partial \phi}{\partial t} + \frac{\phi}{c_p T_\infty}(c_p\frac{\partial T_\infty}{\partial t} - v_\infty\frac{\partial p}{\partial t} - v_\infty\dot{Q}) = \frac{1}{\rho c_p}\frac{\partial}{\partial r}(k\frac{\partial \phi}{\partial r}) + (\frac{\sigma}{r}\alpha - u)\frac{\partial \phi}{\partial r} \tag{3.11}$$

where v_∞ is the specific volume of the gas external to the thermal boundary layer. Noting that the first law for a closed system can be written:

$$c_p dT - v dp = \delta q \tag{3.12}$$

the second term on the left hand side of equation 3.11 will be zero for two cases: (i) the source term is zero throughout the region; and (ii) the source term is constant throughout the region. Under either of these conditions, the final form of the energy equation that will be used in the present simulations can be written

as:

$$\frac{\partial \phi}{\partial t} = \frac{1}{\rho\, c_p} \frac{\partial}{\partial r} \left(k\, \frac{\partial \phi}{\partial r} \right) + \left(\frac{\sigma}{r} \alpha - u \right) \frac{\partial \phi}{\partial r} \tag{3.13}$$

To solve the above equation, boundary and initial conditions are needed. The wall boundary condition at $(r = r_0)$ is

$$\phi\,(r_0, t) = \frac{T\,(r_0, t)}{T_\infty(t)} = \frac{T_w(t)}{T_\infty(t)} = f\,(t) \tag{3.14}$$

and a second boundary condition arises from the behaviour of the gas external to the boundary layer $(r \rightarrow \infty)$

$$\phi\,(\infty, t) = \frac{T\,(\infty, t)}{T_\infty(t)} = 1 \tag{3.15}$$

The initial condition is:

$$\phi\,(r, 0) = g\,(r) \tag{3.16}$$

For planar systems, equation 3.13 can be conveniently solved via transformation to a Lagrangian coordinate system which eliminates the normal velocity term. For example, Yang and Martin [58] adopted the Lagrangian transformation approach, and Borman and Nishiwaki [12] have identified a number of earlier workers also adopting this approach. However, for cylindrical or spherical systems, such a transformation does not lead to a useful simplification.

In [61], to evaluate the velocity term u from the continuity equation, a direct numerical approach has been adopted as follows.

The total mass within the boundary layer between the surface (r_0) and a certain

point within the boundary layer r is given by,

$$m = \int_0^r \rho \; A \; dr \tag{3.17}$$

Where the area $A \sim r^\sigma$ for the different coordinate systems. The velocity in the direction of increasing r will therefore be given by

$$u = \; -\frac{1}{\rho A}\frac{dm}{dt} = \; -\frac{1}{\rho A}\frac{d}{dt} \; \int_0^r \rho(r') \; A(r') \; dr' = \; -\frac{1}{\rho \; r^\sigma}\frac{d}{dt}\int_0^r \rho\,(r')\, r'^\sigma dr' \tag{3.18}$$

A significant feature of the above energy equation formulation (equation 3.13) is that it can be applied when the combustion occurs. This is not a point that other workers have emphasised. The normal approach is to claim that the gas external to the boundary layer is adiabatic and thus the pressure, which is uniform across the thermal boundary layer, is related to the external temperature via the normal isentropic relationship. When combustion occurs, it is clear that the pressure and temperature in the core region (external to the boundary layer) will not follow an isentropic relationship. However, the derivation of the unsteady model emphasizes the fact that the equation 3.13 can be applied even when combustion occurs.

The one-dimensional heat conduction equation is then implemented in the finite difference routine for the solution of transient one dimensional heat conduction problem built in Matlab. This Matlab routine provides the boundary layer heat flux based on a finite difference solution of one dimensional unsteady energy equation for the case of variable thermal properties within the boundary layer. The gas properties required to run this routine are identified from the quasi-steady Matlab program discussed in section (4.3). The finite difference Matlab routine will be used in this study in the examination of the unsteady heat transfer model.

3.3 Turbulent thermal conductivity

The unsteady model discussed in the previous section has a wide range of usage options; it can be used for cartesian, spherical and cylindrical coordinates. Moreover, it can accommodate a non-isentropic variation of gas properties external to the boundary layer in addition to the variable thermal conductivity within the boundary layer. Such options make it suitable for internal combustion engines heat transfer modelling. In this section the addition of a variable turbulent thermal conductivity to this model will be presented. The turbulent thermal conductivity within the boundary layer can be expressed as [64]:

$$K_t = \frac{c_p \mu_t}{Pr_t} \tag{3.19}$$

3.3.1 Turbulent Prandtl number correlations

For simplicity, a constant value for the turbulent Prandtl number is usually assumed [65] [66]. In this study, constant values for the turbulent Prandtl number ranging from 0.7 to 0.9 will be used, in addition to variable values derived from some empirical formulas. Most of the correlations available for modelling the turbulent Prandtl number are derived from pipe flow data, and it seems that specific models are not available for internal combustion engine flows. Churchill [67] found that the turbulent Prandtl number is only a function of (μ_t/μ) (the ratio of the turbulent viscosity to the molecular viscosity) and the molecular Prandtl number (Pr). Jischa and Rieke [68] found that for low Prandtl numbers the turbulent Prandtl number depends strongly on the molecular Prandtl number. The following correlations for the turbulent Prandtl number were developed for different boundary conditions, but generally they are applicable for heat transfer in a fully developed turbulent pipe flow. One of the empirical formulas for the turbulent Prandtl number that describes the turbulent flow in pipes propose by Jischa and

Rieke [68] is expressed as:

$$Pr_t = 0.85 + BPr^{-1} \tag{3.20}$$

where B=0.012 to 0.05 and applied for Re=2×10^4.

The following equation which describes the variation in turbulent Prandtl number was developed by Myong et al. [69]:

$$Pr_t = 0.75 + \frac{1.63}{\ln\left(1 + Pr/0.0015\right)} \tag{3.21}$$

for $10^{-2} < Pr < 10^4$ and $10^4 < Re < 10^5$.

The formula proposed by Graber [70] and cited by Jischa and Rieke [68] describes the turbulent Prandtl number as a function of the molecular Prandtl number in the form :

$$Pr_t = \frac{1}{0.91 + 0.13Pr^{0.545}} \tag{3.22}$$

applicable for $0.7 < Pr < 100$.

Based on the suggestion of Kays [71] another formula for the variable turbulent Prandtl number was proposed in the form:

$$Pr_t = \frac{0.7}{Pr\mu^+} + 0.85 \tag{3.23}$$

Another formula was proposed by Kays and Crawford [72] and presented by

Kays [71] as the following expression:

$$Pr_t = \{0.5882 + 0.228\mu^+ - 0.044(\mu^+)^2[1 - \exp{(\frac{-5.165}{\mu^+})}]\}^{-1} \tag{3.24}$$

Notter and Sleicher [73] developed a correlating equation for the turbulent Prandtl number in the form:

$$Pr_t = \frac{1+\phi}{[0.025Pr\mu^+ + \phi][1 + \frac{10}{35+\mu^+}]} \tag{3.25}$$

where $\phi = 90Pr^{1.5}(\mu^+)^{0.25}$.
The above equation can be applied for $10^4 < Re < 10^6$ and $0 < Pr < 10^4$.

In the above equations μ^+ is the ratio of the turbulent viscosity to the molecular viscosity and Pr is the molecular Prandtl number, which is defined as the ratio of momentum diffusivity (kinematic viscosity) to thermal diffusivity and it is expressed as:

$$Pr = \frac{\nu}{\alpha} = \frac{c_p\mu}{K} \tag{3.26}$$

The thermal conductivity in the above equation is calculated based on the gas temperature in the combustion chamber in the form [41]:

$$K = 3.17 \times 10^{-4} T_g^{0.772} \tag{3.27}$$

and similarly the molecular viscosity is calculated in the form [41]:

$$\mu = \frac{3.3 \times 10^{-7} T_g^{0.7}}{1 + 0.027\phi} \tag{3.28}$$

where ϕ is the equivalence ratio.

Finally, the formula proposed by Reynolds [74] in the form:

$$Pr_t = \{(1 + 100Pe^{-0.5})[(1 + 120Re^{-0.5})^{-1} - 0.15]\}^{-1} \tag{3.29}$$

In the above equation, Pe is the Peclet number which is defined as Prandtl number multiplied by Reynolds number.
Equation 3.29 can be applied for $Re < 1.7 \times 10^5$.

The equations presented above (Eqs. 3.20- 3.29) alongside with constant values for the Prandtl number will be considered in this study in order to investigate the effect of the variation of turbulent Prandtl number on the turbulent thermal conductivity and consequently on the heat transfer in internal combustion engines.

3.3.2 Turbulent viscosity correlations

The turbulent viscosity term appears in the turbulent thermal conductivity correlation in equation 3.19 and in some of the expressions for the turbulent Prandtl number, needs to be defined.

In the two-equation $k - \omega$ model, k is the turbulence kinetic energy and ω is the specific dissipation rate which can be calculated using the following expression [75]:

$$\omega = \frac{Turbulence\ dissipation\ rate}{Turbulence\ kinetic\ energy\ \times \beta^*},\ \beta^* = 0.09 \tag{3.30}$$

This correlation is proposed by Wilcox [75] and is widely used in the definition of ω. The Wilcox $k - \omega$ model gives good results for both wall bounded flows and

free shear flows because of the low Reynolds number correction factors, which makes it suitable for the engine simulation [76].

Different models that describe the turbulent viscosity using the $k-\omega$ models are available in the literature. Some of the well known models will be presented and used in this study. Wilcox [75] proposed a model for the the turbulent viscosity in the form:

$$\mu_t = \alpha^* \frac{\rho k}{\omega} \tag{3.31}$$

where α^* is the low-Reynolds correction factor. This coefficient is given by:

$$\alpha^* = \frac{0.025 + \frac{Re_t}{6}}{1 + \frac{Re_t}{6}} \tag{3.32}$$

In the above equation Re_t is the turbulent Reynolds number which is suggested to be given by:

$$Re_t = \frac{k}{\nu\omega} \tag{3.33}$$

Another model for the turbulent viscosity is proposed by Peng and others [77] and stated by Bredberg [78] in the form:

$$\mu_t = f_\mu \frac{\rho k}{\omega} \tag{3.34}$$

In the above equation the damping function f_μ is expressed as:

$$f_\mu = 0.025 + [1 - \exp\{-(\frac{Re_t}{10})^{3/4}\}] \times [0.975 + \frac{0.001}{Re_t} \exp\{-(\frac{Re_t}{200})^2\}] \tag{3.35}$$

Bredberg and others [79] suggested another formula for the turbulent viscosity. It was presented by Bredberg [78] as follows:

$$\mu_t = f_\mu \frac{\rho k}{\omega} \tag{3.36}$$

The damping function f_μ is presented in the form:

$$f_\mu = 0.09 + (0.91 + \frac{1}{Re_t^3})[1 - \exp\{-(\frac{Re_t}{25})^{2.75}\}] \tag{3.37}$$

3.3.3 Turbulence kinetic energy model

An approach which describes the temporal variation in turbulence kinetic energy within an internal combustion engine is provided by Lumley [80] and is expressed as a differential equation per unit mass with the absence of gas exchange in the form:

$$\frac{dk}{dt} = P - D \tag{3.38}$$

where P is the turbulence energy production rate per unit mass. In this model the ratio V_c/A_w represents the length scale for mean strain rate and it is the ratio of cylinder volume to the surface area. According to this, the mean strain rate should vary as $|V_P|A_w\backslash V_c$, where V_P is the mean piston speed. The turbulent stress has the dimension of squared velocity. The turbulence energy production rate is given by:

$$P = F_P \frac{A_w}{V_c}|V_P|^3 - \frac{2}{3}k\frac{1}{V_c}\frac{dV_c}{dt} \tag{3.39}$$

In the above equation for the production rate, the first term represents turbulence

production due to the strain in the shear flow on the walls and the effects of compression is represented by the second term of this equation.

In equation 3.38, D represents the turbulence energy dissipation rate per unit mass. It varies as V_t^3/L as is indicated by the turbulence theory, where V_t is the turbulent velocity and L is the scale of the largest turbulent eddies. In engines the turbulence scale is compatible with that of the cylinder, and the dissipation rate model is expressed as [80]:

$$D = F_d \frac{kV_t}{V_c^{1/3}} \tag{3.40}$$

In equations 3.39 and 3.40 F_P and F_d are user-defined constants for scaling the production and dissipation terms respectively. The typical values for these constants as suggested by Lumley are:
During compression

$$F_P = 0.00502$$

$$F_d = 0.298$$

During combustion

$$F_P = 0.03$$

$$F_d = 0.05$$

During expansion

$$F_P = 0.00502$$

$$F_d = 0.298$$

By introducing the meaning and modelling the terms of the production rate and the dissipation rate and putting $V_t = \sqrt{2k}$, the equation 3.38 can then be rewritten as:

$$\frac{dk}{dt} = F_P |V_P|^3 \frac{A_w}{V_c} - \frac{2}{3} k \frac{1}{V_c} \frac{dV_c}{dt} - F_d \sqrt{2} \frac{1}{V_c^{1/3}} k^{3/2} \tag{3.41}$$

The above equation is a first order ODE which can be solved using the Matlab function ODE23. To solve this equation, an initial value for the turbulence kinetic energy (k) needs to be assumed. A representative initial value for the turbulence kinetic energy according to Diwakar [81] is assumed to be 12.5 percent of the square of the mean piston speed as stated by Rao and Bardon [21].

3.3.4 Representative calculations

This section illustrates the assumed relationship between the distance from the wall and the turbulent thermal conductivity and the effect of the thermal boundary layer thickness on the peak heat flux values for the wide open throttle motored case and the fired case operating conditions presented in section 7.3.1 and section 7.4 respectively in chapter 7.

An illustration of the variation of the turbulent thermal conductivity as a function of distance from the wall is presented in figure 3.1 for representative motored conditions at different times during the engine cycle. The figure shows that the assumed turbulent thermal conductivity used in the model varies linearly up to the edge of the boundary layer and remains constant from the boundary layer edge and into the core of the engine charge. The edge of the thermal boundary layer was chosen to be 15.5 mm corresponding to the location of 95 % of maximum temperature variation. Different values for the location of the thermal boundary layer were investigated and no significant effect on the heat flux was observed, as illustrated in figure 3.2. This figure shows that only about 20 % reduction in the peak heat flux was observed for a doubling of the assumed turbulent boundary layer thicknesses.

Figure 3.1 also shows that the turbulent thermal conductivity at the top dead centre is the highest among the three represented crank angle cases, whereas during compression (e.g 30° CA degrees BTDC) it is higher than the expansion (e.g 30° CA degrees ATDC). This level of difference in the magnitude of the

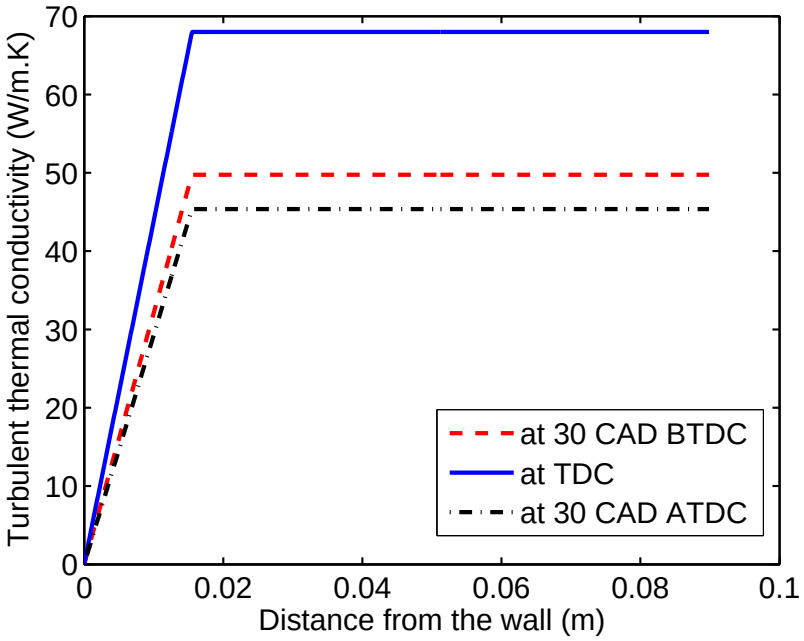

Figure 3.1: Variation of turbulent thermal conductivity as a function of distance from the wall for the WOT motored case.

turbulent thermal conductivity is due to the variation of turbulent kinetic energy obtained from Lumley's model during the engine cycle, as shown in figure 3.3. As it can be observed that the turbulent kinetic energy has its peak near top dead centre then it starts to drop during the expansion stage. This can be identified from equation 3.41 in which the rate of the turbulent kinetic energy is higher during the compression stage when the change in the cylinder volume is negative, which makes the second term of this equation positive and vice versa during the expansion stage. At the top dead centre the rate of change in the cylinder volume is zero, but at that time, the cylinder volume is at its minimum value, which makes the first and the last term of equation 3.41 higher. The assumed thermal boundary layer thickness is correct at 36° CA degrees ATDC, and the simulated thickness of the thermal boundary layer at top dead center is found to be 10 mm.

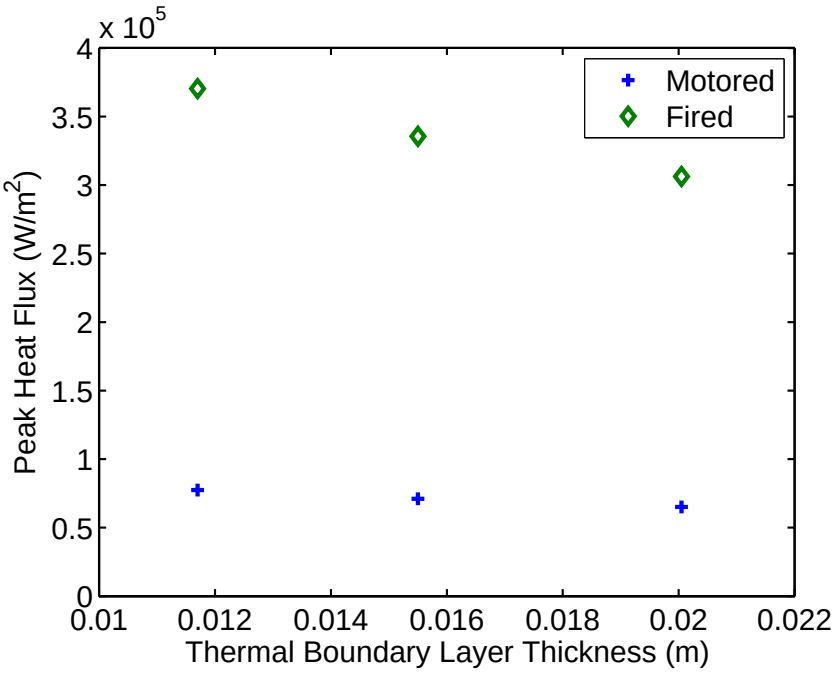

Figure 3.2: Effect of different thermal boundary layer thicknesses on peak heat flux, for the WOT motored case and the fired case.

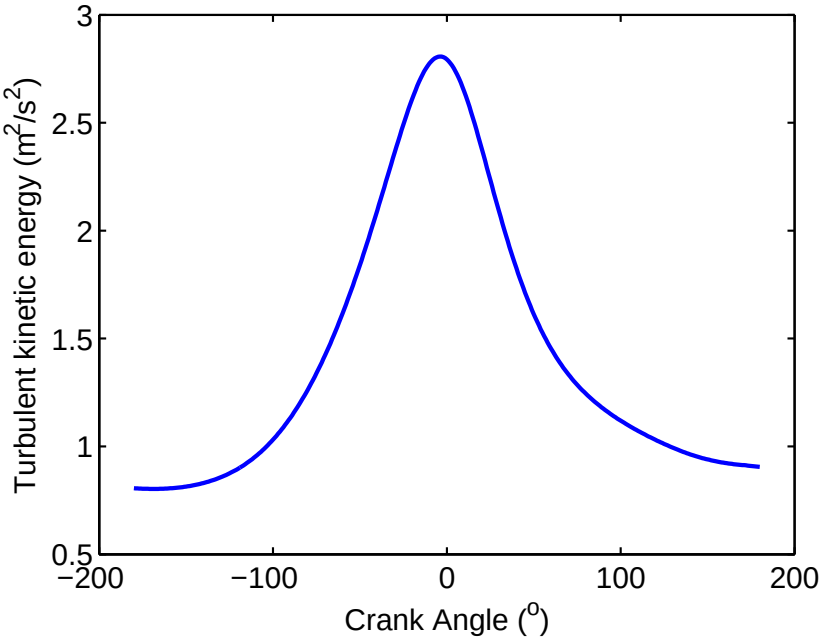

Figure 3.3: Variation of turbulent kinetic energy during the engine cycle for the WOT motored case.

Chapter 4

Simulation of Previous Engine Data

4.1 Introduction

Simulation of engine heat transfer can be used to predict the heat transfer rates from the engine, which are very important for the thermal analysis and engine design. To critically evaluate existing heat transfer models, it is necessary to have data on both instantaneous in-cylinder pressure and heat flux as a function of crank angle, along with engine geometry and fuel and air flow rate data. It seems very few of the previous works on instantaneous engine heat transfer have reported crank-resolved cylinder pressure and heat flux in sufficient detail to enable independent assessment. This chapter will focus on the results obtained from simulating the previous data from the literature for a small number of different engines and conditions. In addition, the results obtained from the unsteady thermal energy equation simulation will be presented. The engine simulations are performed using a quasi one-dimensional spark ignition engine Matlab simulation program. Both the simulated pressure and temperature history were used to calculate the heat transfer coefficient, using different heat transfer models, and

to compare the simulated results with the reported data.

4.2 Types of S.I engine computer models

Two main types of computer model are available for use in engine characteristics prediction. These two models are the fluid dynamic model and the thermodynamic model. The fluid dynamic model is based on the detailed analysis of the in-cylinder fluid flow and the thermodynamics model is generally based on energy and mass conservation within the engine cycle. A brief description of these two models follows.

4.2.1 Fluid dynamic models

The fluid dynamic computer models are called multi-dimensional models, due to the implementation of the flow equations. These models have more ability to predict engine conditions, but they usually take longer for the cycles to be calculated and to set up. The fluid dynamic models can predict the flow field within the engine cylinder, the combustion process and the heat transfer, by numerically solving the governing conservation equations. These are also able to study the process of intake and exhaust gas exchange, by means of one-dimensional unsteady fluid dynamics. Moreover, the turbulence within the flow region can be modelled using full-field modelling or the large eddy simulation. This can include the cycle-by-cycle variation which exists during the engine operation.

4.2.2 Thermodynamic models

In the thermodynamic models there is no flow modelling calculated and therefore the geometric features of fluid motion cannot be predicted. These models are re-

ferred to as zero dimensional models. The thermodynamic models are known as phenomenological and they are called quasi-dimensional models when special geometric features can be added. The thermodynamic computer models must start with the inlet conditions, which include the properties of the inlet gas. In addition the engine geometry must be entered, such as cylinder bore, stroke, connecting rod length and engine speed. Once these details are entered into the model then the model will be able to calculate the required parameters. This includes the rate of change of volume with crank angle, and the change of in-cylinder pressure with respect to the crank angle. The heat transfer rates and the indicated work and efficiency can also be calculated. In this study the thermodynamic computer model is chosen to be used in the engine simulation.

4.3 Simulation using a quasi one-dimensional Matlab program

To perform the simulation for the internal combustion engines and conditions, the model developed by Buttsworth [82] is used. This model is a translation of the work by Ferguson [83] from FORTRAN into Matlab. The overall mass of the reactants is transformed into products according to a specified rate, which followed the cosine burn law during combustion [83]. The local transformation of reactants into products within the flame front is considered instantaneous and the products of combustion are treated as being in chemical equilibrium using the approach of Olikara and Borman [84].

4.3.1 Simulation of pressure and heat transfer data

The crank-resolved pressure and heat transfer data from the work of Wu et al. [5] [6] and Alkidas [7] will be presented and discussed. The designations “en-

gine A" and "engine B" refer to the engines used by Wu et al. [5] [6] respectively and "engine C" refers to the engine used by Alkidas et al. [7]. The engine simulations are performed using a quasi one-dimensional spark ignition engine Matlab simulation program developed by Buttsworth [82]. Both the simulated pressure and temperature history were used to calculate the heat transfer coefficient using different heat transfer models, and to compare the simulated results with the reported data. To perform the engine simulations, some of the essential engine parameters, such as bore, stroke, compression ratio and connecting rod length were reported in the literature. The specifications of their engines are shown in tables 4.1, 4.2 and 4.3 respectively.

Parameter	Value
Compression ratio	9.1:1
Cylinder bore	0.0565 m
Cylinder stroke	0.0495 m
Fuel	Gasoline
Engine capacity	125 cm^3 single cylinder
Valves per cylinder	2

Table 4.1: Specifications of engine A, Wu et al. [5].

Parameter	Value
Compression ratio	10.2:1
Cylinder bore	0.052 m
Cylinder stroke	0.0586 m
Fuel	Gasoline
Engine capacity	125 cm^3 single cylinder
Valves per cylinder	2

Table 4.2: Specifications of engine B, Wu et al. [6].

The work of Wu et al. [5] [6] provided the heat transfer data under different oper-

Parameter	Value
Compression ratio	8.5:1
Cylinder bore	0.0921 m
Cylinder stroke	0.0762 m
Fuel	Iso-octane
Engine capacity	507.6 cm^3 single cylinder
Connecting rod length	0.1463 m

Table 4.3: Specifications of engine C, Alkidas et al. [7].

Parameter	Value
Speed	6000 rpm
Wall temperature	531 K
Half stroke to rod ratio	0.25
Blow-by constant	0.8 s^{-1}
Residual fraction	0.1
Equivalence ratio	0.9
Burn start	15^o BTD
Burn duration	50^o
Initial pressure (180 BTC)	95 kPa
Initial temperature (180 BTC)	370 K

Table 4.4: Operation parameters for simulation engine A, Wu et al. [5].

ating conditions. In this simulation the data are chosen as follows: for engine A, the pressure and heat flux data were provided for the condition 6000 rpm and 6 bar BMEP; for engine B, the data were provided for the condition 6000 rpm and 7 bar BMEP. For the engine used by Alkidas et al. [7] engine C the data were provided for the condition at 1300 rpm and the baseline intake flow configuration. However, for those parameters which were not provided, estimated values were used, or the parameters (such as inlet pressure and temperature) were tuned with reasonable

limits, so the simulated pressure history provided a good match with the experimental results as presented in figures 4.1, 4.2 and 4.3. While many papers have reported instantaneous heat flux data, very few have also reported corresponding in-cylinder pressure data. Without a reported pressure history, the magnitude and phasing of the combustion-induced pressure rise cannot be confidently simulated and hence, the instantaneous bulk gas conditions within the cylinder, which drive the heat transfer process, cannot be reliably simulated. Furthermore, appropriate values for the start and duration of the burning are being used (tuned) in order to simulate the engine's performance accurately. The operation parameters used in the engine simulation process are presented in tables 4.4, 4.5 and 4.6 for the engines A, B and C respectively. It is noted in table 4.4 and 4.5, that unrealistically high values for the wall temperatures are used. Those values were obtained from the tuning process in the simulation to match the measured pressure histories and no further scaling was performed in the heat transfer models in contrast to the approach adopted in chapter 6 where scaled heat transfer models are used.

Parameter	Value
Speed	6000 rpm
Wall temperature	593 K
Half stroke to rod ratio	0.25
Blow-by constant	0.8 s^{-1}
Residual fraction	0.1
Equivalence ratio	0.9
Burn start	16^o BTD
Burn duration	60^o
Initial pressure (180^o BTC)	80 kPa
Initial temperature ((180^o BTC)	320 K

Table 4.5: Operation parameters for simulation of engine B, Wu et al. [6].

The simulation parameters mentioned in the above tables were used in simulating

Parameter	Value
Speed	1300 rpm
Wall temperature	450 K
Half stroke to rod ratio	0.2604
Blow-by constant	0.8 s^{-1}
Residual fraction	0.1
Equivalence ratio	0.92
Burn start	23^o BTD
Burn duration	53^o
Initial pressure (180^o BTC)	70 kPa
Initial temperature ((180^o BTC)	425 K

Table 4.6: Operation parameters for simulation of engine C, Alkidas et al. [7].

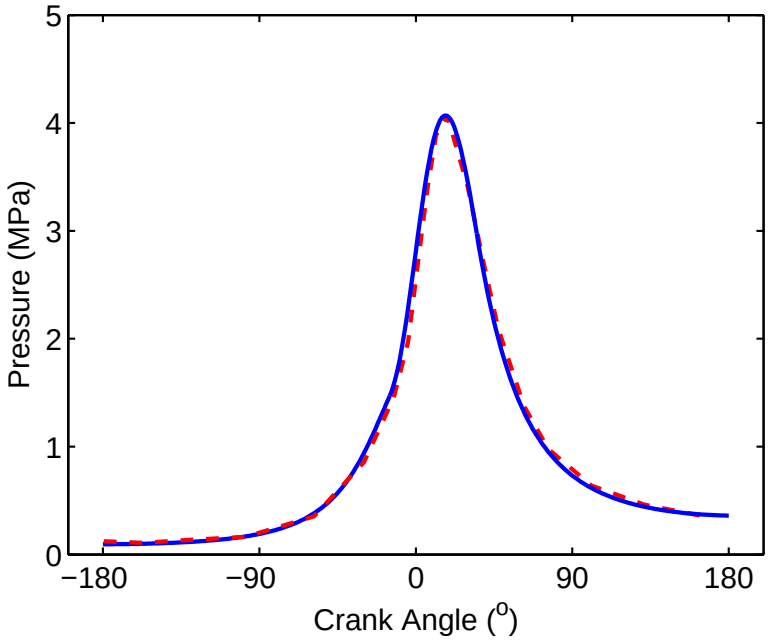

Figure 4.1: Pressure variation with crank angle for engine A operation. Dashed line: data from [5]; solid line: simulated results using Annand's model with initial pressure 95 kPa and initial temperature 370 K.

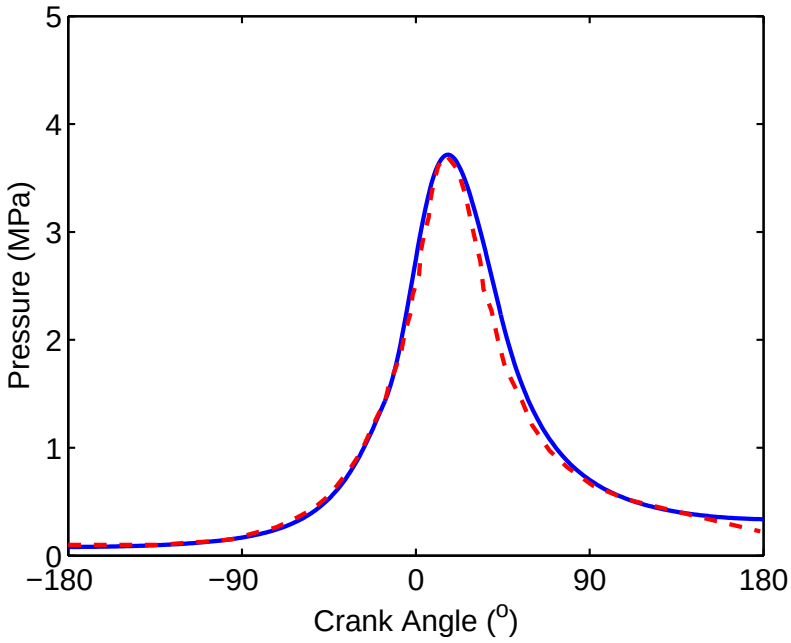

Figure 4.2: Pressure variation with crank angle for engine B operation. Dashed line: data from [6]; solid line: simulated results using Annand's model with initial pressure 80 kPa and initial temperature 320 K.

the pressure history for the engines A, B and C, as presented in the figures 4.1, 4.2 and 4.3 respectively.

Heat transfer data obtained by [5] and [6] for engines A and B is presented in figures 4.4 and 4.5 respectively, along with results from the simulations. Two solid lines are presented in each figure. The first line, which begins at 180 BTDC corresponds to the heat flux determined using the Annand model (Equation 2.7) for the unburned gas. The second, which begins at 23 BTDC for engine A and 16 BTDC for engine B, correspond to the heat flux, again using the Annand model, for the burned zone. There appears to be reasonable agreement between experiments and the simulated result in the initial stages of compression. However, this level of agreement should be regarded as somewhat fortuitous, since only two thermocouple heat flux gauges were used in both engine experiments and these two gauges registered substantially different peak values, which could be due to the inherent spatial variation and the time of flame arrival at the measuring

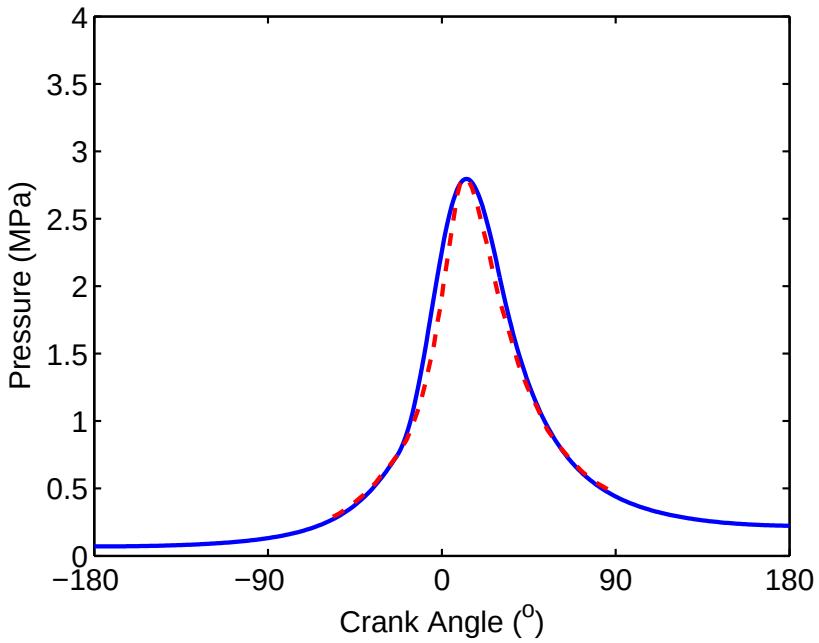

Figure 4.3: Pressure variation with crank angle for engine C operation. Dashed line: data from [7]; solid line: simulated results using Woschnis's model with initial pressure 70 kPa and initial temperature 425 K.

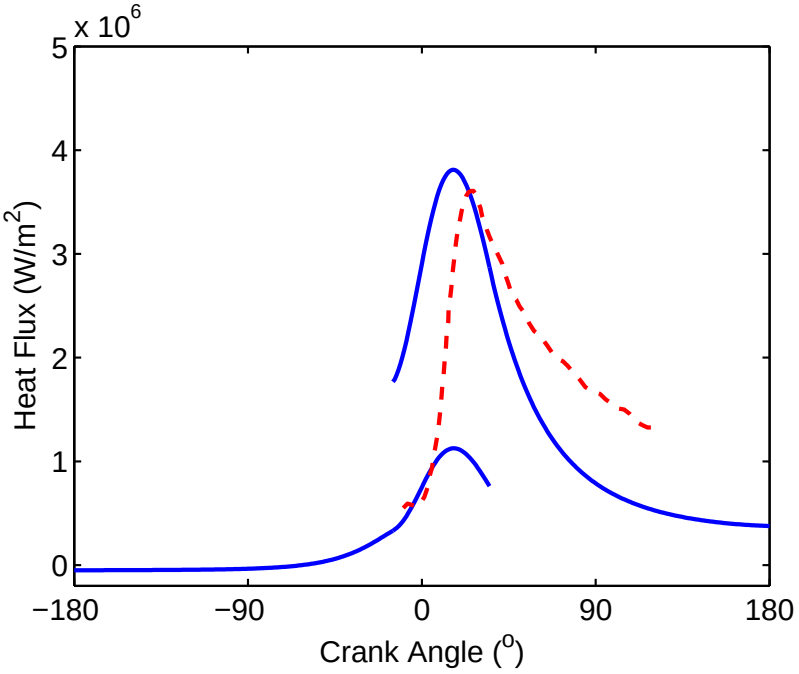

Figure 4.4: Heat flux variation with crank angle for engine A operation. Dashed line: data from [5]; solid line: simulated results using Annand's model.

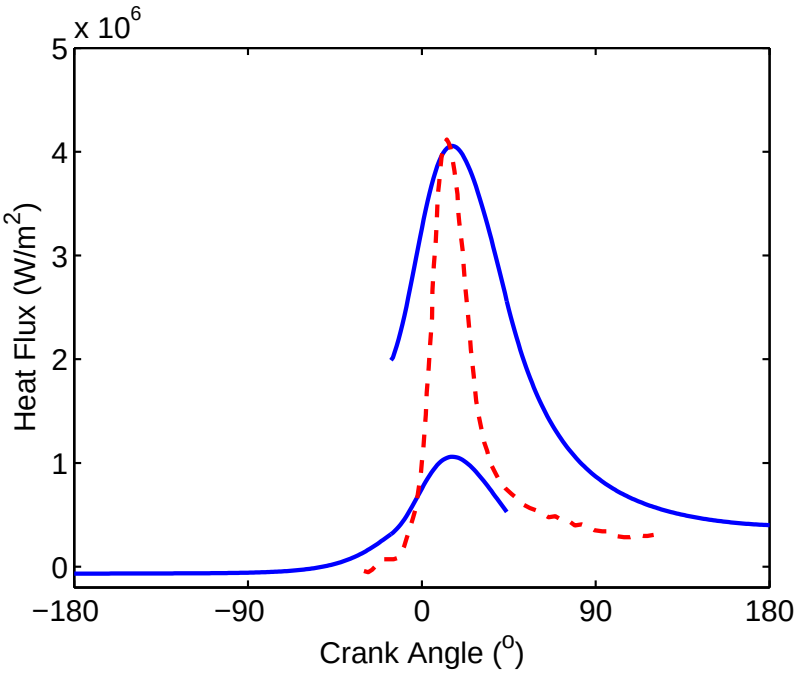

Figure 4.5: Heat flux variation with crank angle for engine B operation. Dashed line: data from [6]; solid line: simulated results using Annand's model.

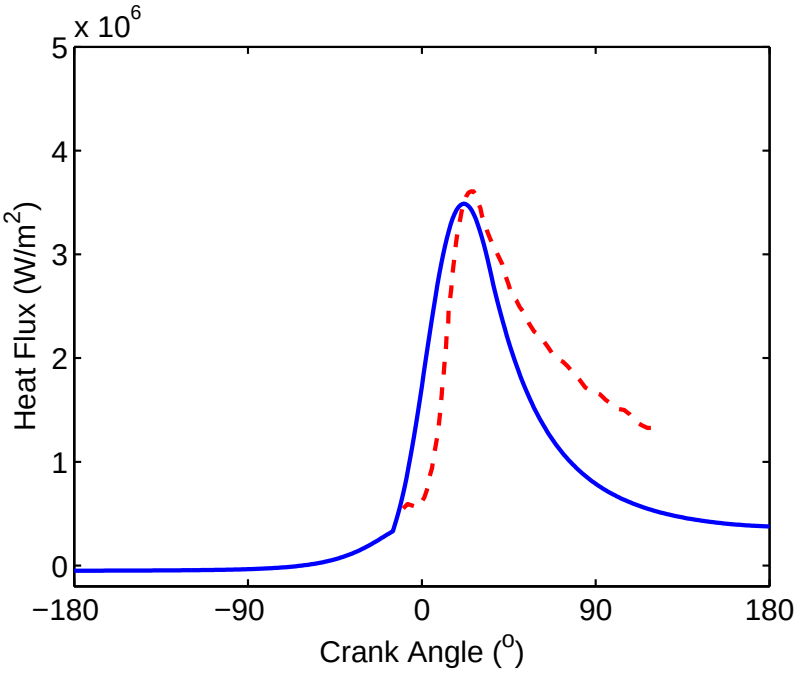

Figure 4.6: Average heat flux variation with crank angle for engine A operation. Dashed line: data from [5]; solid line: simulated results using Annand's model.

positions as observed by different studies as well as the current study (section 6.3). The difference was larger than a factor of 4 for engine A, and a factor of 5 for engine B.

A significant feature of figure 4.4 is the fact that the simulated result appears to fall more rapidly than the measured heat flux. In Figure 4.5 however, the measured heat flux appears to fall more rapidly than the simulated result. The flame arrival at the gauge locations will have a dominant effect on the rise in heat flux observed in the experiments. Since the experimental data represents an averaging of two signals from different locations, it is perhaps reasonable to present the simulated result *averaged* over the unburned and burned zones. This has been done in figures 4.6 and 4.7 for engine A and B respectively.

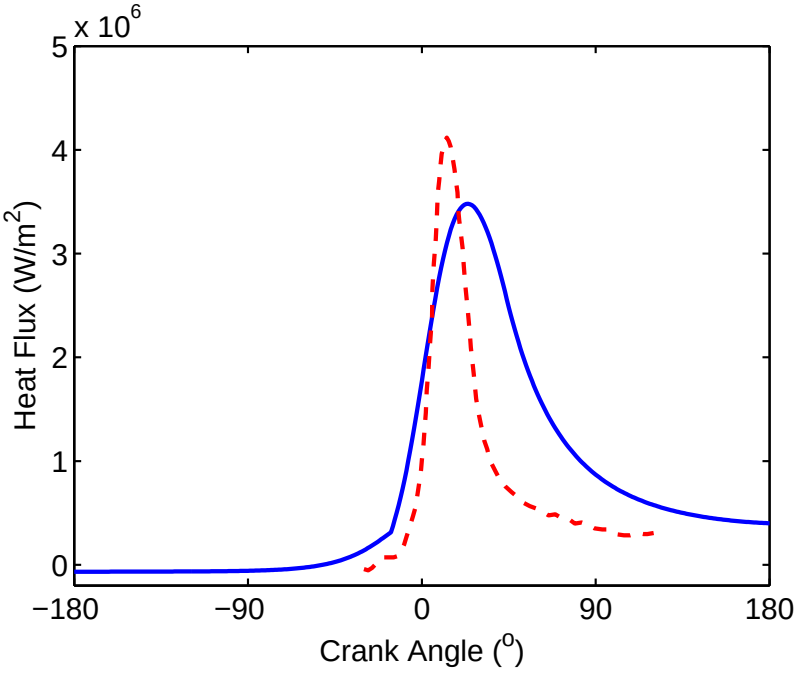

Figure 4.7: Average heat flux variation with crank angle for engine B operation. Dashed line: data from [6]; solid line: simulated results using Annand's model.

The averaged simulation result provides a reasonable representation of the observed timing of the rise in heat flux. However, the rate of fall in the heat flux is not improved through this averaging process. Using the cosine burn law during

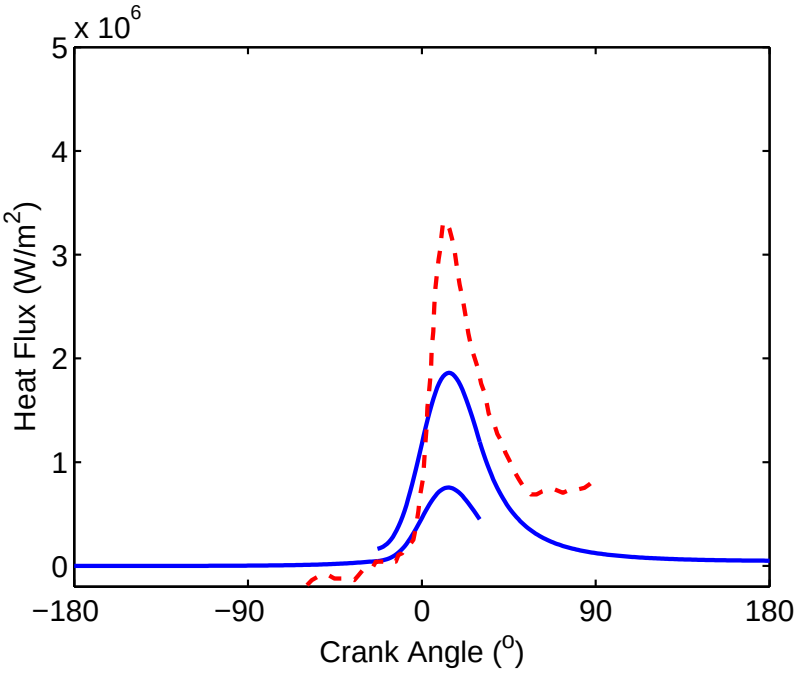

Figure 4.8: Heat flux variation with crank angle for engine C operation. Dashed line: data from [7]; solid line: simulated results using Woschni's model.

combustion in the simulation model might be the reason why the simulated rate of fall in heat flux was not well matched with the measured one.

In the case of engine C, the Woschni model (equation 2.8) was used in the simulation process and the measured heat flux presented in figure 4.8 was obtained by averaging the heat flux at the three locations. In this case the Woschni model was used because of the good agreement that was obtained from the pressure simulation, and also with this model a satisfactory level of agreement was achieved between the calculated and the simulated mass.

It appears in figure 4.8 that the peak value in the measured heat flux is greater than the simulated result by a factor of about 2.5. In figure 4.9 the averaged simulation result is compared with the experimental data and it is observed that the phasing of the rise in the simulated result is similar to the measured (average) heat flux, despite the fact that the peak values are different.

4.3.2 Results from unsteady simulation

The unsteady thermal boundary layer model was run, using the gas properties identified from the engine simulation with the Annand model (equation 2.7) for engine A and B operation and with the Woschni model (equation 2.8) for engine C operation (the heat flux results from which are presented above, section 4.3.1).

Results from the unsteady model are presented in figures 4.10 through to 4.15. In figures 4.10, 4.11 and 4.12 the heat flux in the unburned and burned zones are presented separately, whereas in 4.13, 4.14 and 4.15 the mean heat flux obtained by averaging the results over the instantaneous unburned and burned zone areas is presented.

For the present modelling, a constant effective turbulent conductivity was assumed throughout the thermal boundary layer. The magnitude of this conductivity was assumed to be 50 times larger than the molecular conductivity, following the approach adopted by Lawton [43] in which the turbulent conductivity was taken as being 25 times larger than the molecular conductivity.

The unburned zones simulated heat flux using the unsteady approach for the three engines, is higher than the experimental results for crank angles before top dead centre, figures 4.10, 4.11 and 4.12. Figures 4.10 and 4.12 illustrate that the simulated burned zones heat flux for engines A and C are smaller than the experiments, whereas for engine B the simulated burned zone heat flux is higher than the experiments, as shown in figure 4.11. The peak heat flux values are substantially larger, and occur earlier than the experimental peak values when two separate zones are considered for each of the simulated data, figures 4.10, 4.11 and 4.12.

The phasing of the simulated peaks is improved when the averaged values are considered, but those averaging approaches cause the magnitude of the simulated peaks to underestimate the experimental results (figures 4.13, 4.14 and 4.15).

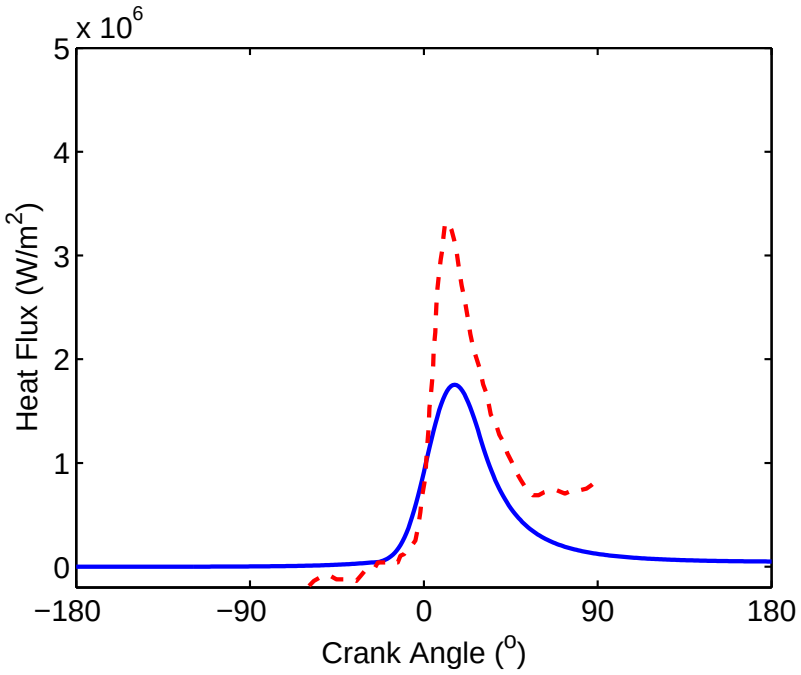

Figure 4.9: Average heat flux variation with crank angle for engine C operation. Dashed line: data from [7]; solid line: simulated results using Woschni's model.

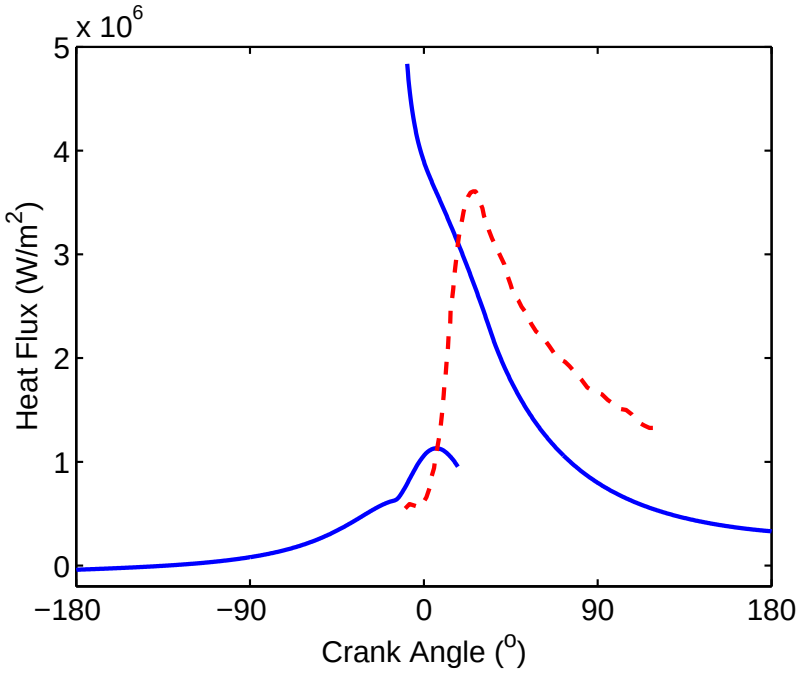

Figure 4.10: Heat flux variation with crank angle for engine A operation. Dashed line: data from [5]; solid line: simulated results using unsteady model.

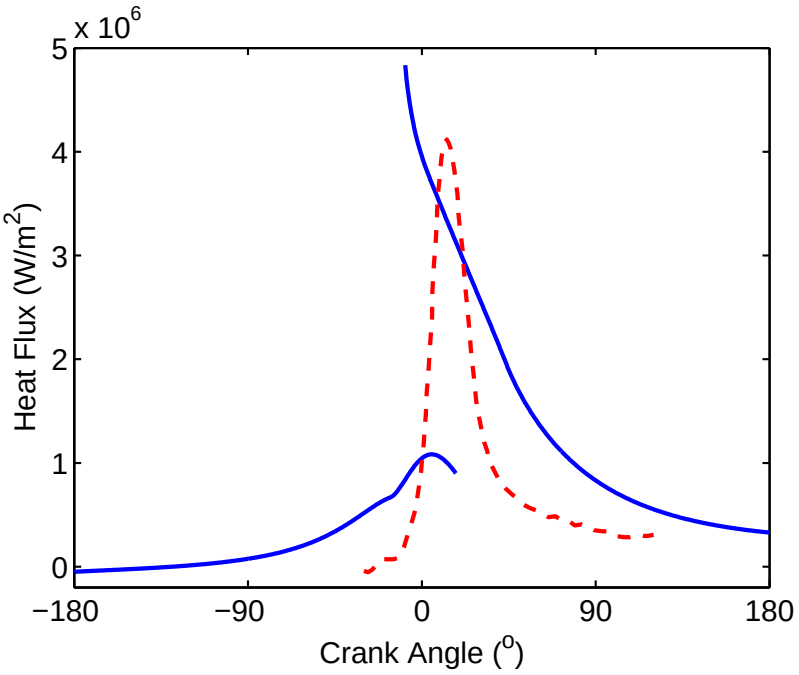

Figure 4.11: Heat flux variation with crank angle for engine B operation. Dashed line: data from [6]; solid line: simulated results using unsteady model.

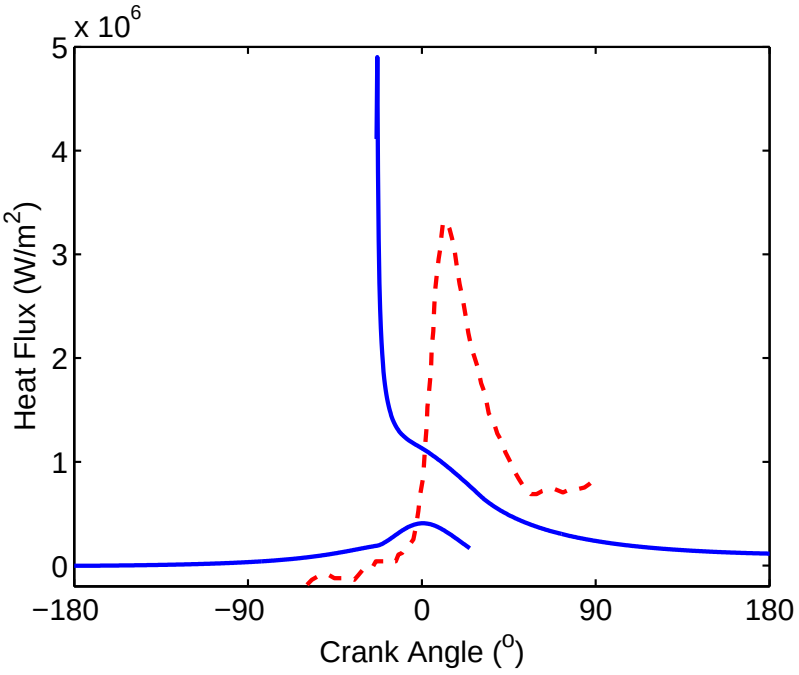

Figure 4.12: Heat flux variation with crank angle for engine C operation. Dashed line: data from [7]; solid line: simulated results using unsteady model.

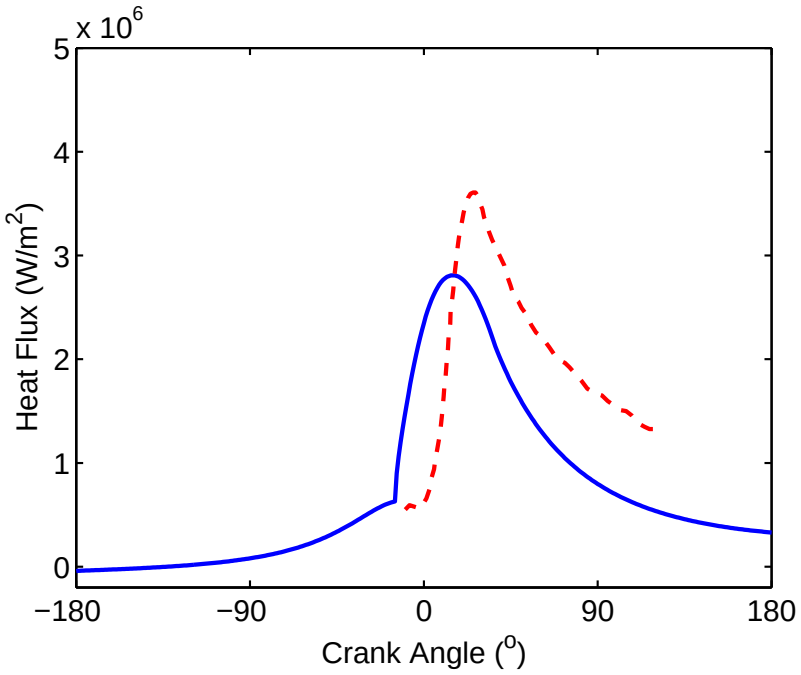

Figure 4.13: Average heat flux variation with crank angle for engine A operation. Dashed line: data from [5]; solid line: simulated results using unsteady model.

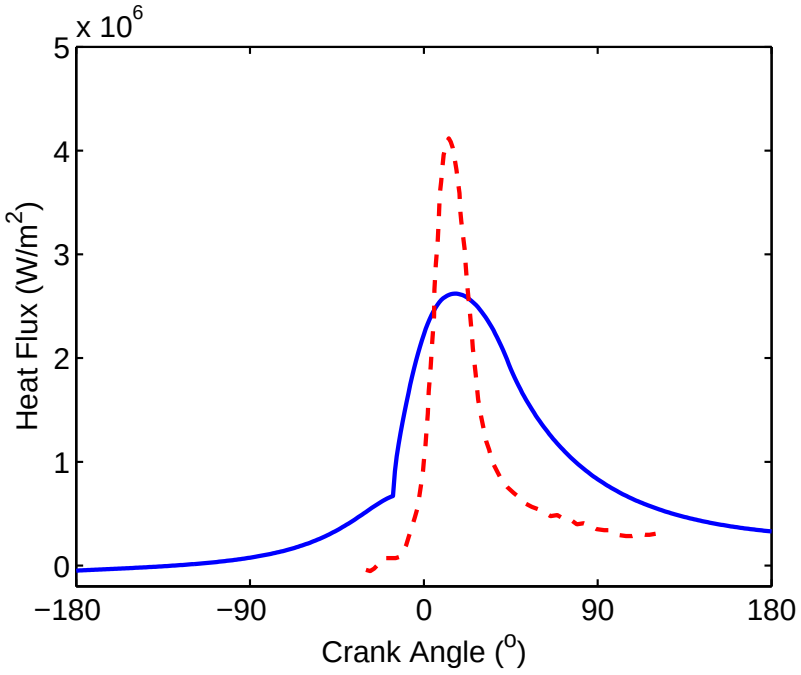

Figure 4.14: Average heat flux variation with crank angle for engine B operation. Dashed line: data from [6]; solid line: simulated results using unsteady model.

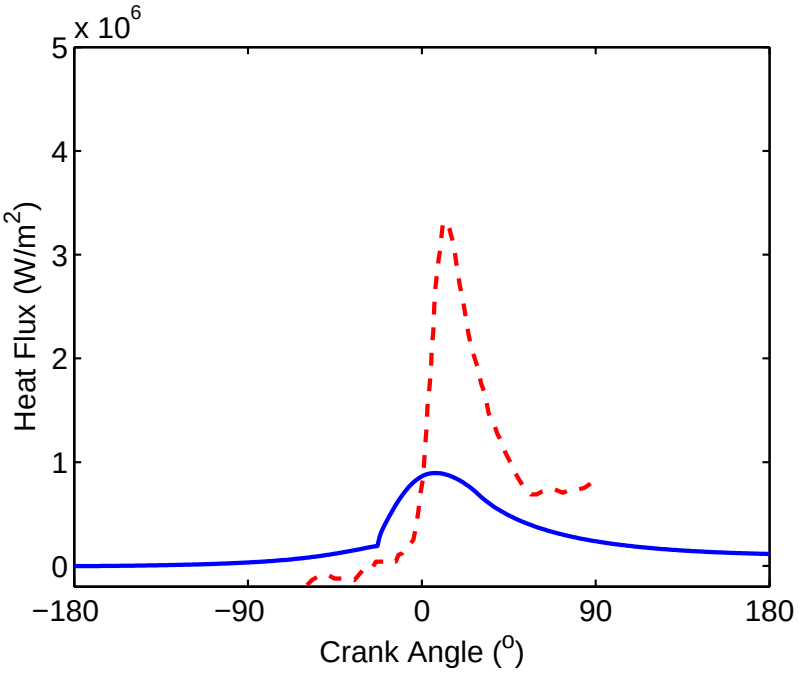

Figure 4.15: Average heat flux variation with crank angle for engine C operation. Dashed line: data from [7]; solid line: simulated results using unsteady model.

4.4 Conclusion

A formulation of the unsteady, one dimensional energy equation for heat flux simulation, applicable for the internal combustion engine environment, was examined. The thermodynamic simulation of three internal combustion engines was performed by tuning the unknown simulation parameters within reasonable limits until the simulated pressure history closely matched the experimental data. Heat flux simulation on the three engines was achieved, using the quasi-steady Annand model for the engines A and B and the Woschni model for the engine C. A good agreement with the experimental measurements was observed on engines A and B. However, the level of agreement is somewhat fortuitous, since internal combustion engine heat flux is a strong function of position, and only two positions were used to derive a supposedly representative, crank-resolve heat flux in the experiments in engines A and B. Three heat flux gauge positions were available from the engine C data so in this case, all three were used to obtain the supposedly

representative heat flux. It can also be concluded that no significant improvement in the simulation of the heat flux measurements was achieved when the unsteady energy equation modelling of the thermal boundary layer was applied. In particular, the rapid fall of the heat flux during the expansion stroke is not accurately captured by the unsteady modelling, despite the fact that considerable success has previously been achieved in this area, using the unsteady energy equation model applied to motored engines. Inaccurate modelling of the effective turbulent conductivity may be a source of error in the present modelling efforts. A constant, but arbitrarily elevated value of thermal conductivity relative to the molecular conductivity was assumed. The unsteady thermal boundary layer simulation may be improved if the spatial and temporal variation in the turbulent conductivity is correctly modelled.

Using an effective turbulent conductivity that varies with crank angle is an important objective which may improve these aspects of the simulation. Moreover, due to the unsteady environment of the internal combustion engines, which generally causes the increase and decrease in the turbulence intensity during compression and expansion processes respectively, there are good prospects for narrowing the heat flux peak simulated by the unsteady approach. An improved approach for more effective turbulent conductivity modelling will be investigated and implemented in the engine simulation.

Chapter 5

Equipment and Test Procedure

5.1 Introduction

This chapter outlines the experimental methods used for the investigations of the heat transfer within a small, four-stoke, spark ignition engine. The engine specifications, the measuring devices, the thermocouple probes fabrication and the whole measurements procedure will be presented in this chapter. The lack of sufficient reporting of pressure history and heat flux data in previous works, in addition to uncertain mass capture values, have made a very strong demand on performing an experimental work to obtain sufficient and reliable pressure and heat flux data to develop the engine heat transfer modelling.

5.2 Experimental equipment and the experimental methods

In this study the heat flux in the engine is first investigated under motored conditions with the variation in the throttle position. The motored test is undertaken

to check the performance of the engine before starting to record the data from the fired engine. This step will help in validating the pressure and temperature measurements and also to validate the crank angle data. In this test the effect of changing the throttle position on the in-cylinder pressure and the heat transfer in the engine is examined. In the case of the motored tests, only the air flows into the combustion chamber and no combustion occurs during this case. From this point, the effect of the gas flow and the turbulence on the heat transfer can be investigated in the absence of the combustion and associated thermal inhomogeneities. Under fired conditions, the engine is tested for only one case with loaded and partly closed throttle setting.

The experimental equipment and set-up will be fully described in the following sections.

5.2.1 The test engine

The engine used for this research at the laboratories of the University of Southern Queensland is a four-stroke, single cylinder, air cooled, spark ignition Kubota engine, model GS200 fueled with gasoline. The detailed engine specifications are given in table 5.1. Some modifications have been made on the engine head to allow for mounting the pressure transducers and the thermocouple probes. Schematic diagram of the test engine set-up is illustrated in figure 5.1. The engine is coupled with a hydraulic dynamometer made by Salami with a load controller panel.

5.2.2 Surface temperature sensors (thermocouples)

This work required the design and and construction of small, accurate and cost-effective gauges (temperature sensor) that can be used to measure the changes in the surface temperature of the engine walls. The temperature sensors are fast-response E-type coaxial thermocouples (Chromel-Constantan). The thermocou-

Engine make and model	Kubota - GS200
Bore	69 mm
Stroke	54 mm
Total displacement	201 cc
Continues H.P	2.83 kW/3600 rpm
Compression ratio	6.0:1.0
Ignition timing	23^o BTDC

Table 5.1: Test engine specifications.

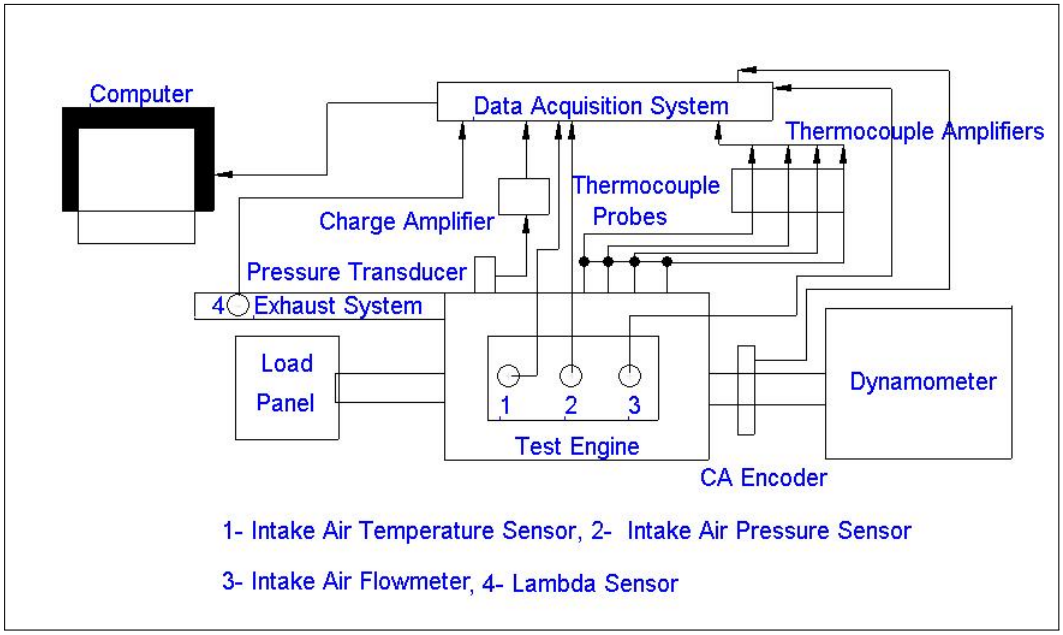

Figure 5.1: Schematic diagram of experimental set-up.

ple probes were designed and assembled by the author in the laboratories of the University of Southern Queensland. The E-type (Chromel/Constantan) coaxial thermocouple is designed and constructed for the purpose of measuring the transient surface temperature of the internal combustion engine wall as a function of time. The design of this thermocouple is shown in figure 5.2. It is one thermocouple element (chromel tube) inserted over the second thermocouple element (constantan wire) with an electrical insulation in between. To establish an electri-

cal insulation layer between the two thermocouple materials, the constantan wire is placed in an oven for about 30 minutes at 850°C prior to assembly to allow the oxidation layer to grow. Then the chromel tube is assembled over the constantan wire to form the E-type thermocouple which then is placed into the furnace for 1 hour at 850°C to achieve a good insulation and bonding. The oxidation layer on the second thermocouple element (constantan wire) is working as an insulation substance between the two materials.

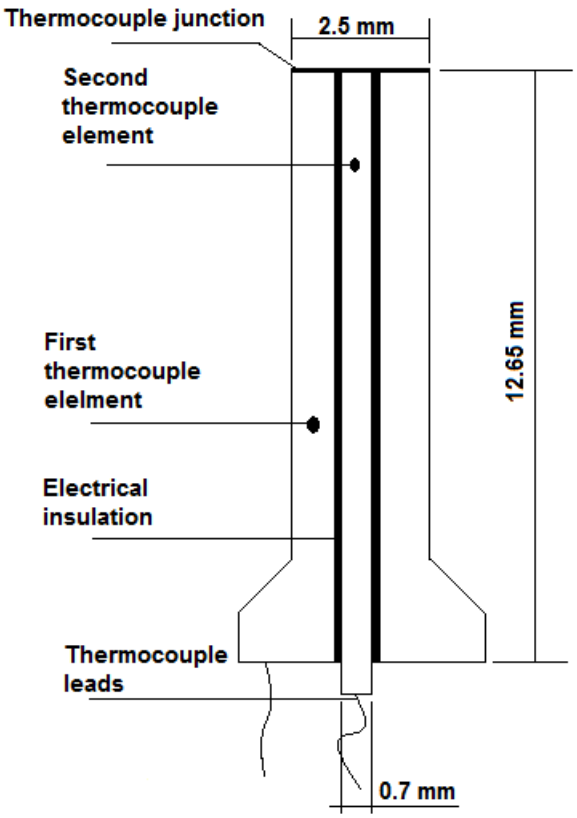

Figure 5.2: The arrangement of the thermocouple probe.

The hot junction of the thermocouple is formed using sandpaper to grind the front surface of the thermocouple and drag the thermocouple materials across the insulation. Sanding the front surface in situ will allow a conformal fit for the thermocouple in the engine walls. Forming the thermocouple hot junction using this method makes the gauge very robust and suitable for the application in harsh environmental conditions. For example, the impact of high speed particles

transported gases in combustion chamber has in general no effect on the operation of the thermocouple. In case of failure, sanding the front surface again activates the thermocouple.

The thermocouple allows a mounting through the wall which is important for accurate measurements for the fast changing surface temperatures. Four thermocouple probes are used and mounted at equal distance of about 5.0 mm intervals along a ray from the spark plug located on the engine head as shown in figure 5.3. The probes are installed flush with the surface of the engine head and they are mounted into the engine head wall by gluing the rear part of the first thermocouple element (chromel tube) to the engine head with an epoxy. For accurate heat flux measurements and to determine the fluctuations in heat flux from the transient surface thermocouple measurements, the thermal product $\sqrt{(\rho c_p k)}$ was defined based on available values for the individual properties ρ, c_p and k for the two separate materials, and emf calibration for the thermocouple probes was performed. The thermal properties of the two thermocouple materials are given in table 5.2. Since the value of $\sqrt{(\rho c_p k)}$ for the two materials differs by only 1 % it was considered reasonable to take the mean $\sqrt{(\rho c_p k)}$ value as that of the thermocouple heat flux gauge.

Thermal property	Chromel	Constantan
Density kg/m^3	8730.243	8912.93
Thermal conductivity W/m.K	19.2	21.2
Specific heat J/kg.K	450	390
$\sqrt{(\rho c_p k)}$ J/m^2.K.s$^{1/2}$	8.68×10^3	8.58×10^3

Table 5.2: Properties of thermocouple materials at room temperature [8] [9].

Because the output of those probes is in microvolts, the signals was amplified and then read in by the data acquisition system (described in section 5.2.5). A Matlab program was then used to convert the voltage data obtained from the thermocouple probe into temperature values, which was then used to deduce the heat

flux through the engine walls, using the thermal properties of the thermocouple materials.

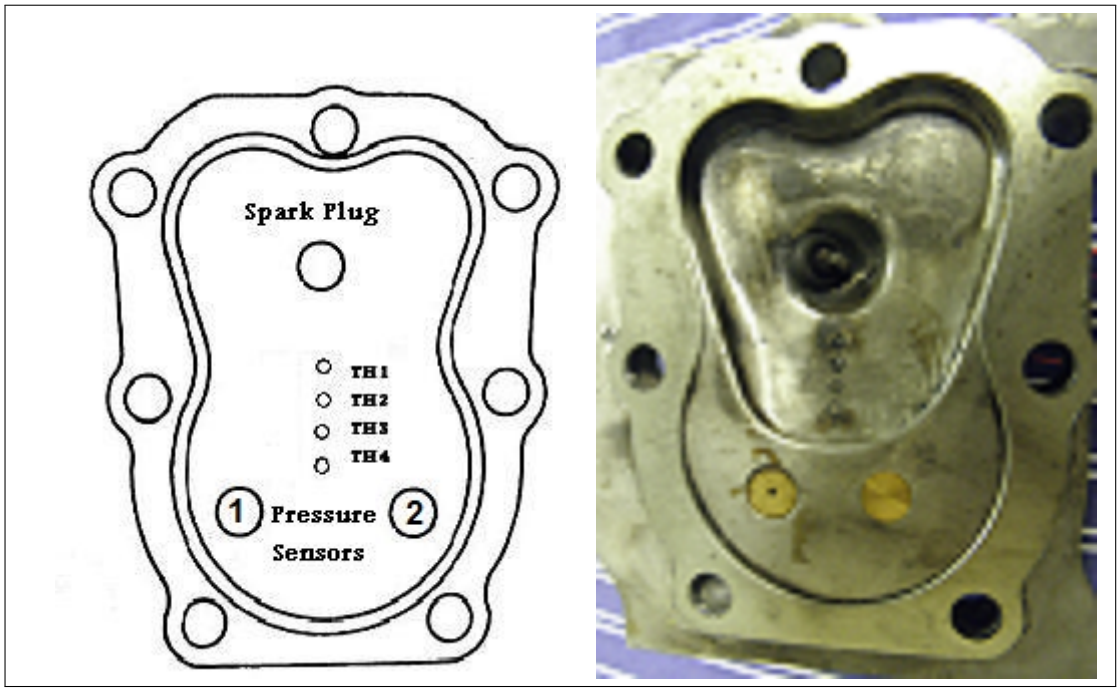

Figure 5.3: Location of heat flux probes and pressure sensors. TH1-TH4 are the thermocouple gauges, 1 and 2 refers to the PCB and Kistler piezoelectric pressure sensors respectively.

5.2.3 Pressure sensors

The piezoelectric pressure transducers are often preferred in engine applications due to their small size, quick response and accuracy. Charge is created on the quartz elements of the transducers when they are subjected to pressure. The charge produced by the pressure transducer is converted to analogue voltage values by charge amplifiers.

Two pressure sensors mounted on the head of the engine are used to measure the in-cylinder pressure. The first is an uncooled, flush-mounted Kistler 6125C piezoelectric pressure sensor which was mounted on the engine head as illustrated in figure 5.3 with a Kistler SCP slim 2852A11 charge amplifier; this pressure

sensor is used to measure the in-cylinder pressure during the motoring test. The second pressure transducer is a PCB piezoelectric pressure sensor model 112B11 with a Bruel & Kjaer charge amplifier and it is used to measure the in-cylinder pressure during the fired running engine test. The inlet pressure and the pressure in the combustion chamber near the bottom dead centre (BDC) are measured using BSDX series pressure sensors manufactured by Sensortechnics. Both of those pressure measurements will be used to provide an absolute reference for the pressure in the cylinder measured by the piezoelectric devices.

5.2.4 Top Dead Centre (TDC) encoder

A transmissive optoschmitt sensor (electro optical sensor) made by Honeywell was used to give a voltage pulse when the TDC position is reached. This sensor consists of a well aligned pair of infrared diodes facing an optoschmitt detector encased in a black thermoplastic housing, so that infrared rays emitted from the diode fall on the optoschmitt detector when uninterrupted. The photodetector consists of a photodiode, amplifier, voltage regulator, Schmitt trigger and an NPN output transistor with 10 kΩ (nominal) pull-up resistor.

The buffer logic provides a high output when the optical path is clear, and a low output when the path is interrupted. A thin metal plate with 12 notches (one every 30^o CA with a wider notch for the TDC position) was fixed to the flywheel, such that it passes through the slit between the infrared diode and the optoschmitt detector when the engine is running. The metal plate and the sensor are positioned in such a way that when the notch passes by the sensor it gives a voltage signal for each notch with a longer signal provided when the piston reaches TDC. The TDC position was calibrated by taking the voltage output readings on the oscilloscope and fixing the metal plate at the location corresponding to TDC. Voltage signals from the optical sensor are recorded by the data acquisition system. A Matlab routine is used to calculate the real crank angle data from the

voltage data.

5.2.5 Data acquisition system

The data acquisition used in the experiments is a set of two 4-Channel NI 9234 (±5 V, 51.2 kS/s per Channel, 24-Bit IEPE) modules and two NI 9205 32-Channel (±200 mV to ±10 V, 16-Bit analog input) modules from National Instruments. The data acquisition system is used to sample the measured parameters, with a sample rate 51200 samples/second. Signals recorded for the present work were: crank angle position, voltage signal from surface temperature probes, cylinder pressure, inlet air flow rate, inlet air temperature, the voltage signal from the intake pressure transducer, the voltage signal from the pressure transducer on the side of the combustion chamber near the BDC and voltage signal from the lambda sensor. The signals received recorded as time based voltage measurements were then converted to meaningful units based on previous calibration of the measuring devices. This converted data includes temperatures, pressure, engine speed and fuel flow rate. Those measurements are then combined using Matlab routines developed for this purpose to calculate performance parameters and other useful formulations to describe and characterise the engine operation and heat transfer conditions and behaviour.

5.2.6 Air flow rate and fuel flow rate

The inlet manifold of the engine is connected to a calibrated standard counter rotary flow meter made by Romet (model no. RM 30) with a maximum capacity of 30 m^3/h which which draws in air from the atmosphere. A voltage output from the air flow meter is read by the data acquisition system to provide the flow rate of air captured by the engine.

Fuel flow rate is measured on the basis of volume using a graduated beaker and

stopwatch. The fuel from the graduated beaker is sent to the engine through a pipe with a control valve. For the measurement of the fuel flow rate of the engine, the valve is open and the time for a definite quantity of the fuel flow is noted. This gives the fuel flow rate for the engine.

The air flow rate and the fuel flow rate are then converted from volume basis to mass basis via the calculated density of the ambient air and the specified density of the fuel.

5.2.7 Lambda sensor

A Professional Lambda Meter (PLM) made by MoTec is used to measure the lambda values in the engine. This sensor can measure lambda or (Air/Fuel ratio) over a wide range of mixtures with fast response time. The PLM provides a differential analogue output voltage proportional to lambda which can be connected to a data logger to record the voltage values corresponding to lambda values. The lambda sensor is located in the exhaust flow.

5.3 Data reduction procedure

The procedure and the steps that are used to convert the voltage signals the surface junction thermocouples and the pressure transducers into heat flux and pressure values are described as below. The governing equations and the simulation model which used in the model simulation are presented in appendix A.

5.3.1 Temperature and heat flux measurements and calculations

High heat fluxes like those obtained from the very harsh environment and during high speed flows such as heat flux in the internal combustion engine are generally obtained by measuring the surface temperatures. The transient heat flux registered by the thermocouples can be determined from the measured surface temperature history, by solving the one-dimensional heat conduction equation equation to convert the surface temperature history to the correct heat flux into the engine walls. The rationale for using this method for determining the heat flux is dependent on a few assumptions. The system is simplified as one-dimensional, unsteady heat conduction and the heat transfer is assumed to be normal to the combustion chamber surface, hence the probes are insulated from the engine walls. In this method the technique uses the surface temperature as a function of time to calculate the heat flux. The approach is based on the voltage changes of the fast response thermocouples, which are embedded in the engine head walls. Then those voltage changes can be converted to temperature values to be incorporated into the heat flux equation.

For this purpose a set of in-house fabricated amplifiers are used in this process, the voltage gain of those amplifiers being 2000 (1 Volt into the amplifier would give 2000 Volts out of the amplifier). The sensitivity of the E-type thermocouples used in this experiment was found to be 62.5 μV/°C based on our calibration, see appendix B. The resulting voltages come out from the amplifiers are then incorporated into a Matlab routine combining with the thermocouple sensitivity to calculate the real surface temperatures. Those temperatures are then used to calculate the heat flux through the thermocouple probes. The thermal product for this type of thermocouples can be taken as the average of the two thermocouple materials properties, although it is recommended in some cases to use the thermal properties of the chromel due to the uncertainty in constantan thermal properties [9]. The heat flux measurement is based on a one-dimensional tran-

sient conduction solution and is given as for a semi-infinite geometry. The heat flux rates can be determined from the measured surface temperature history by solving the following equation using a numerical integration technique, and based on the thermal properties of the thermocouple materials given in table 5.2.

$$q = \frac{2 \times \sqrt{\rho c_p k}}{\sqrt{\pi}} \sum_{i=1}^{n} \frac{T_i - T_{i-1}}{\sqrt{t_n - t_i} + \sqrt{t_n - t_{i-1}}} \tag{5.1}$$

Where q is the heat transfer through the thermocouple gauges, ρ, c and k are the density, specific heat at constant pressure and the thermal conductivity for the thermocouple material respectively, T is surface temperature, t is the time of interest. The above equation is valid under the assumption that for $t_0 = 0$ the temperature is set to be as $T(t_0) = 0$, i.e. the temperature in the equation given above represents the temperature difference of the thermocouple probe registered during the measurements [85] [56].

Due to the large amount of data recorded, the rapid change in temperatures and because of the nature of such measurements, some noise appears in the temperature data. Such noise associated with the temperature measurements will appear to some degree in the calculated heat flux. To minimize the noise effects, the recorded surface temperature history data will be smoothed using a smoothing function in Matlab during the calculation of the heat flux from these temperature data. The data is sampled at a rate of 51200 samples/s and smoothed over 20 points using a moving-average filter.

5.3.2 Pressure measurements

In the case of the motored test the Kistler 6125C piezoelectric pressure sensor is used to measure the in-cylinder pressure. Based on this sensor calibration, the voltage output of this sensor through the charge amplifier is converted directly to pressure data with 1 V_{out}=1 MPa pressure reading. This pressure sensor gives

directly the real pressure values in the cylinder with no need for any offset processes.

During the fired test the PCB piezoelectric pressure transducer is used to measure the in-cylinder pressure. This pressure transducer has a linear response characteristic and the slope of the calibration line is determined with a dead weight pressure tester (see appendix B). The Bruel & Kjaer charge amplifier is used to convert the charge signals from the pressure transducer to voltage signals which can be read by the data acquisition system. These voltage signals will then be incorporated into a Matlab routine to be transformed into pressure values using the following formula for this pressure transducer according to the sensor calibration.

$$P = C_1 V + C_2 \tag{5.2}$$

Where P is the pressure, C_1 is calibration constant (the slope of the curve), V is the voltage readings in volts and C_2 is the intercept of the curve on the pressure axis. A Matlab routine will be used to calculate the in-cylinder pressure values versus the crack angle data. The pressure value obtained by the in-cylinder pressure transducer does not give the actual in-cylinder pressure values. In order to obtain the actual in-cylinder pressure values, the calculation procedure needs a reference or pegging pressure. The reference pressure is determined by reading the intake pressure and the pressure in the cylinder at near the BDC, using the transducer embedded on the side of the combustion chamber at this position as described below.

The in-cylinder pressure values acquired from the PCB piezoelectric pressure transducer mounted on the head of the engine must be offset to match a known absolute pressure. The BSDX series pressure sensors offer cost-effective absolute, differential and gage pressure measurements. The reference pressure values from the two BSDX series pressure sensors (mentioned in section 4.2.3) will be assigned as the actual in-cylinder pressure when the piston is at BDC of the intake

stroke. For this purpose a BSDX5000A2R from the BSDX series pressure sensors is installed on the side wall of the combustion chamber near the bottom dead centre. In this case time averaged pressure readings from the combustion chamber at around the bottom dead centre are recorded. This recorded pressure is matched to the inlet pressure recorded in the intake stroke downstream of the throttle, using a BSDX1000A2R pressure sensor from the BSDX series pressure sensors. The offset of these two measurements is used to offset the rest of the in-cylinder pressure data. Based on the previous offset procedure, all other pressure values in the engine cycle can be determined from the knowledge of the reference pressure values and the calibration line slope of the pressure transducer in the engine head.

The in-cylinder pressure data collected in this stage will be averaged over a number of cycles along with the crank angle, to minimize the cycle-to-cycle variation and to obtain a good representation of the engine operating conditions.

Chapter 6

Results from Engine Experiments and Assessment of Quasi-Steady Models

6.1 Introduction

Measurements are taken under motored and fired conditions with the engine described in chapter 5 to obtain a new data set in which all parameters necessary for heat flux simulation are measured. The experimental results for the pressure and heat flux obtained from the motored and fired tests together with the results from the simulation process using some of the existing quasi-steady heat transfer models, are presented in this chapter.

6.2 Results from motored engine

The throttle in the intake is used to control the mass of air entering the engine. The effect on the heat transfer of reducing the in-cylinder mass is investigated. The throttle position is varied from a wide open throttle (WOT) to a fully closed throttle (FCT). In this work the pressure data are analysed to ascertain a proper phasing of the pressure data along with the crank angle data, and also to provide the peak pressure values during the engine test in order to compare them with simulated results.

6.2.1 Results from wide open throttle test

The initial air temperature was calculated from the known trapped mass and the measured pressure and was found to be 314.98 K, the inlet pressure measured being 80.79 kPa. The mass of the air captured by the engine was found to be 2.2339×10^{-4} kg/cyc. The engine was run at 1411 rpm. The in-cylinder pressure data obtained from this test is presented in figure 6.1. Those pressure data show a little cycle-to-cycle variation but they can provide considerable information about the reliability and accuracy of the measurement procedure.

The in-cylinder pressure data is then ensemble averaged, and presented verses crank angle data along with the simulated pressure data. The ensemble averaged pressure data verses the crank angle is shown figure 6.2. This figure indicates that the occurrence of the peak pressure occurs slightly before the top dead centre (about 1.6 degrees crank angle BTDC).

In order to reliably simulate the heat transfer process within the engine cylinder, it is necessary to match the simulated pressure with the experimentally measured pressure. The heat transfer model proposed by Eichelberg [12] equation (2.6) is used in this case to simulate the pressure data and later to simulate the heat flux

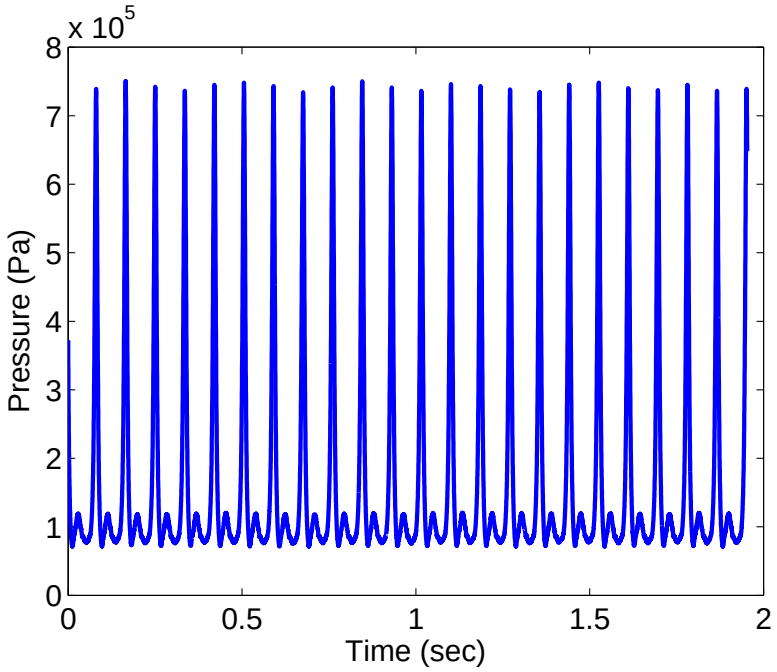

Figure 6.1: In-cylinder pressure for WOT motored test over 23 cycles.

within the engine. The pressure simulation using this model shows a reasonable agreement with the measured pressure, figure 6.3 which gives a good opportunity to reliably simulate the instantaneous heat flux in later work. The peak pressure value goes up to about 0.74 MPa at 1.6° crank angle BTDC and then starts to decrease. At approximately 180° CA after top dead centre, the pressure starts to rise as the piston moves towards top dead centre during the exhaust stroke.

The heat transfer coefficient proposed by Eichelberg was used to predict the total instantaneous heat transfer with no radiation term included. This formula is widely used in predicting the heat transfer in low-speed engines [12]. In the present case, a scaling factor (α_s) is applied to this formula to allow matching of the measured and simulated pressure. Eichelberg's formula with a scaling factor can be presented as follows.

$$h = \alpha_s 7.67 \times 10^{-3} (C_m)^{1/3} (PT_g)^{1/2} \tag{6.1}$$

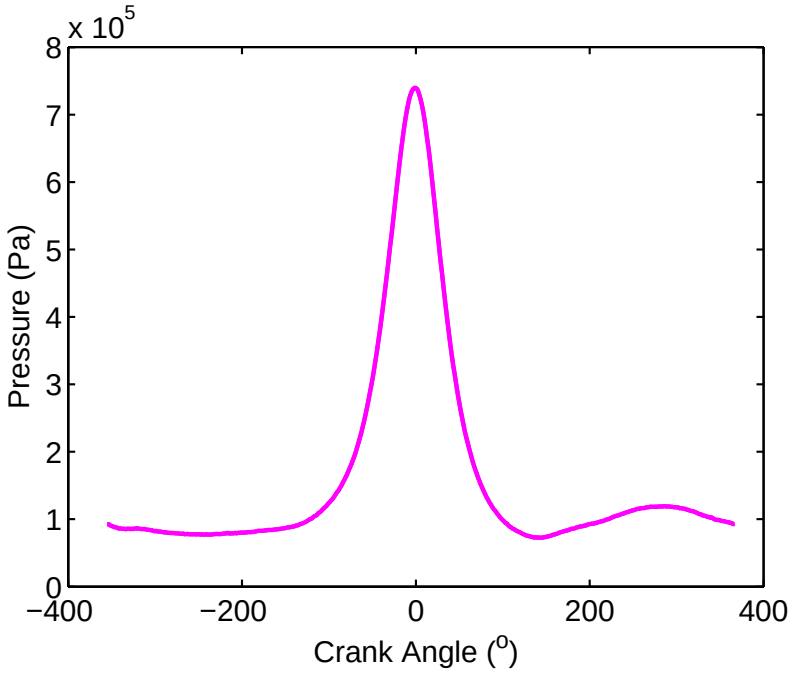

Figure 6.2: Averaged in-cylinder pressure for WOT motored case.

In this formula the scaling factor is tuned until a reasonable agreement between the measured and simulated pressure is achieved. In the case of the wide open throttle test the scaling factor is found to be 4.035. Once the reasonable agreement between the two pressure histories is achieved, the instantaneous heat flux in the combustion chamber is investigated and simulated.

The change in the measured surface temperature history from one of the coaxial thermocouples is shown in figure 6.4. The heat flux extracted from one of the measured surface temperatures from one of the thermocouple probes is presented in figure 6.5. The peak heat flux value for this motored test reaches the value of more than 80 kW/m^2 in some cycles. Notably the peak heat flux level varies significantly from cycle-to-cycle, whereas the minimum level is about the same for all cycles.

Figure 6.6 shows the variation in the ensemble averaged heat flux with crank angle at the three measurement positions. Position one is where the closest probe to the spark plug is located, followed by position two and three, figure 5.3 in

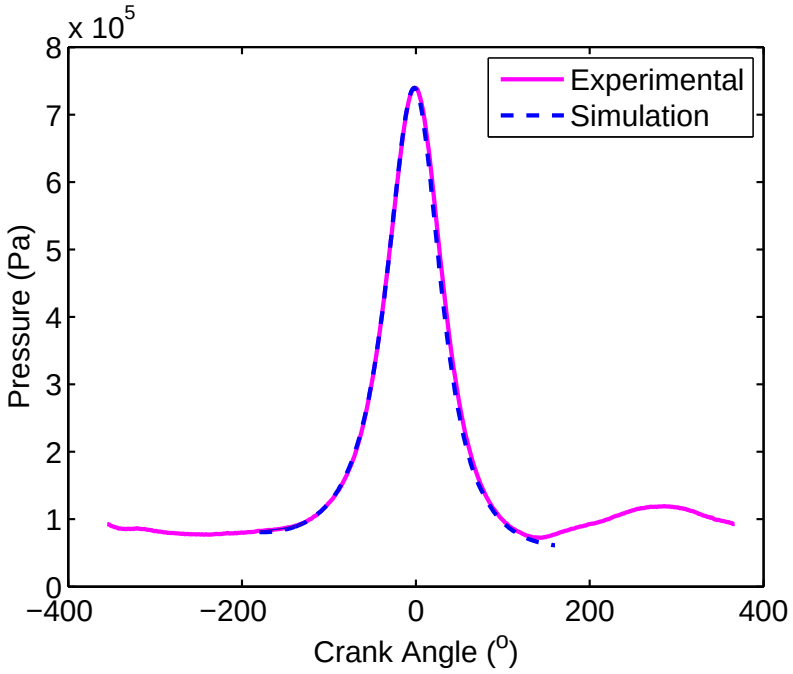

Figure 6.3: Averaged in-cylinder measured pressure and the simulated pressure for WOT motored case.

chapter 5. The present surface junction thermocouples do not have an in-depth thermocouple reference, so the small steady-state component of heat flux, remains unresolved. Therefore, the ensemble averaged heat flux was offset to match the minimum values of the simulated heat flux. It can be seen that there is a variation in the heat flux according to the measuring position during the intake stroke, due to the differences in the local air flow. It can also be noticed that the increase in the heat flux during the compression stroke occurs simultaneously at all locations. The heat flux measured at location one seems to rise more rapidly, followed by heat flux at location three and two respectively, whereas the heat flux at location two falls more rapidly than the heat flux at location three and one after top dead centre. On the other hand, the peak values of heat flux at locations two and three seem to occur approximately at the same crank angle, whereas, at location one the peak heat flux value occurs later at about 1.7° CA after top dead centre. Differences in the heat flux during the exhaust stroke can be noticed and this might be because of the exhaust valve opening and the change in the air

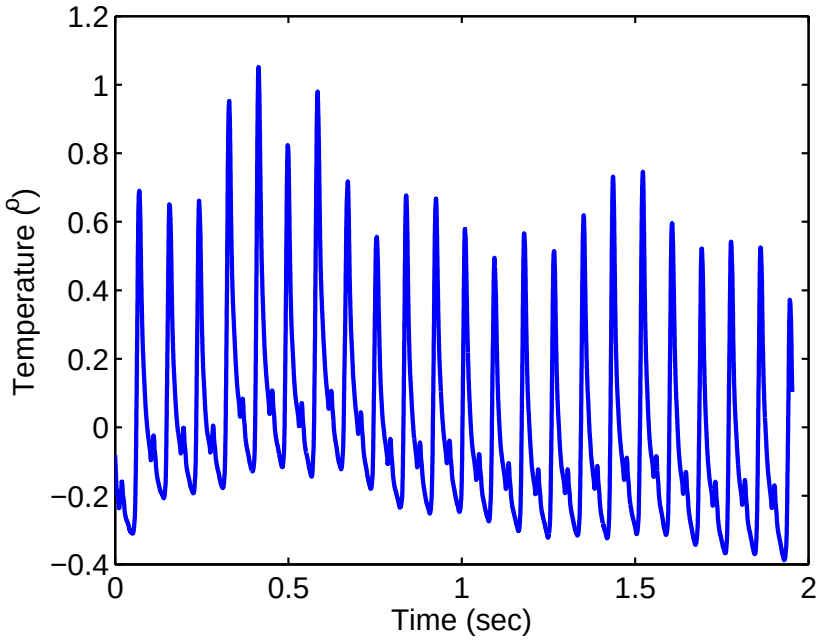

Figure 6.4: Change in surface temperature from probe one for WOT motored case.

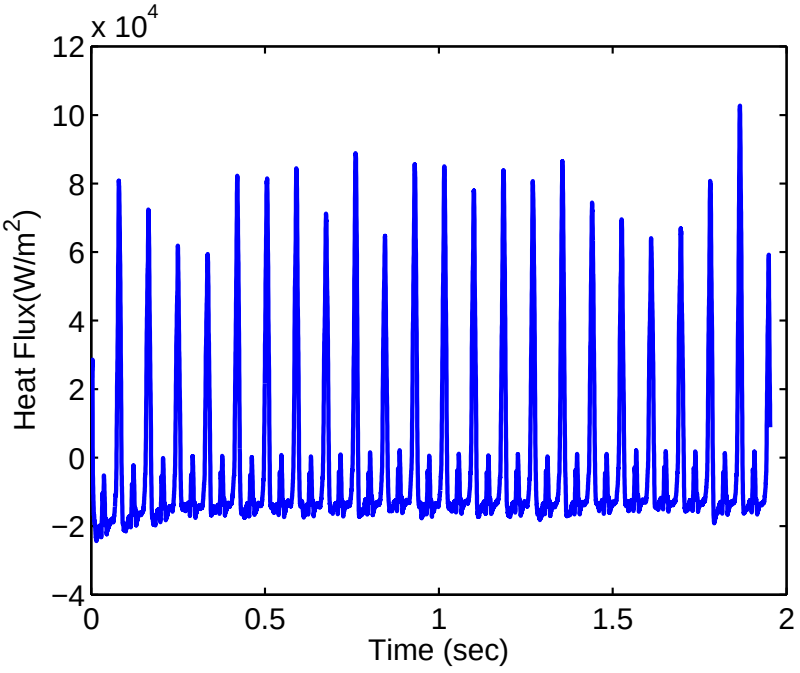

Figure 6.5: Heat flux calculated from measured surface temperature from probe one for WOT motored case.

flow pattern.

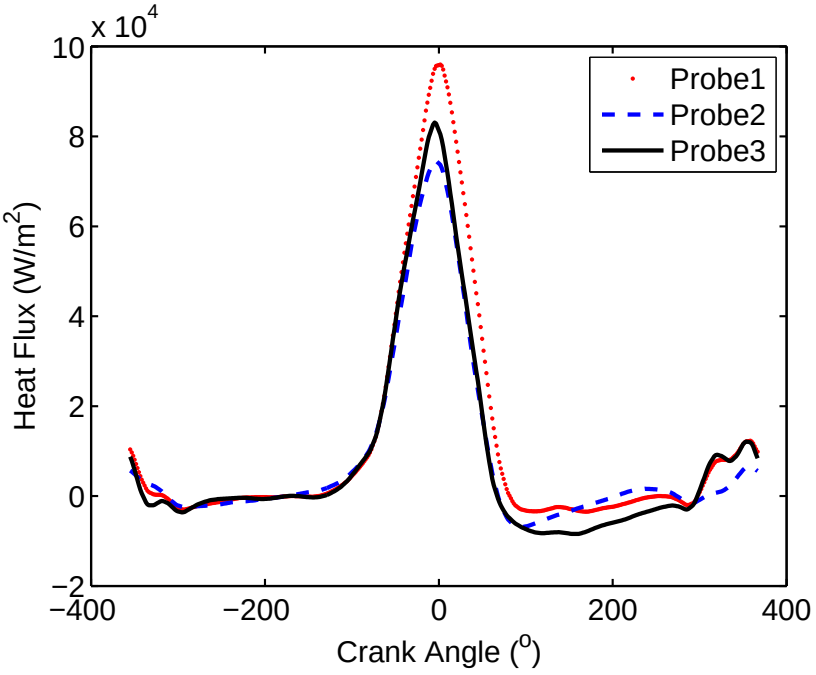

Figure 6.6: Heat flux from different measuring locations for WOT motored case.

The heat flux is ensemble averaged for the three probes and plotted versus crank angle, figure 6.7. A closer look at the heat flux data in this figure shows that the averaged peak heat flux value occurs before the top dead centre (about 3.25° CA BTDC). The decline of the heat flux from about 8.25 kW/m^2 occurs at 330° CA BTDC, due to the inlet valve opening which draws in air at ambient temperature. This decline in the heat flux continues as the gas in the cylinder is cooled by the fresh air entering the cylinder. The ensemble averaged peak heat flux value becomes about 84.4 kW/m^2. A sharp decline in the heat flux occurs near the top dead centre and negative values of heat flux are reached at about 100° CA after top dead centre then it starts to increase as the piston moves towards the top dead centre during the exhaust stroke.

The measured heat flux and the simulated heat flux is presented in figure 6.8, along with the crank angle. The simulation of the heat flux using the scaled Eichelberg's model with a scaling factor of 4.035 (chosen so pressure histories

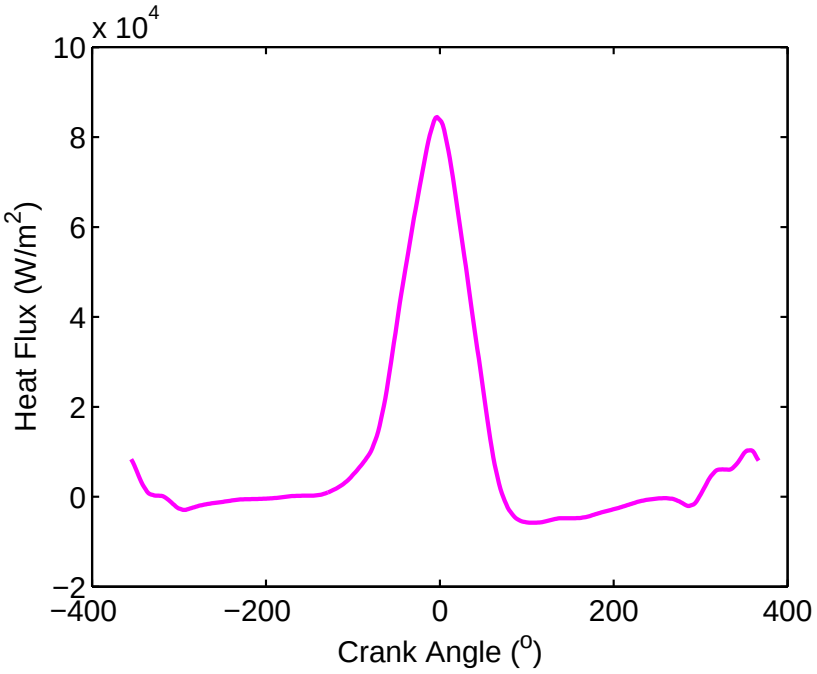

Figure 6.7: Averaged heat flux for WOT motored case.

match) overestimates the measured one by a factor of more than 1.9. This might be due to the fact that most of the existing heat transfer models are generally engine-specific, and heat transfer characteristics are generally considered to be different from engine to engine. A significant feature can be noticed from this figure, that the simulated heat flux appears to rise and fall more rapidly than the measured one. The peak simulated heat flux value occurs at 5° CA BTDC which is earlier than the peak value of the measured heat flux. Using an unscaled version of Eichelberg's model shows no improvement in the prediction of the heat flux when compared to the scaled one.

Some of the widely used heat transfer models are used to make a comparison between the heat transfer models and the measured data. Predicted results of the heat flux using a selection of the previous models as described in chapter 2 are presented in figure 6.9. All of the heat transfer models used in this comparison overestimate the heat flux. These previous models are all tuned so that the simulated pressure in each case matched the measured pressure. In Woschni's model (equa-

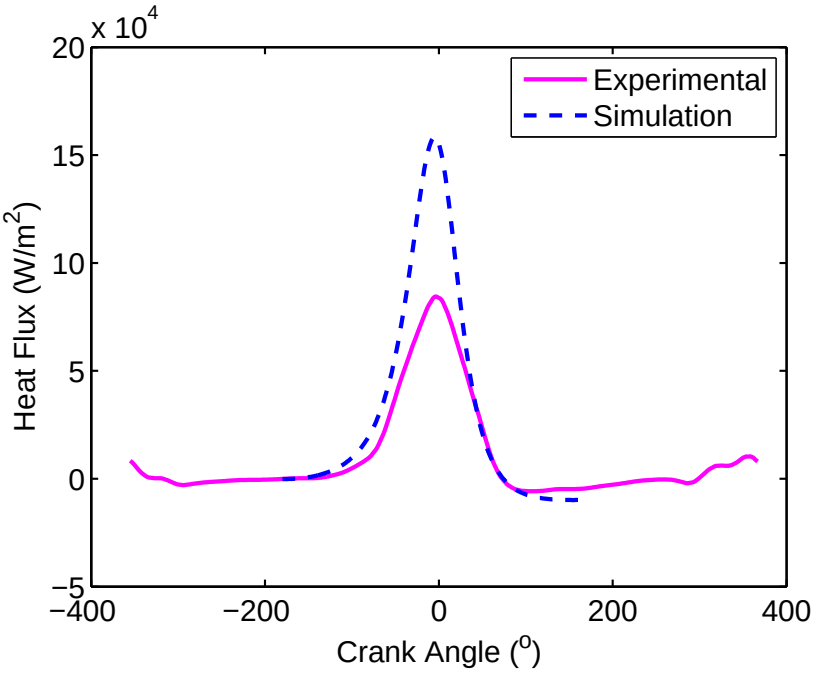

Figure 6.8: Measured and simulated heat flux using Eichelberg's model with a scaling factor of 4.035 for WOT motored case. Experimental data from the averaged heat flux for the three probes.

tion 2.8) the scaling factor is chosen to be 5.296, in Annand's model (equation 2.7) the scaling factor is 1.939, in Nusselt's model (the convection term only equation 2.4) the scaling factor is found to be 6.036 and in Hohenberg's model (equation 2.10) the scaling factor used is 3.108.

Figure 6.10 shows a zoomed-in plotting of the peak values for those models. The figure illustrates that even when these models are tuned to match the measured peak motoring pressure, the difference in the peak heat flux values between the different heat transfer models is in the order of about 13 %. The figure also shows that the models proposed by Hohenberg and Nusselt provided the highest heat flux, followed by the models of Woschni, Eichelberg and finally, Annand.

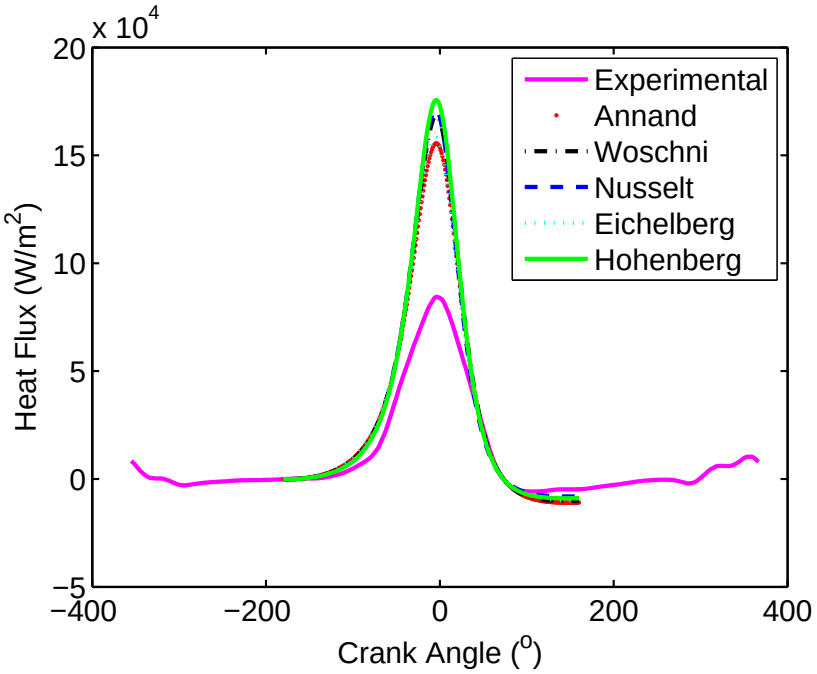

Figure 6.9: Comparison of measured and simulated heat flux using previous heat transfer models with different scaling factors for WOT motored case. Experimental data from the averaged heat flux for the three probes.

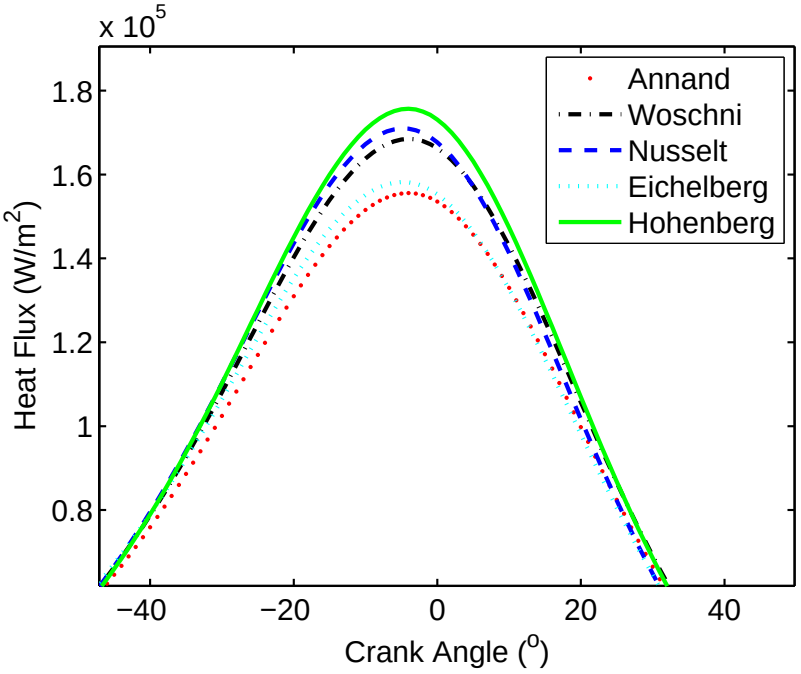

Figure 6.10: Zoomed-in plotting for simulated heat flux using previous heat transfer models for WOT motored case.

6.2.2 Results from fully closed throttle test

In this test the engine was throttled, which decreases the trapped mass. This decreases the in-cylinder pressure, and a decrease in the heat flux would be expected as well. The initial temperature of the air based on the trapped mass and the measured pressure was found to be 408.48 K and the inlet pressure was 42.55 kPa. The trapped mass was dropped due to the throttling process, and it was found to be 9.0711×10^{-5} kg/cyc and the engine was run at 1406 rpm. The measured in-cylinder pressure obtained from this test is shown in figure 6.11.

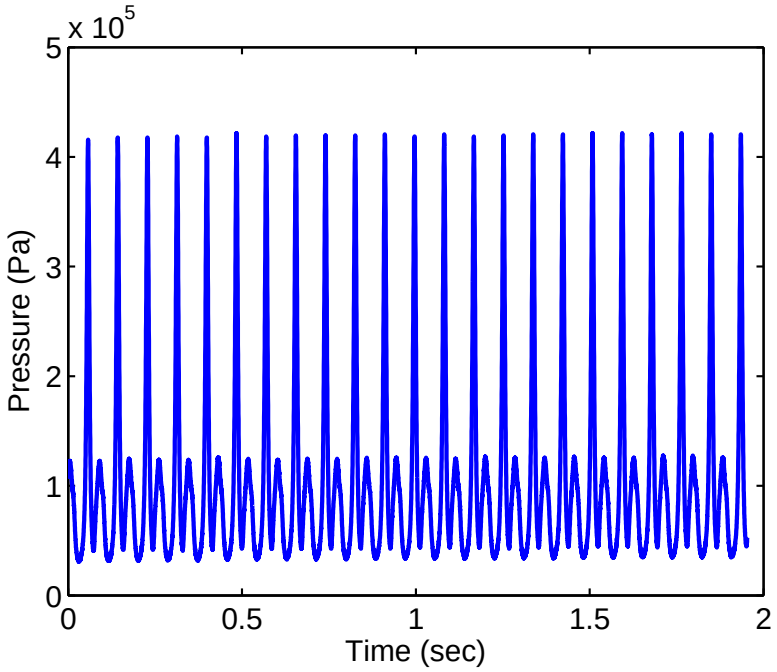

Figure 6.11: In-cylinder pressure from FCT motored test over 23 cycles.

Figure 6.12 shows the ensemble averaged in-cylinder pressure versus crank angle. The figure shows that the peak measured pressure value occurs at 1.6° CA before top dead centre. The simulated pressure is then plotted, along with the measured pressure, figure 6.13. This figure demonstrates that the simulated peak value occurs slightly later than the measured one at the top dead centre. The figure also shows that a good agreement between the measured and the simulated pressure is achieved. The peak pressure value is about 0.42 MPa and

then it starts to decline after the top dead centre and to start to rise again at about 180° CA ATDC as the piston moves towards top dead centre during the exhaust stroke. Eichelberg's heat transfer model (equation 2.6) is used in this case to simulate the pressure and the heat flux. The scaling factor (α_s) that has been applied in the WOT case to match the measured and the simulated pressure, is applied in this case as well and is found to be 0.208.

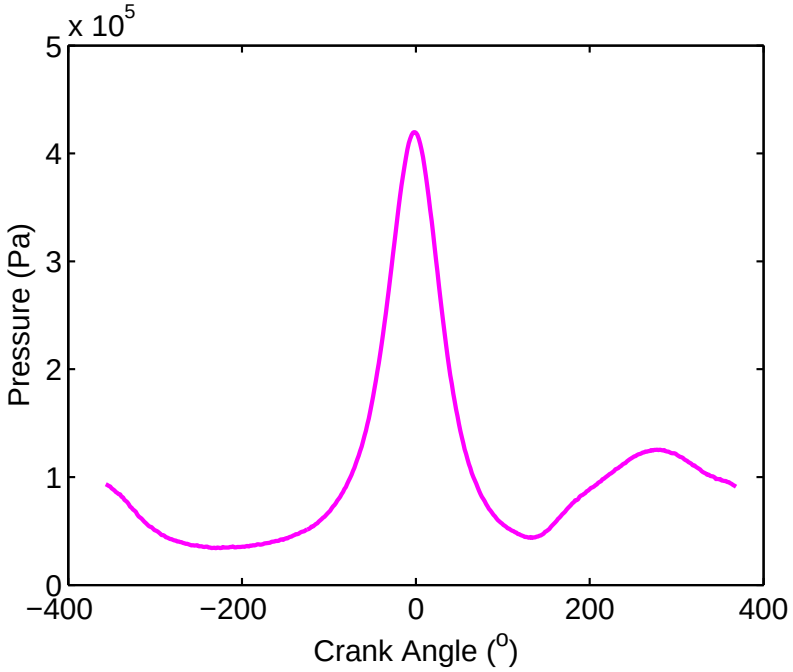

Figure 6.12: Averaged in-cylinder pressure from FCT motored test.

Based on the good agreement achieved between the measured and the simulated pressure, the instantaneous heat flux is then investigated. The change in the engine surface temperature and heat flux from the gases to the cylinder walls are presented in figures 6.14 and 6.15 respectively for one of the measuring positions. Figure 6.15 shows that the heat flux reaches more than 60 kW/m^2 in some cycles and it also shows a difference in the peaks from cycle-to-cycle.

The variation of the ensemble averaged heat flux from the three measuring positions is presented in figure 6.16. The ensemble averaged heat flux was also offset in the this case to match the minimum values of the simulated heat flux, since

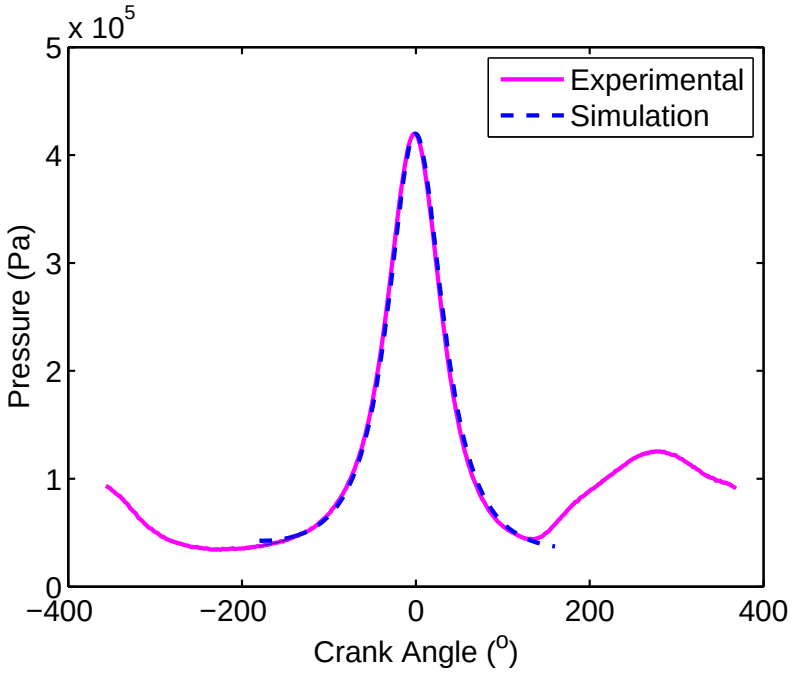

Figure 6.13: Averaged in-cylinder measured pressure and the simulated pressure for FCT motored case.

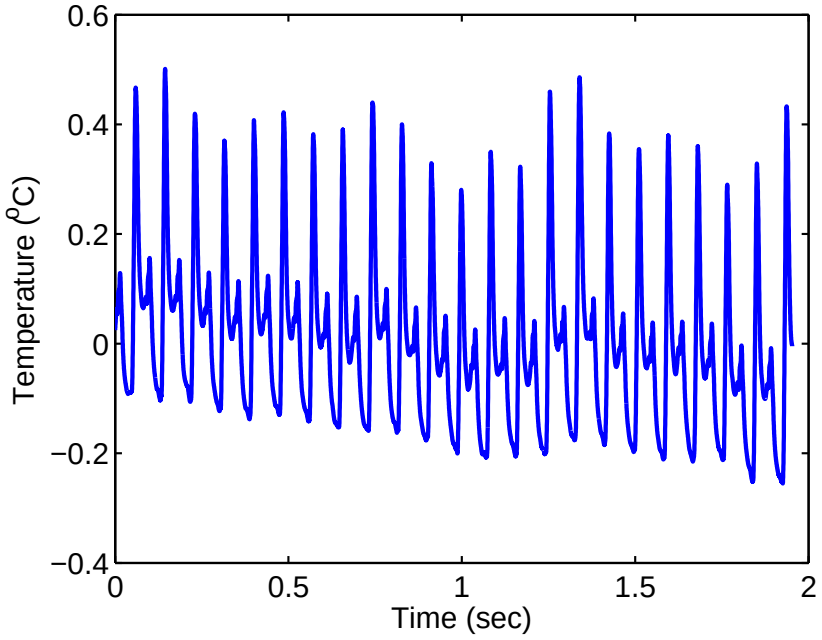

Figure 6.14: Change in surface temperature from probe one for FCT motored case.

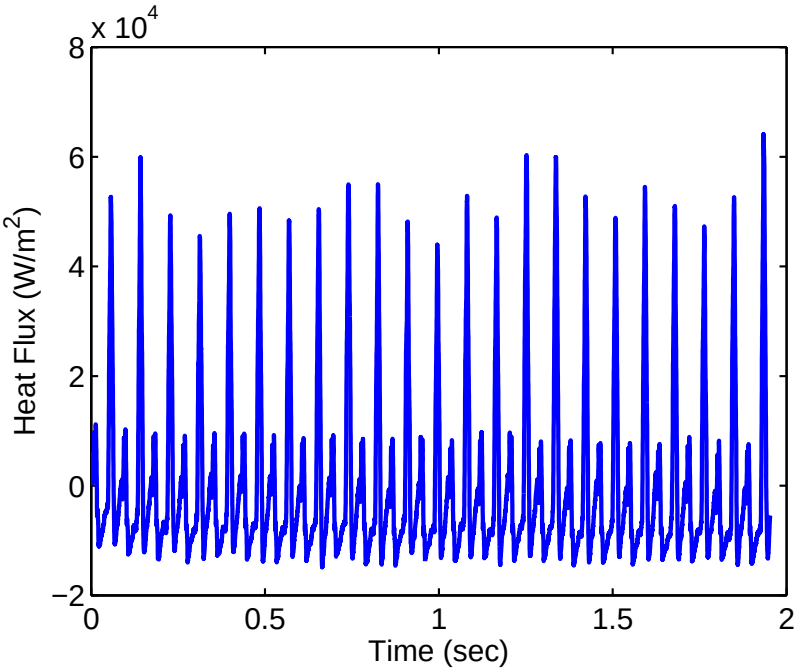

Figure 6.15: Heat flux calculated from measured surface temperature from probe one for FCT motored case.

the small steady-state component of the measured heat flux remains unresolved in the experimental data. The figure illustrates that the heat flux at position one decreases earlier, as it is the closest one to the intake valve and the incoming fresh air reaches it first. The same trend found in the WOT case can be noticed here, when the heat flux measured at location one rises more rapidly than the heat flux at location three and two respectively. However, the heat flux at location two falls more rapidly than the heat flux at location three and one. The peak values of the heat flux measured at location one and two occurs at the same crank angle (3.2° CA BTDC), whereas at location three, it happens earlier at about 4.9° CA before top dead centre.

Figure 6.17 presents the ensemble averaged heat flux from the three measuring positions. As the fresh air enters the engine during the intake stroke, the heat flux decreases from 11.5 kW/m^2 and continues to decrease below zero to reach its minimum value at about 294° before it starts to rise again. The peak value of the

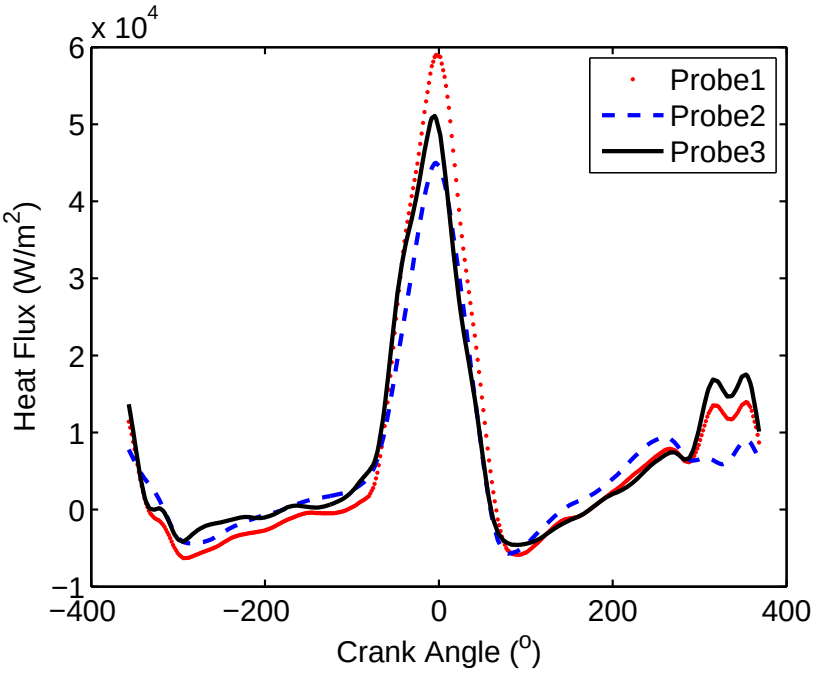

Figure 6.16: Heat flux from different measuring locations for FCT motored case.

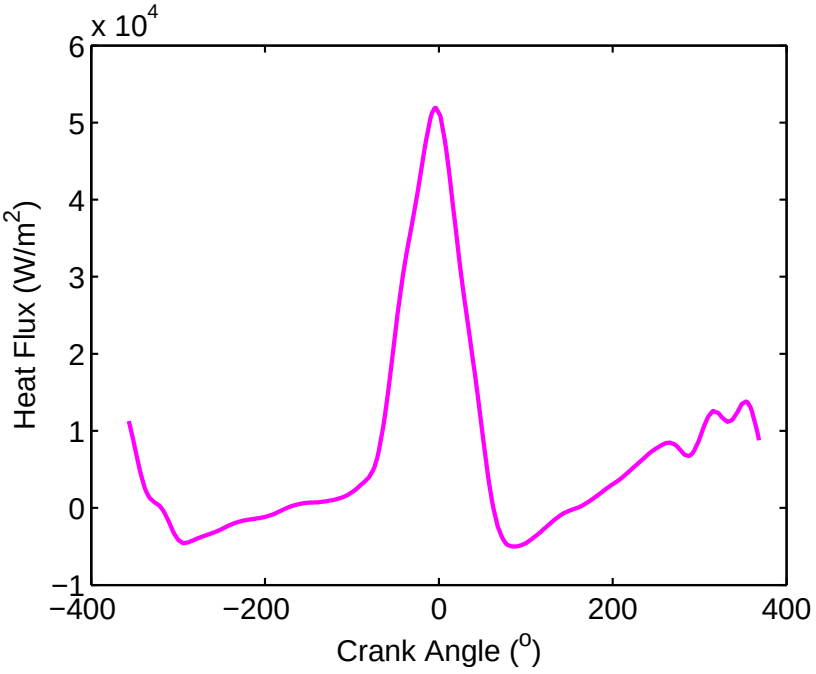

Figure 6.17: Averaged heat flux for FCT motored case.

ensemble averaged heat flux is 52.11 kW/m^2 and it occurs at 3.2° CA BTDC. The heat flux then declines sharply to reach its minimum value after top dead centre

at about 85° CA. As the piston moves towards the top dead centre, the heat flux starts to increase during the exhaust stroke. The simulated heat flux using Eichelberg's model is presented in figure 6.18 along with the measured heat flux versus crank angle. The figure shows that no agreement is achieved between the measured and the simulated heat flux. Moreover, the peak value of the measured heat flux is higher than the simulated one by more than 4.7 times. The figure also demonstrates that the peak simulated heat flux value occurs later than the measured one at about one degree before top dead center. Using the unscaled Eichelberg's model in the FCT case shows better agreement with the measured one than the scaled model, but the measured pressure history is not accurately simulated.

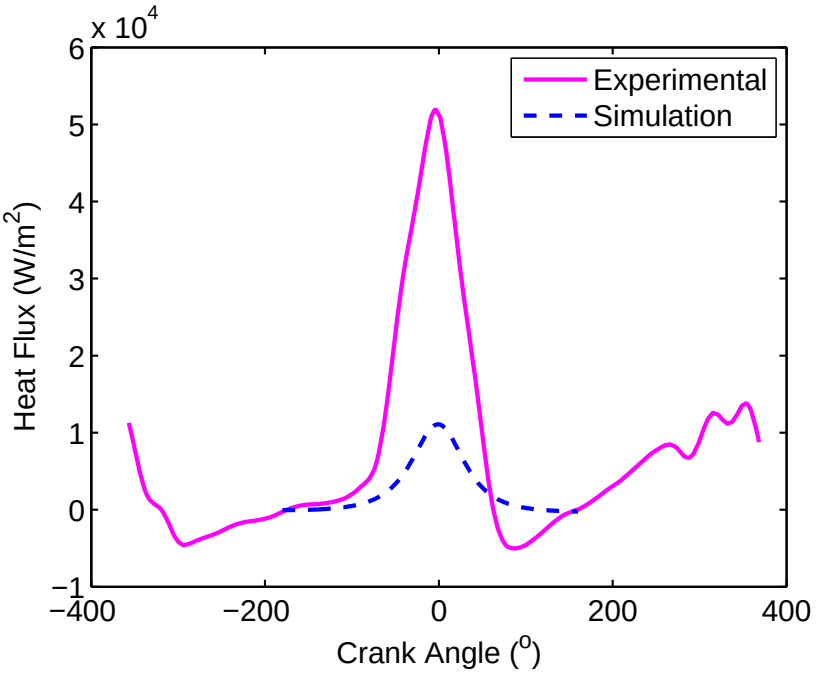

Figure 6.18: Measured and simulated heat flux using Eichelberg's model with a scaling factor of 0.208 for FCT motored case. Experimental data from the averaged heat flux for the three probes.

A comparison between the measured heat flux and the simulated heat flux using some of the previous heat transfer models with different scaling factors is presented in figure 6.19. The figure shows that all of the heat flux models under-

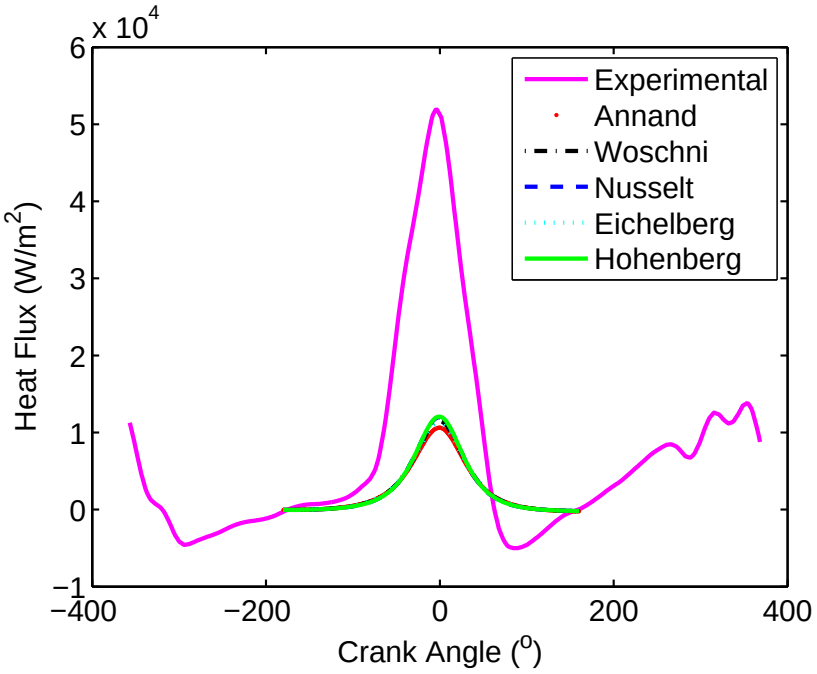

Figure 6.19: Comparison of measured and simulated heat flux using previous heat transfer models with different scaling factors for FCT motored case. Experimental data from the averaged heat flux for the three probes.

estimate the measured heat flux. The same procedure in matching the measured and the simulated pressure is followed in the FCT case and different scaling factors are applied to each model. In Woschni's model (equation 2.8) the scaling factor applied is 0.444, in Annand's model (equation 2.7) the scaling factor is found to be 0.148, in Nusselt's model (the convection term only equation 2.4) the scaling factor is chosen as 0.362 and in Hohenberg's model (equation 2.10) the scaling factor used is 0.251. A zoomed-in plotting for the heat flux predicted by the previous heat transfer models is shown in figure 6.20. This figure determines that the difference in the peaks between the different models is 13 %, which is the same as that found in the WOT case. The figure also demonstrates that the highest value of heat flux is predicted by the scaled Hohenberg's and Nusselt's models.

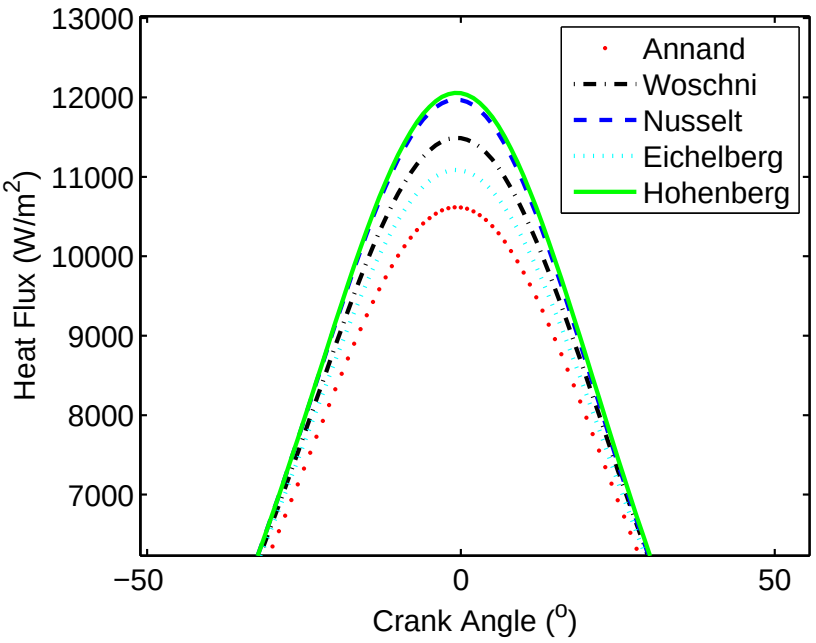

Figure 6.20: Zoomed-in plotting for simulated heat flux using previous heat transfer models for FCT motored case.

6.3 Results from fired engine

This section discusses the results obtained from the fired engine test. The inlet air temperature was found to be 400 K, based on the trapped mass and the measured inlet pressure, the inlet pressure measured at the inlet manifold was 54 KPa. The averaged wall temperature was found to be as 432.15 K based on the measured data. The mass of the air entering the engine was found to be 1.1778×10^{-4} kg/cyc. The engine was run at 2213 rpm. The engine was loaded and it was run at a slightly lean operating condition with an equivalence ratio of 0.95.

The in-cylinder pressure data obtained from this test is presented in figure 6.21. The figure shows the peak pressure distribution of a sample of about 35 consecutive cycles. This figure shows the maximum and minimum pressure during the sample, as well as the variation in the pressure peaks, with some cycle-to-cycle variation

and almost the same minimum values.

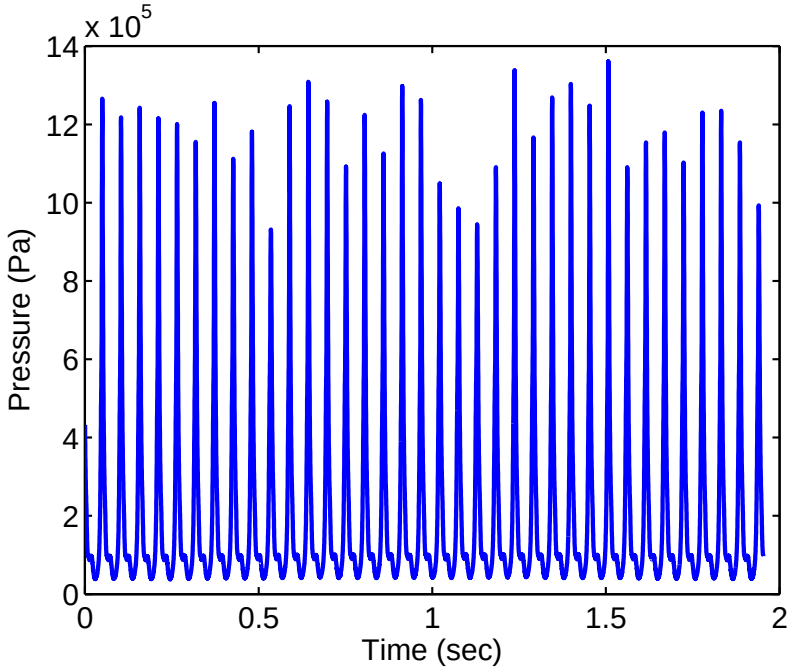

Figure 6.21: In-cylinder pressure for fired case over 35 cycles.

The ensemble averaged in-cylinder pressure and simulated pressure are presented in figure 6.22. This figure demonstrates that some agreement between the simulated and measured pressure has been achieved during the compression and combustion stages. To achieve this level of agreement, some parameters in the simulation had to be tuned. In the simulation of the fired engine test, the scaling factor applied to Eichelberg's model in equation 2.6 has also been applied to Woschni's model (equation 2.8) in the case of the fired test. The scaling factor in this case is found to be 0.15. Moreover, the Wiebe function model is used in the definition of the mass fraction burned and the Wiebe parameters have been tuned as well to match the pressure and were found to be $a = 75$ and $m = 2.036$. The peak pressure value is about 1.14 MPa and it occurs at about 30° CA ATDC. Then the pressure starts to decrease during the expansion stroke and it can be noticed that the simulated pressure seems to decline more rapidly than the measured one until about 100° CA after top dead centre when the measured pressure started to drop more rapidly.

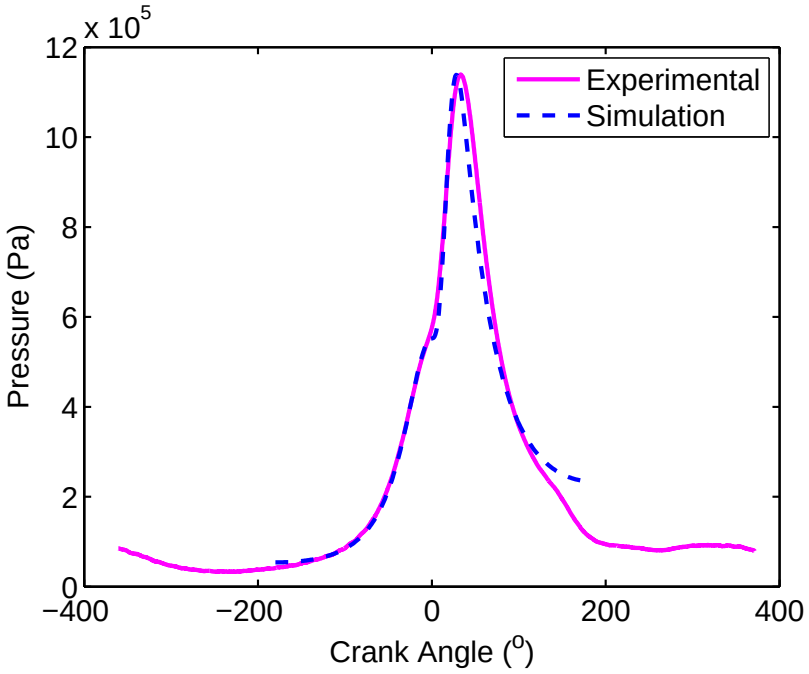

Figure 6.22: Averaged in-cylinder measured pressure and the simulated pressure for fired case.

The change in the engine surface temperature and heat flux from the gases to the combustion chamber walls from one of the thermocouples are shown in figure 6.23 and figure 6.24 respectively. Figure 6.24 shows that a great cyclic variation occurring in the heat flux appears in the peaks, whereas the minimum values for most of the cycles are almost the same.

Figure 6.25 displays the heat flux trace at the three measurement positions on the engine head, the offsetting was also applied to this case to match the minimum values of the measured heat flux with the simulated one. It can be seen that there is a slight difference in the heat flux in the intake stage according to the measuring position, due to the local gas velocities and flows. The figure also demonstrates that, during the compression stage and just before the flame initiation when the piston moves towards the TDC, the gas density through the cylinder increases and accordingly the heat flux increases in all measuring locations, and the local distribution of the heat flux is only affected by the local velocity distribution in

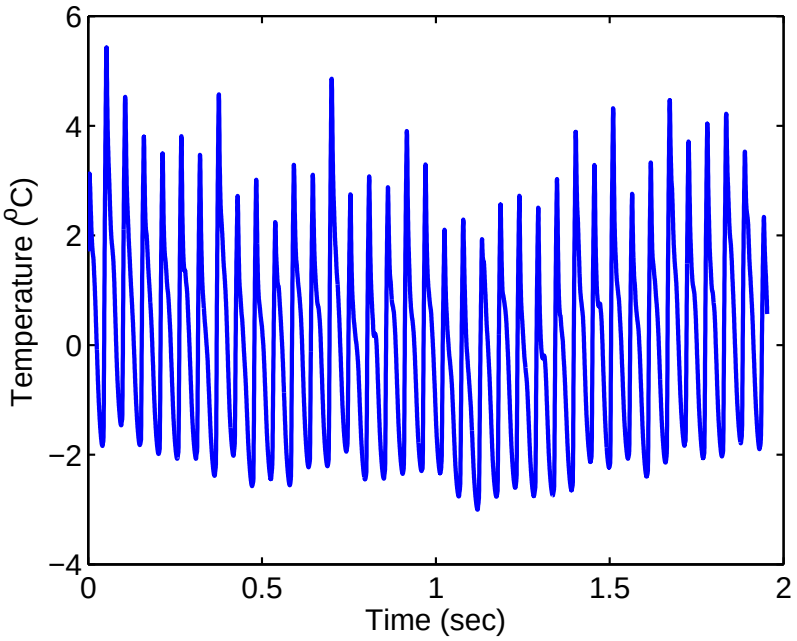

Figure 6.23: Change in surface temperature from probe one for fired case.

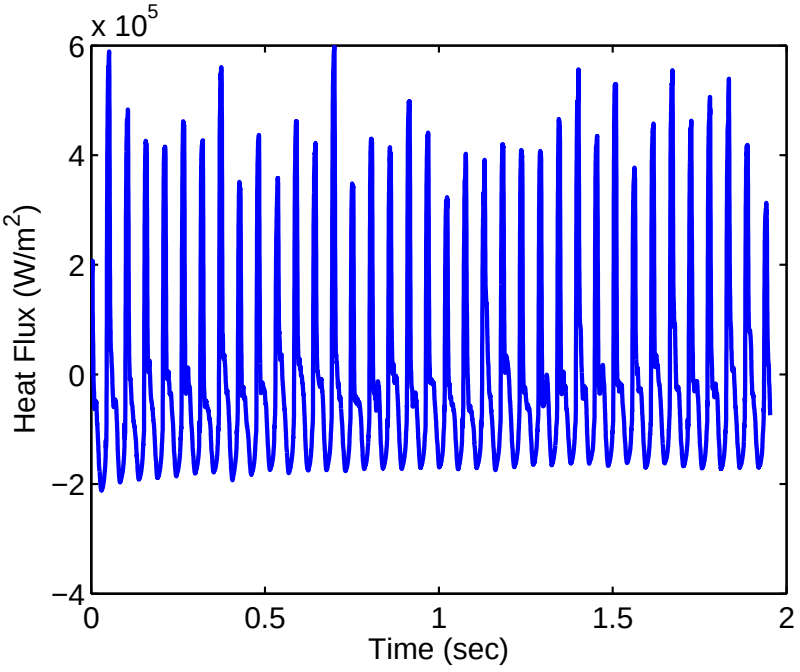

Figure 6.24: Heat flux calculated from surface temperature from probe one for fired case.

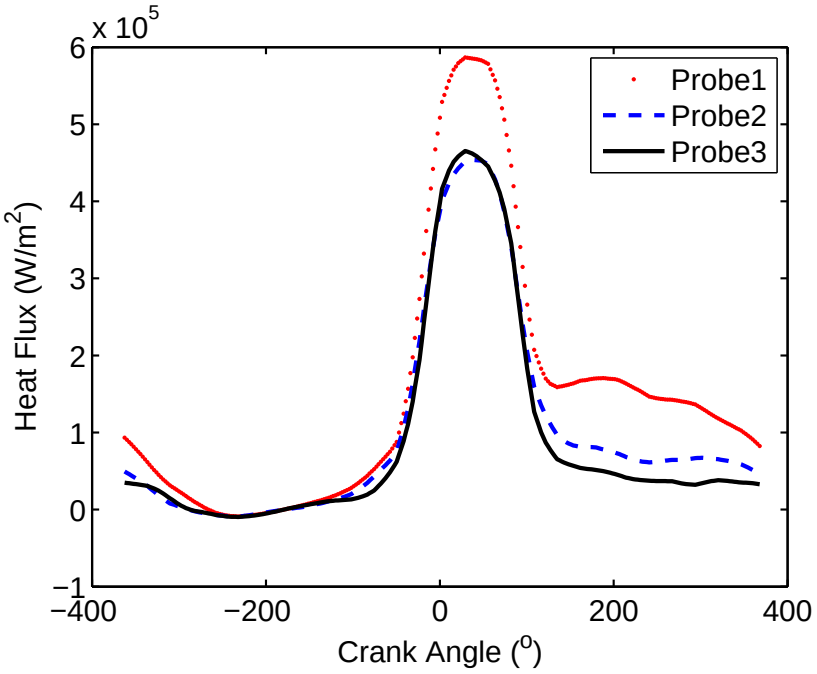

Figure 6.25: Heat flux from different measuring locations for fired case.

the cylinder. After the ignition it can be noticed that the heat flux at location one starts to rise more rapidly and it has the highest peak value, due to its location closest to the spark plug, followed by location two and ultimately location three. The figure also illustrates that the peak values for the measuring locations one and three occur at the same crank angle (about 30° CA ATDC). At location two, it occurs later, at 37° CA after top dead centre.

When the numerical prediction of the pressure matches the experimental pressure data as closely as possible, then the numerical heat flux data can be compared to the measured heat flux. The ensemble averaged measured heat flux over the three measuring locations is presented in figure 6.26, with simulated heat flux using the scaled Woschni's model. This figure demonstrates that the peak measured heat flux occurs at the same crank angle of peak in-cylinder pressure and it is about 498 kW/m^2. After that the heat flux reduces to relatively low values as the piston moves towards the bottom dead centre and the expansion starts to cool the in-cylinder burned gases. It can be noticed from this figure that the

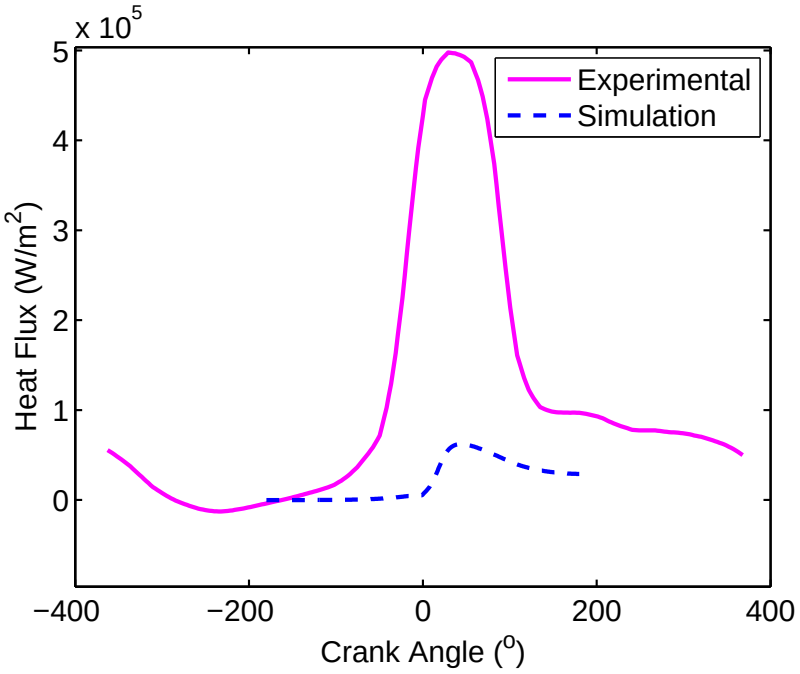

Figure 6.26: Measured and simulated heat flux using Woschni's model with a scaling factor of 0.15 for fired case. Experimental data from the averaged heat flux for the three probes.

simulated heat flux using the scaled Woschni's model is obviously underestimating the measured heat flux. The measured peak value is higher than the simulated one by more than 7.6 times. It is possible that due to the fact that those models are engine-specific, they might not be able to predict the heat flux correctly over a different range of engine geometries and they cannot be widely used for all operating conditions. The unscaled Woschni's model in the fired case shows better agreement with the measured one than the scaled Woschni's model, but the measured pressure history is found to be not accurately simulated if the unscaled model is used.

In contrast to some of the well known heat transfer models with different scaling factors, the measured heat flux is plotted against those models in order to investigate their ability to predict the heat flux in this engine. The scaling factors used in this simulation are 0.08 for Annand's model (equation 2.7) and Eichelberg's model (equation 2.6), 0.1 for Nusselt's model (the convection term only equa-

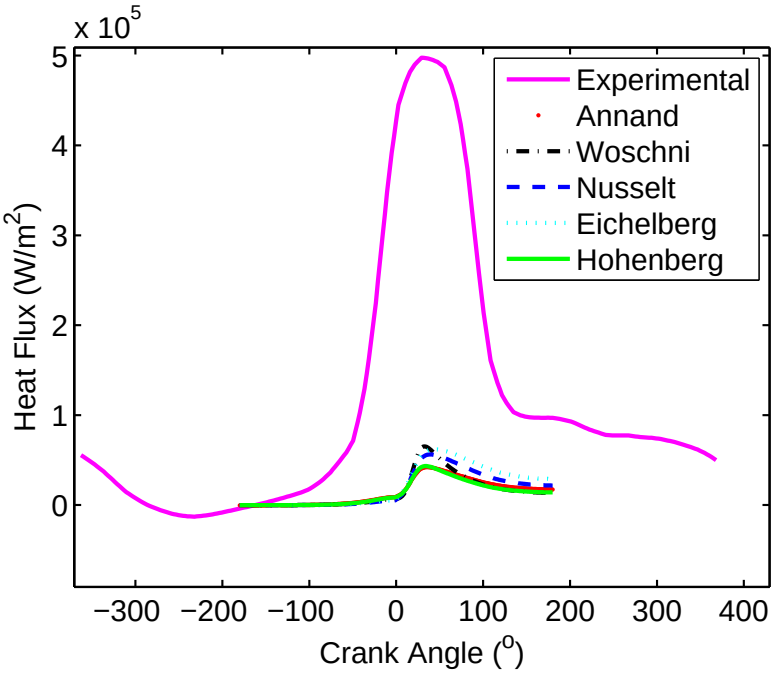

Figure 6.27: Comparison of measured and simulated heat flux using previous heat transfer models with different scaling factors for fired case. Experimental data from the averaged heat flux for the three probes.

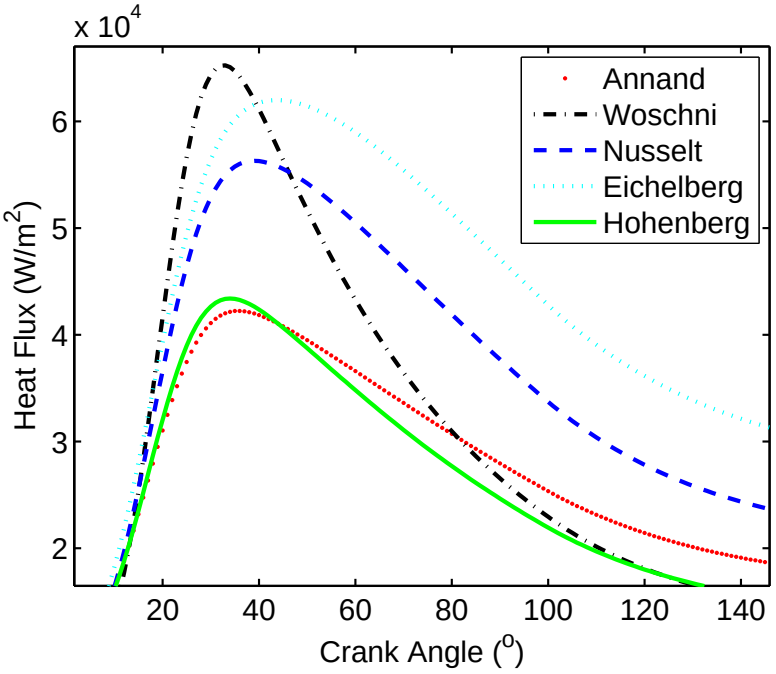

Figure 6.28: Zoomed-in plotting for simulated heat flux using previous heat transfer models for fired case.

tion 2.4) and 0.12 for Hohenberg's model (equation 2.10). Figure 6.27 presents the measured heat flux and the simulated heat flux, using the heat transfer models of Hohenberg, Nusselt, Annand, Eichelberg and Woschni. The figure shows that all of the existing heat transfer models underestimated the measured heat flux. Even though the shapes of the heat flux are somewhat similar to each other, the magnitude is still lower than the measured heat flux. Moreover, although each of these models has different parameters in predicting the heat flux, none of them was able to provide a close estimation of the measured heat flux. In figure 6.28 it can be seen that the peak values of the heat flux predicted using the previous model, seem to occur at different crank angles and also the decline of heat flux after the peak values occurs at different times.

6.4 Unscaled heat flux simulation

In this section, the unscaled versions of the different heat transfer models discussed in previous sections are used to compare with the measured heat flux values. The unscaled peak heat fluxes values for the WOT motored case, the FCT motored case and the fired case are presented in table 6.1. It can be noticed from this table that, for the WOT motored case, the unscaled version of Eichelberg's model shows no improvement in the simulated heat flux comparing to the scaled one. Whereas, the unscaled Annand's model shows a better prediction of the peak heat flux than the others. Moreover, the peak heat flux values from the unscaled models vary in a factor of 1.3 - 4. In the FCT motored case the unscaled version of Eichelberg's model shows a better agreement with the measured heat flux when compared to the scaled version. In this case the variation in the peak heat flux values from the different unscaled models is in order of 1.5 - 3.5. In the case of the fired engine the unscaled Woschni's model shows a closer agreement in the simulation of the peak heat flux than the scaled model. Furthermore, the difference in peaks between the different scaled models is in factor of 1.25 - 4. It can also be observed for the fired case that, the unscaled versions of Annand's and

Eichelberg's models have the same peak heat value. However, the use of unscaled version of these different models does not produce an accurate simulation of the measured pressure history.

Unscaled peak heat flux values(W/m^2)			
Heat transfer model	WOT motored case	FCT motored case	Fired case
Annand	8.16×10^4	7.49×10^4	8.16×10^5
Woschni	2.99×10^4	2.49×10^4	4.35×10^5
Eichelberg	3.92×10^4	5.33×10^4	8.16×10^5
Nusselt	2.62×10^4	3.06×10^4	6.53×10^5
Hohenberg	5.91×10^4	4.42×10^4	5.44×10^5
Measured peak	8.45×10^4	5.2×10^4	4.98×10^5

Table 6.1: Unscaled peak heat flux values from different heat transfer models.

6.5 Conclusion

In this chapter the results from the motored test were presented. The effect of two different throttle settings on the in-cylinder pressure and heat transfer were examined. The engine was tested under wide open and fully closed throttle settings. The results showed that throttling the engine resulted in reducing the mass of air trapped by the engine and this led to decreasing the in-cylinder pressure and temperature as well as the heat transfer. A Matlab routine was used in simulating the engine performance.

The heat transfer model proposed by Eichelberg was used in the Matlab routine for the engine simulation. A scaling factor was applied to Eichelberg's model. The scaling was used to achieve close agreement between the measured and simulated pressure results. The scaling factor was found to be 4.035 for the wide open throttle test and 0.208 for the fully closed throttle test. Some of the well known

heat transfer models were examined, to compare the measured heat transfer with the simulated heat transfer using those models with different scaling factors. In the case of the wide open throttle, all of the models tested overestimated the measured heat transfer, and it was found to be more than 1.9 in the case of the scaled Eichelberg's model. In the fully closed throttle test, the measured heat flux was underestimated, and in the case of the scaled Eichelberg's model it was more than 4.7 times.

In the case of the fired test, Woschni's model was used in the engine simulation. The scaling factor applied to this model to match the measured and the simulated pressure was found to be 0.15. The Wiebe function parameters for the mass fraction burned was found to be $a = 75$ and $m = 2.036$. In the simulation of the heat flux using the scaled Woschni's model there was no agreement achieved and it underestimated the measured heat flux by 7.6 times. The same approach was observed when some of the previous heat transfer models with different scaling factors were used and all of them under-predicted the measured heat flux.

When the unscaled version of Eichelberg's model used for the two motored cases, the predicted heat flux showed a better agreement in the FCT case with the measured one than the scaled model, whereas, in the WOT case there was no improvement achieved. For the fired case when the unscaled Woschni's model was applied, a better prediction in the simulated heat flux was obtained compared to the scaled model. On the other hand, the use of unscaled models produced an inaccurate simulation of the measured pressure history. Therefore, it seems likely that there are strong spatial variations in the heat flux which are not measured or simulated.

Chapter 7

Results from Unsteady Model

7.1 Experimental data

To explore the applicability of the the unsteady heat transfer model developed in this study and compare predicted heat fluxes with the measured ones, the results from the unsteady model simulation will be compared to the available experimental data. The experimental data covers three different sets of operating conditions, including two sets of motored engine and one fired engine case. The heat flux determined from the unsteady model simulation will be compared to the measured data in the wide open throttle and fully closed throttle motored case in addition to the fired case.

7.2 Numerical simulation conditions

In the finite difference routine for the solution of transient, one-dimensional, heat conduction problem built in Matlab, some of the numerical conditions and the gas properties are required. Those properties are identified from the engine simulation discussed in the previous chapter for each case. The averaged wall temperatures

and the trapped mass, are chosen based on the experimental data. The temperature change is chosen as 1 K and the time steps and the grid refinement values are chosen, based on the spatial and temporal step size independence checks performed for each case. In the unsteady model, all the three models for the turbulent viscosity presented in chapter 3 were examined and the heat flux results were almost identical for the all models. Therefore, the turbulent viscosity model presented in equation 3.31 with different constant values and models for turbulent Prandtl number will be used. A single fixed value for the thermal boundary layer thickness of 15.5 mm is assumed.

7.3 Results from unsteady model - motored case

The unsteady heat transfer model developed in this study is first tested on a motored engine case. As mentioned in chapter 6, the engine is tested under motored conditions, with wide open and fully closed throttle cases. The results from the unsteady model for those two cases with comparison to experimental results follows below.

7.3.1 Results from wide open throttle case

The unsteady thermal boundary layer model was run, using the gas properties identified from the engine simulation with Eichelberg's model (section 6.2.1). In the present modelling, a variable effective thermal turbulent conductivity was considered throughout the thermal boundary layer, instead of the constant value assumed in a previous work [61], and as discussed in chapter 4, section 4.3.2.

Time step and node spacing independence

Investigation of the solution independent from the time step and node spacing of the computation in numerical studies is essential. Once the independence is

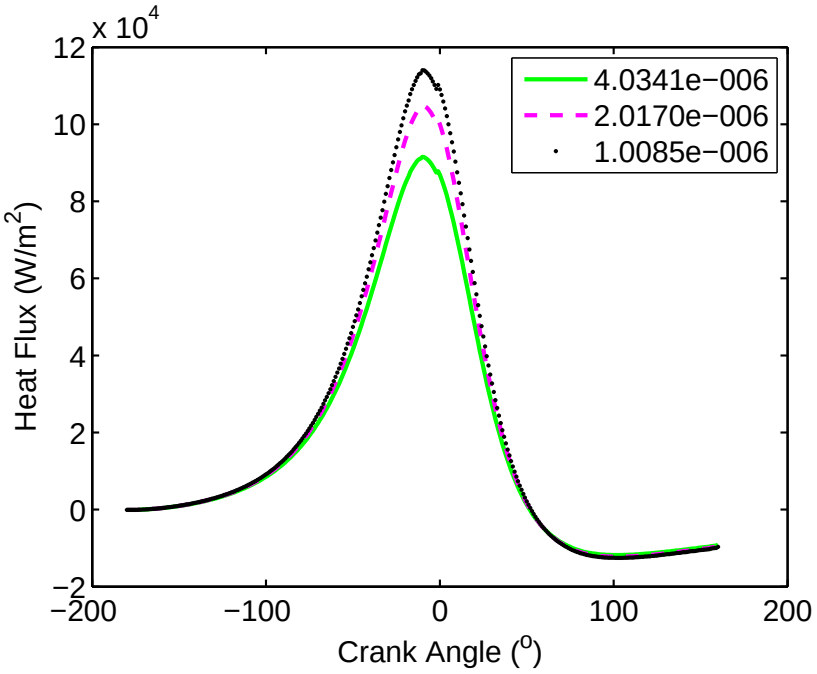

Figure 7.1: Heat flux sensitivity to node spacing ($Pr_t = 0.9$) for WOT motored case. Values in the legend corresponded to node spacing at the wall in units of m.

confirmed, the numerical results can be confidently compared with the experimental data. Time step and node spacing independence were investigated for all of the turbulent Prandtl number models presented in this study. The time step and node spacing independence test for the case of a constant turbulent Prandtl number of 0.9 and one of the variable turbulent Prandtl number models will be presented.

Three different time steps were tested for the wide open throttle case. The three time steps tested were 2.66×10^{-6} s, 5.31×10^{-6} s and 1.06×10^{-5} s. According to this test, the simulated heat flux was essentially identical for the three time steps. Consequently, the time step 1.06×10^{-5} s was chosen for the simulation.

When checking the node spacing (grid refinement) independence, it is desirable to minimise the total number of nodes, so as to reduce the computational time. However, a fine node spacing is required at the surface, to accurately resolve rapid changes in heat flux. The grid refinement was checked by changing the Fourier

number in the finite difference routine built in Matlab which was used in the simulation of the unsteady heat transfer model. Three different values for the node spacing were examined. These values were 4.03×10^{-6} m, 2.02×10^{-6} m and 1.01×10^{-6} m for the WOT case. The node spacing independence check is shown in figure 7.1 for the turbulent Prandtl number 0.9, and figure 7.2 for the turbulent Prandtl number using the formula in equation 3.21. The order of convergence of the numerical scheme was almost unity and error estimates based on the Richardson extrapolation indicated the error in the peak heat flux value for the smalest node spacing was around 7%. This was considered sufficiently accurate for the present work since unsteadies in the model parameters were typically much lower. Therefore, the node spacing of 1.01×10^{-6} m was chosen for the wide open throttle case.

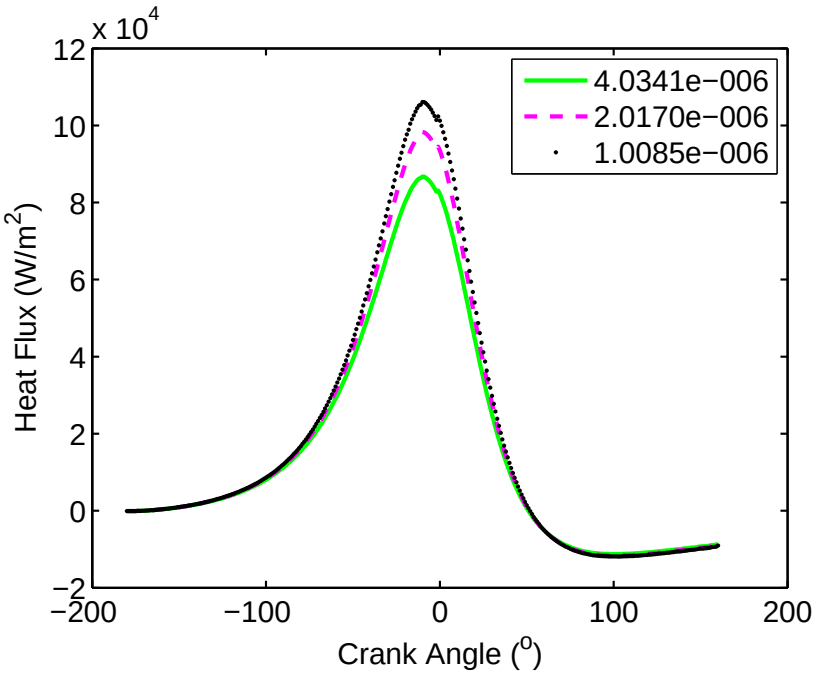

Figure 7.2: Heat flux sensitivity to node spacing (equation 3.21 for Pr_t) for WOT motored case. Values in the legend corresponded to node spacing at the wall in units of m.

In the examination of the effect of the turbulent Prandtl number on the simulated heat flux, three constant values of the turbulent Prandtl number were used

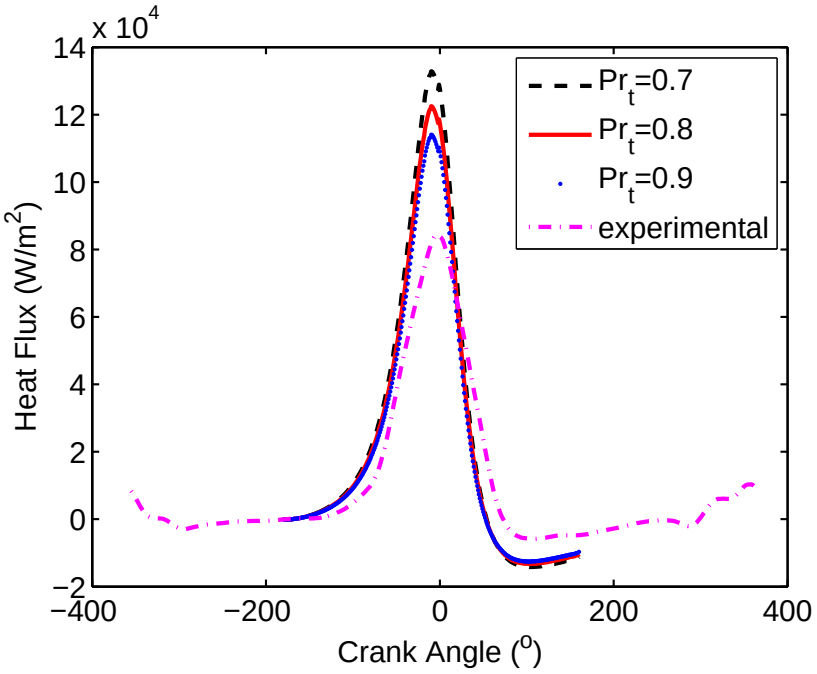

Figure 7.3: Measured and simulated heat flux using the unsteady model for WOT motored case, with constant turbulent Prandtl number values in the thermal conductivity model. Experimental data from the averaged heat flux for the three probes.

in the unsteady model. The three values were 0.7, 0.8 and 0.9. The simulated heat flux results obtained from these values are shown in figure 7.3. It can be observed from this figure that as the turbulent Prandtl number increases, the heat flux decreases. It also demonstrates that the unsteady model overestimates the measured heat flux and the predicted heat fluxes start to increase and drop faster than the measured one. Furthermore, all the three peaks of the simulated heat flux occur at the same crank angle 10° CA BTDC. The error in the peaks between the measured and the simulated heat flux is found to be 57.29 % for the value of 0.7, about 45.04 % for 0.8 and 35.02 % when the value of 0.9 is used. It seems that increasing the value of the Prandtl number in the unsteady model could improve the prediction of the heat flux.

In order to examine the prediction of heat flux using the unsteady model, the turbulent Prandtl number models presented in equation 3.21 and equation 3.29 are

used to simulate the heat flux in the unsteady model. These two models for the turbulent Prandtl number provide a very close estimation of the measured heat flux, with the smallest error between the measured and the simulated peaks.

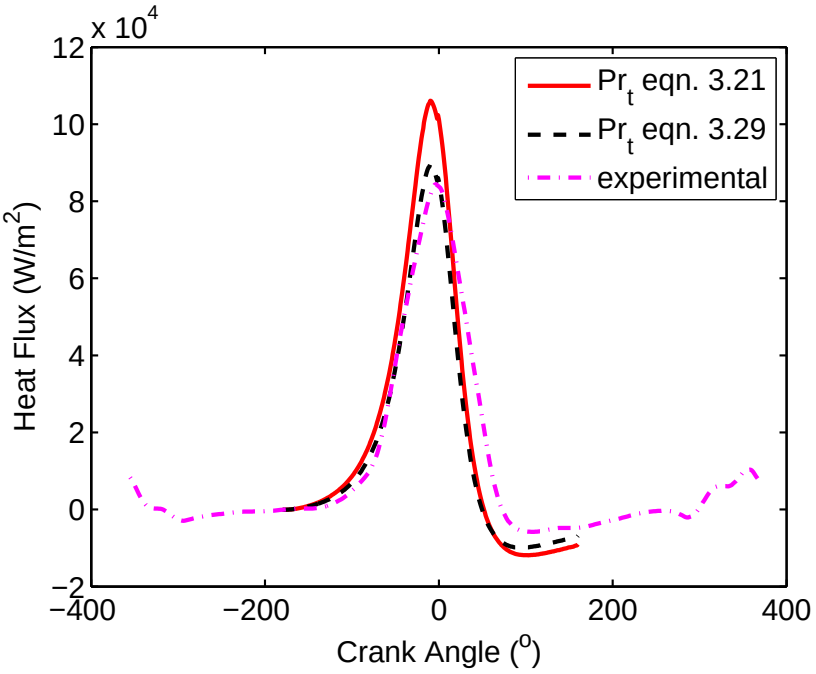

Figure 7.4: Measured and simulated heat flux using the unsteady model for WOT motored case, with variable turbulent Prandtl number values in the thermal conductivity model. Experimental data from the averaged heat flux for the three probes.

The heat flux from the unsteady model is presented in figure 7.4. In figure 7.4 it can be seen that the heat flux simulated using the unsteady approach starts to rise more rapidly than the measured heat flux at about 160° CA before top dead centre, whereas at about 60° CA BTDC they seem to rise simultaneously. The simulated heat flux using the turbulent Prandtl number in equation 3.21 has the highest peak value, followed by the simulated heat flux using the turbulent Prandtl number in equation 3.29 and the measured heat flux. The peak heat flux values for the two simulated heat fluxes occur at the same crank angle (10° CA BTDC), while the measured one occurs slightly later at 3.25° CA BTDC. The figure demonstrates that, just after the top dead centre, the two simulated heat

fluxes decline more rapidly than the measured one. The error in the peak values between the simulated and measured heat flux is found to be 6.03 % and 25.63 % for the turbulent Prandtl number, using equation 3.29 and equation 3.21 respectively. An overall agreement between the measured and the simulated heat flux can be observed from this figure.

All of the turbulent Prandtl number models mentioned earlier in this study were examined and the errors in the peaks between the measured heat flux and the predicted heat flux using those models are presented in table 7.1.

Turbulent Prandtl number model	Error in peak values %
Equation 3.20	38.17
Equation 3.23	87.05
Equation 3.24	103.57
Equation 3.21	25.63
Equation 3.25	35.24
Equation 3.22	28.14
Equation 3.29	6.03
Pr_t=0.7	57.29
Pr_t=0.8	45.04
Pr_t=0.9	35.02

Table 7.1: Error in peaks between measured and predicted heat flux using the unsteady model, with different turbulent Prandtl number models in the turbulent thermal conductivity model for the WOT motored case. All models have overestimated the peak heat flux value.

7.3.2 Results from fully closed throttle case

The gas properties identified from the engine simulation with Eichelberg's model (section 6.2.2) for the FCT case are used to run the unsteady thermal boundary layer

model. The same trend in choosing the turbulent viscosity model in the WOT case, is used in this case and the same constant values for the turbulent Prandtl number with the two variable models are chosen for this case in the simulation of the heat flux in the unsteady model, with a brief illustration for the other models.

Time step and node spacing independence

When checking the time step independence, another three different time steps, were tested for the fully closed throttle case. The three time steps tested are 2.66×10^{-6} s, 5.33×10^{-6} s and 1.07×10^{-5} s. As observed in the WOT case, the peak heat flux was found to be virtually identical for the cases studied. The time step 1.07×10^{-5} s is chosen for the simulation.

To investigate the effect of the node spacing (grid refinement) independence on the computation in the FCT case, another three values for the node spacing were examined by changing the Fourier number in the simulation routine. These three values are 7.16×10^{-6} m, 3.58×10^{-6} m and 1.79×10^{-6} m. Figure 7.5,

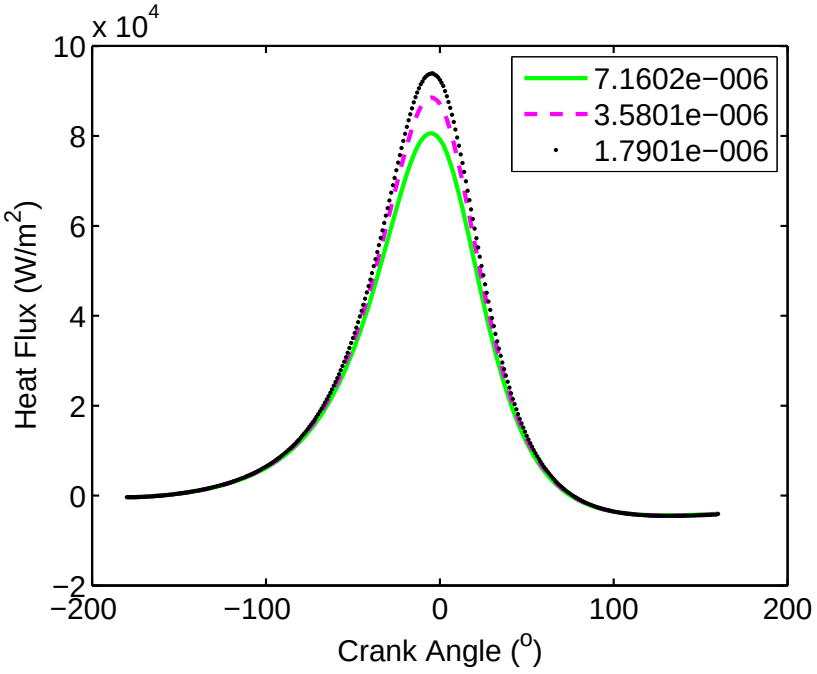

Figure 7.5: Heat flux sensitivity to node spacing ($Pr_t = 0.9$) for FCT motored case. Values in the legend corresponded to node spacing at the wall in units of m.

showing the sensitivity of the node spacing on heat flux for the turbulent Prandtl number 0.9, and figure 7.6 for the turbulent Prandtl number using the formula in equation 3.21. The Richardson extrapolation was also performed for this case and the order of convergence of the numerical scheme was found to be almost unity. Error estimates based on the Richardson extrapolation for the peak heat flux value at the smallest node spacing was about 5%. Therefore, the node spacing of 1.79×10^{-6} m was chosen for this case.

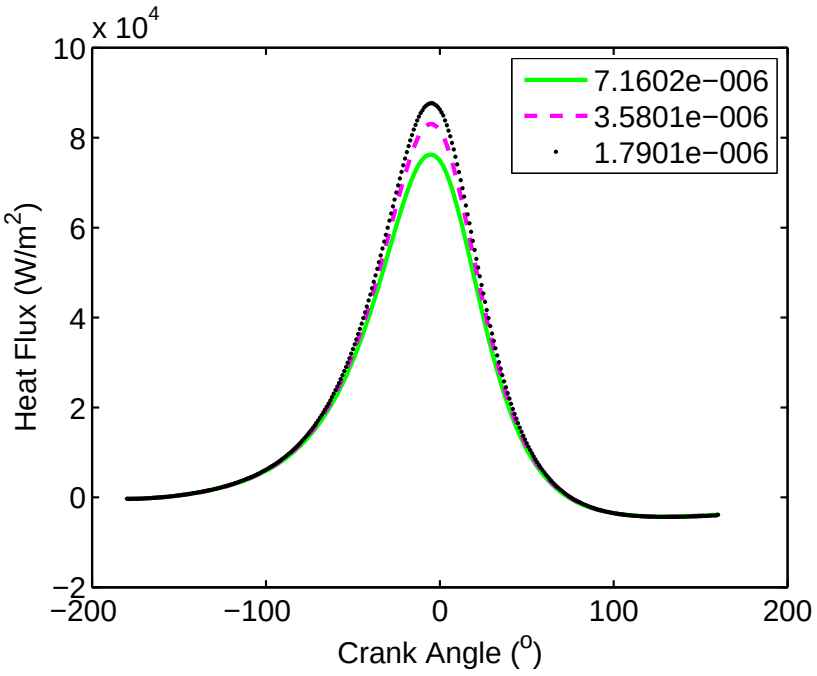

Figure 7.6: Heat flux sensitivity to node spacing (equation 3.21 for Pr_t) for FCT motored case. Values in the legend corresponded to node spacing at the wall in units of m.

Three different constant values of the turbulent Prandtl number were examined in the unsteady model. Values of 0.7, 0.8 and 0.9 were applied. Figure 7.7 shows the simulated heat flux obtained from the unsteady model, using those three values compared with the measured heat flux. The figure demonstrates that, the higher the turbulent Prandtl number, the smaller the heat flux. The figure also shows that the predicted heat flux from all three values of turbulent Prandtl number seems to increase simultaneously and more rapidly than the measured heat flux,

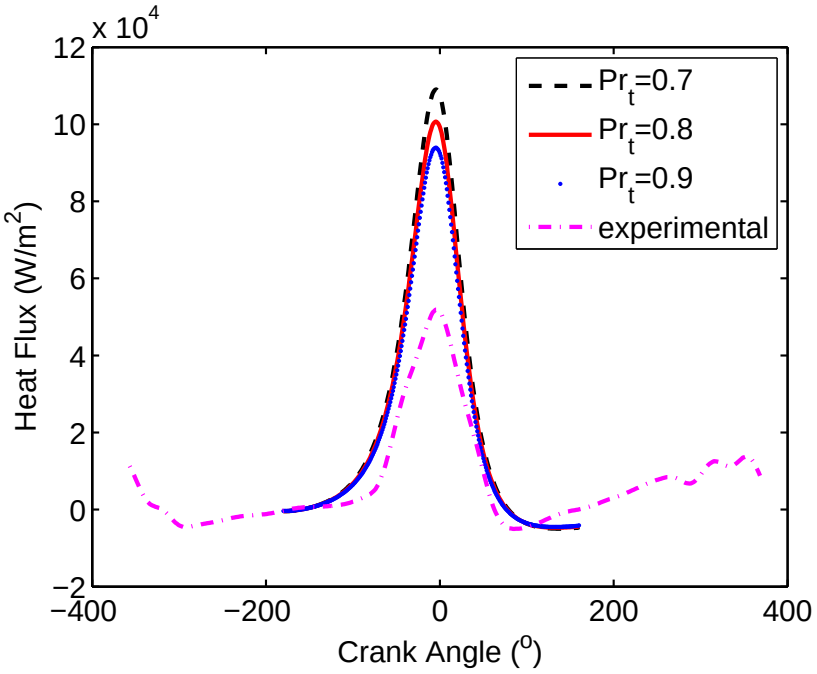

Figure 7.7: Measured and simulated heat flux using the unsteady model for FCT case, with constant turbulent Prandtl number values in the thermal conductivity model. Experimental data from the averaged heat flux for the three probes.

whereas the measured heat flux declines faster than the predicted ones. It is also observed that the unsteady model overestimates the measured heat flux, and the peak values of the simulated heat flux occur at the same crank angle (5° CA BTDC), while the measured peak occurs slightly later at 3.2° CA BTDC. The error in the peak values between the simulated heat flux and the measured one is found to be more than 110 % for the case of Pr_t= 0.7, about 94 % for the case of Pr_t= 0.8 and 80.98 % for Pr_t= 0.9. It can be observed that using constant values for the turbulent Prandtl number in the unsteady model improved the heat flux estimation, in comparison to the use of the empirical Eichelberg's correlation discussed earlier.

The heat flux from the unsteady model in the FCT case is presented in figure 7.8, using two different models for the variable turbulent Prandtl number (equation. 3.21 and equation. 3.29). The figure demonstrates that the predicted heat flux using the unsteady approach starts to rise and drop more rapidly than

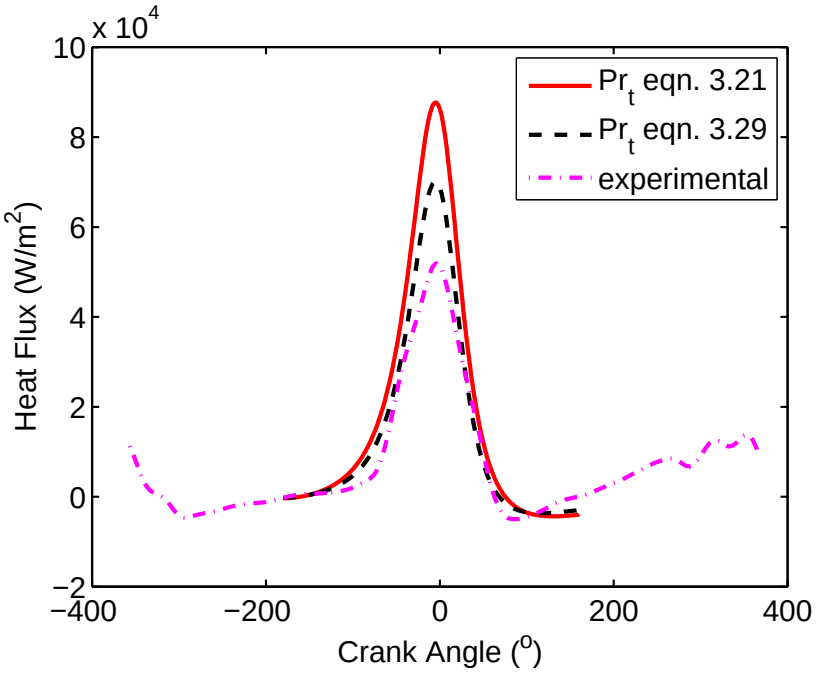

Figure 7.8: Measured and simulated heat flux using the unsteady model for FCT motored case, with variable turbulent Prandtl number values in the thermal conductivity model. Experimental data from the averaged heat flux for the three probes.

the measured heat flux during most of the engine cycle, however, at about 35° CA ATDC they seem to decline simultaneously. As was observed in the WOT case, the simulated heat flux using the turbulent Prandtl number in equation 3.21 tends to have the highest peak value, followed by the simulated heat flux using the turbulent Prandtl number in equation 3.29 and then the measured heat flux.

Moreover, the peak heat flux values for the two simulated heat fluxes occur at the same crank angle (5° CA BTDC), while the measured one occurs later at 3.2° CA BTDC. The error in the peak values between the simulated and measured heat flux is higher than what was observed in the WOT case and it is found to be about 35 % and 68.95 % for the turbulent Prandtl number using equation 3.29 and equation 3.21 respectively. Although the fact that the magnitude of the simulated heat flux using the unsteady approach seems to somehow overestimate the measured heat flux, there is a reasonable agreement in the phasing of the heat flux. It can

also be observed that the unsteady model provides a better prediction of the heat flux in contrast to the results obtained for the empirical model proposed by Eichelberg, presented in figure 6.18, and the case of the constant turbulent Prandtl number values discussed above. Furthermore, this level of agreement between the results can be accepted to some extent as the measured data was taken from only three measuring locations in the combustion chamber which is unlikely to reflect in the actual spatial variation of heat transfer in the chamber, and also because the maximum value for each location is somewhat different to another one, which can be seen in figure 6.16 in the previous chapter.

Table 7.2 presents the errors in peaks between the measured and simulated heat flux from different turbulent Prandtl number models.

Turbulent Prandtl number model	Error in peak values %
Equation 3.20	85.15
Equation 3.23	87.05
Equation 3.24	103.57
Equation 3.21	68.95
Equation 3.25	75.74
Equation 3.22	72.24
Equation 3.29	35.01
Pr_t=0.7	110.16
Pr_t=0.8	94.06
Pr_t=0.9	80.98

Table 7.2: Error in peaks between measured and predicted heat flux using the unsteady model, with different turbulent Prandtl number models in the turbulent thermal conductivity model for the FCT motored case. All models have overestimated the peak heat flux value.

7.4 Results from fired case

The unsteady thermal boundary layer model for the fired case is run using the gas properties identified from the engine simulation with Woschni's model in section 6.3. In this section the the predicted heat flux from the unsteady model for three constant turbulent Prandtl number values and different turbulent Prandtl number models is discussed and compared to the measured results.

Time step and node spacing independence

In the time step independence check, three different time steps for the fired engine case were tested. The three time steps tested are 1.69×10^{-6} s, 3.39×10^{-6} s and 6.7730×10^{-6} s. The check of the time steps independence on the heat flux was carried out in this case and it showed no significant effect of the these changes on the heat flux. Therefore, the time step 6.77×10^{-6} s was chosen to be used in the simulation.

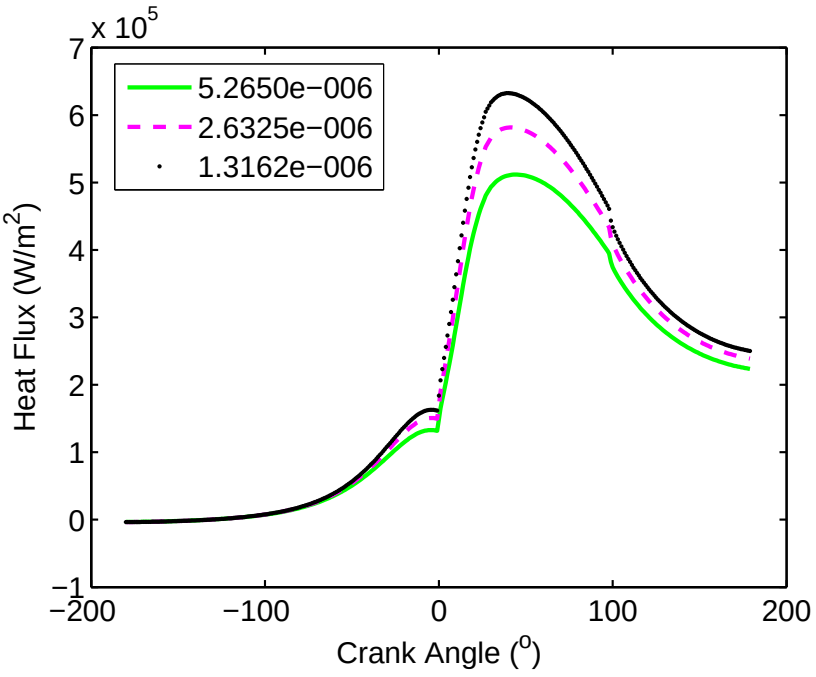

Figure 7.9: Heat flux sensitivity to node spacing ($Pr_t = 0.9$) for fired case. Values in the legend corresponded to node spacing at the wall in units of m.

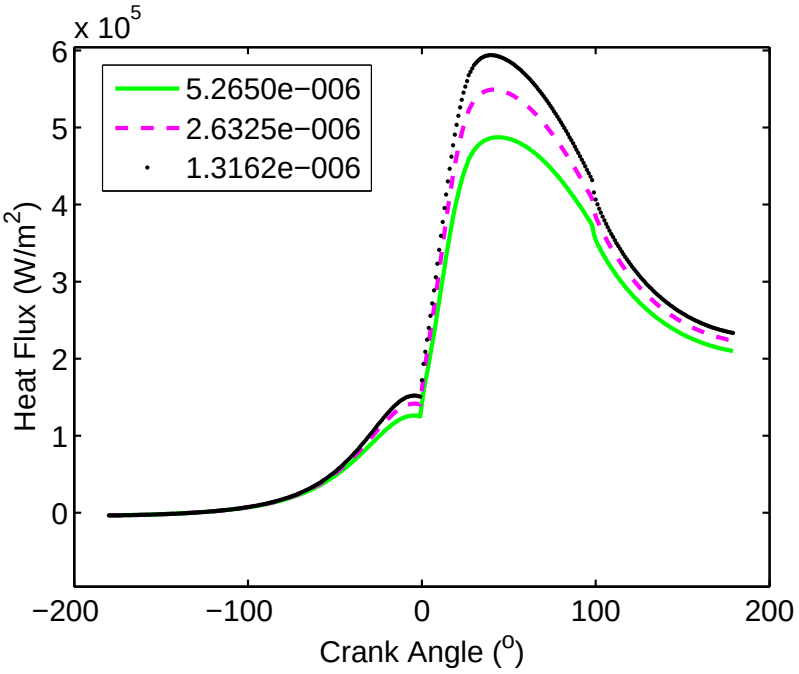

Figure 7.10: Heat flux sensitivity to node spacing (equation 3.21 for Pr_t) for fired case. Values in the legend corresponded to node spacing at the wall in units of m.

The effect of the node spacing was also checked in this case and three different values for the node spacing were tested. Those values are 5.27×10^{-6} m, 2.63×10^{-6} m and 1.32×10^{-6} m. The sensitivity check was made on all of these values and it was found that the heat flux is weakly affected by the change in the node spacing values. The Richardson extrapolation was performed for the fired case and the order of convergence of the numerical scheme was also found to be almost unity and error estimates based on the Richardson extrapolation in the peak heat flux value for the smallest node spacing used was found to be about 8%. The value of 1.32×10^{-6} m for the node spacing was chosen in the fired engine test simulation. The effect of variable node spacing on heat flux is illustrated in figure 7.9 and figure 7.10 for constant turbulent Prandtl number 0.9 and for variable turbulent Prandtl number using the equation 3.21.

In the case of the fired engine the three constant values for the turbulent Prandtl number used in the two previous (motored) cases are used in this case. Fig-

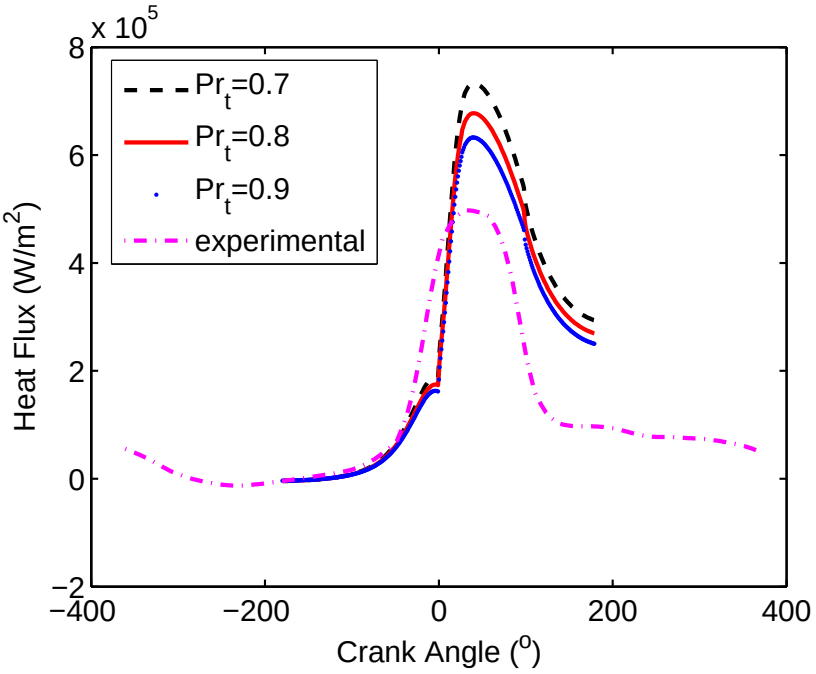

Figure 7.11: Measured and simulated heat flux using the unsteady model for fired case, with constant turbulent Prandtl number values in the thermal conductivity model. Experimental data from the averaged heat flux for the three probes.

ure 7.11 presents the effect of different turbulent Prandtl number values on the heat flux. The figure demonstrates that the unsteady model over-predicts the measured heat flux for all constant values used. This figure also shows that the measured heat flux starts to rise and decline more rapidly than the predicted heat flux. It can also be noticed that the simulated peaks occur at the same crank angle of about 40° CA ATDC and the measured one occurs earlier at 31° CA ATDC. The error between the simulated peak heat flux and the measured value is found to be more than 47 % for the turbulent Prandtl number value of 0.7, about 36 % for the case of 0.8 and 27.09 % for the Prandtl number 0.9. It can be observed that using constant values for the turbulent Prandtl number in the unsteady model adds some improvement to the prediction of the heat flux, in contrast to the quasi-steady models used in the previous chapter, but they still overestimate the measured heat flux.

The predicted heat flux from the unsteady model in the fired case is demonstrated

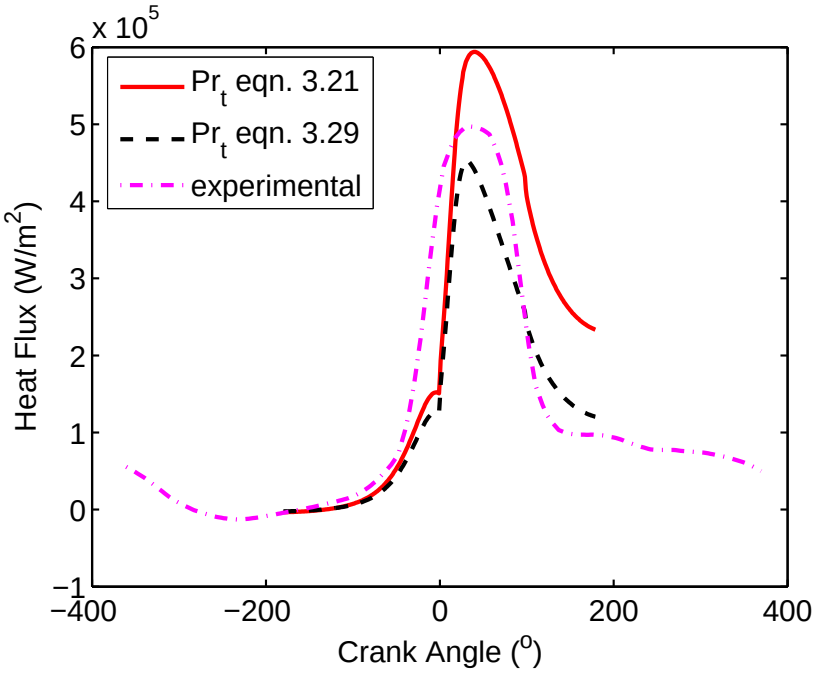

Figure 7.12: Measured and simulated heat flux using the unsteady model for fired case, with variable turbulent Prandtl number values in the thermal conductivity model. Experimental data from the averaged heat flux for the three probes.

in figure 7.12 using the two different models for the variable turbulent Prandtl number (equation. 3.21 and equation. 3.29). The figure shows that the measured heat flux starts to rise more rapidly than the simulated ones using the unsteady model. The figure also shows that the two simulated heat fluxes seem to increase simultaneously during the compression stage and most of the combustion stage, whilst the predicted heat flux using the turbulent Prandtl number in equation 3.21 declines faster than the another simulated one. Moreover, the simulated heat flux using the turbulent Prandtl number in equation 3.21 seems to have the highest peak and it overestimates the measured heat flux, whereas the predicted heat flux using the turbulent Prandtl number in equation 3.29 underestimates the measured heat flux. It can also be observed that the peak heat flux value for the heat flux obtained from the unsteady approach using the equation 3.29 for the turbulent Prandtl number, and the measured peak occur at about the same crank angle 30° CA ATDC, whilst the simulation of Prandtl number in equation 3.21

occurs later at 40° CA ATDC. The error between the predicted and measured peak heat flux is found to be about 9.04 % when the formula in equation 3.29 for the turbulent Prandtl number is used, and about 19.32 % using the formula in equation 3.21. It can be seen that a reasonable agreement is achieved with a reduction in the error between peaks compared to the results obtained from the quasi-steady model proposed by Woschni presented in figure 6.26, and the results from the unsteady model using the constant values for the turbulent Prandtl number.

The error between the predicted peak values and the measured one, using all of the different turbulent Prandtl number models mentioned in section 3.3.1, is reported in table 7.3. The table illustrates that peak value of the measured heat flux is overestimated by the all of these models except the model in equation 3.29.

Turbulent Prandtl number model	Error in peak values %
Equation 3.20	30.26
Equation 3.23	31.30
Equation 3.24	40.53
Equation 3.21	19.32
Equation 3.25	20.85
Equation 3.22	21.96
Equation 3.29	-9.04
Pr_t=0.7	47.28
Pr_t=0.8	36.15
Pr_t=0.9	27.09

Table 7.3: Error in peaks between measured and predicted heat flux using the unsteady model, with different turbulent Prandtl number models in the turbulent thermal conductivity model for the fired case. Models generally overestimate the peak heat flux.

7.5 Application to other engines

In this section, the unsteady heat transfer model will be applied to other engines to validate this method of investigating the heat flux from those engines. The data from engines discussed in an earlier chapter (chapter 4) will be used in this simulation. The data from the work of Wu et al. [5] and [6] will be used and discussed in the heat flux simulation using the unsteady model. The designations "engine A" and "engine B" refer to the engines used by Wu et al. [5] and [6] respectively. The unsteady thermal boundary layer model was run using the gas properties identified from the engine simulation for these engines discussed in section 4.3.1. The turbulent Prandtl number model in equation 3.29 was used in the turbulent conductivity model in the unsteady heat transfer model.

Time step and node spacing independence

The time step and grid refinement independence checks were performed for these engines and the following values were chosen. For engine A the time step chosen was 2.498×10^{-6} s and the node spacing was 7.246×10^{-7} m; for engine B the time step and node spacing chosen were 2.498×10^{-6} s and 7.751×10^{-7} m respectively.

The simulated heat flux obtained from the unsteady model is presented with the experimental heat flux for engine A and B in figure 7.13 and figure 7.14 respectively. Figure 7.13 shows that the simulated heat flux starts to rise and decline more rapidly than the measured one, whereas in figure 7.14, the simulated heat flux increases faster than the measured one, but the measured one seems to drop more rapidly. Moreover, it can be seen for engine A in figure 7.13 that the predicted peak occurs earlier than the measured peak at 17° CA ATDC and the measured one occurs at about 26° crank angle after top dead centre. For the engine B in figure 7.14 the simulated peak occurs slightly later than the measured one at about 16° crank angle after top dead centre, whereas the measured one occurs at about 13° CA ATDC. It can also be noticed that the simulated peak using the unsteady model is higher than the measured one for engine A and

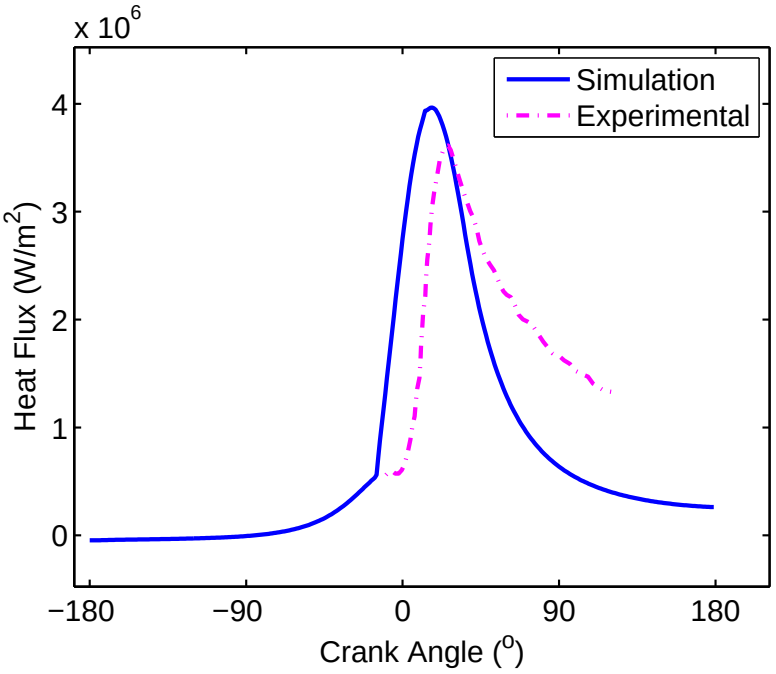

Figure 7.13: Measured and simulated heat flux using the unsteady model (Engine condition A).

smaller than the measured one for engine B, as shown in figures 7.13 and 7.14 respectively. The error in peaks between the measured and the simulated one is found to be 9.4 % for engine A and 17.3 % for engine B. The simulation of heat flux using the unsteady approach developed in this study shows an improvement in predicting the heat flux compared to the unsteady model with a constant turbulent conductivity shown in chapter 4. This level of agreement in predicting the heat flux might be improved if the engine's operating parameters such as the intake pressure and temperature and the trapped mass were available from the experiments in the work of [5] and [6] instead of tuning some parameters to match the pressure trace to validate the engine simulation.

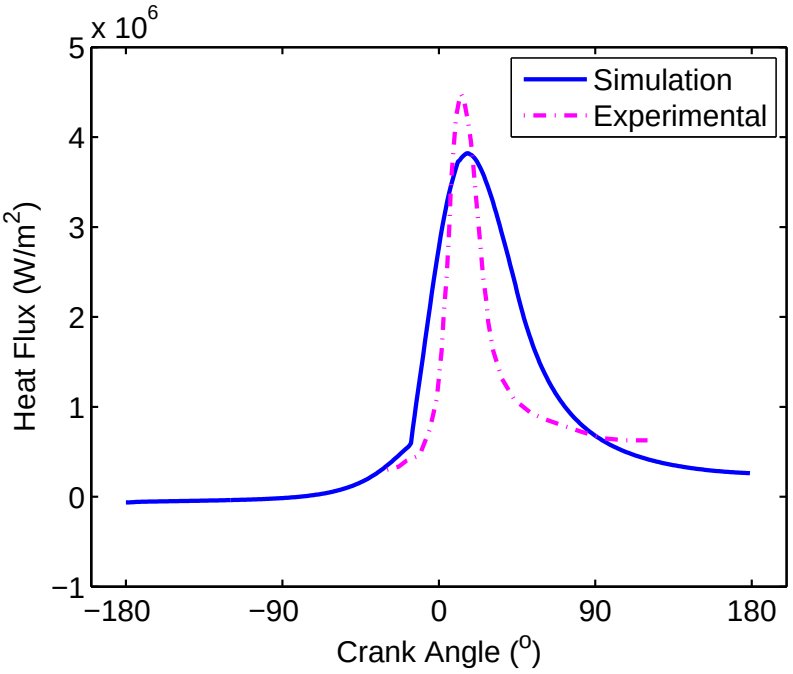

Figure 7.14: Measured and simulated heat flux using the unsteady model (Engine condition B).

7.6 Conclusion

In this chapter, the unsteady model developed in this study was examined and validated on different engine operating conditions. The model was tested in a motored engine with two different throttling settings (wide open and fully closed throttle) and one fired engine case. A finite difference routine built in Matlab was used in the simulation of this model. The numerical conditions and the gas properties for this simulation were identified from the experimental data and the engine simulations discussed in the previous chapter. For the numerical simulation the time-step independence check was performed for each case. Three different time steps were tested for the three cases. According to this test it was observed that the heat flux tends to converge for the all time steps examined and the highest time step for each case was chosen.

In validating the unsteady model, different turbulent Prandtl number models

were implemented in the thermal conductivity model, as well as examining three constant values for the turbulent Prandtl number, with the assumption of a fixed value of the thermal boundary layer thickness. The simulation showed different values for the error in peaks between the measured and predicted heat flux for each value of the turbulent Prandtl number for each engine case tested. For the constant turbulent Prandtl values, the errors in peaks were found to be 57.29 % for the value of 0.7, about 45.04 % for 0.8 and 35.02 % for the value of 0.9 in the WOT case. For the FCT case, the errors were found to be higher than in the case of the WOT test and they were 110.16 % for the case of 0.7, about 94.06 % for the case of 0.8 and 80.98 % for the Prandtl number 0.9. For the fired case, the errors were found to be more than 47.28 % for the turbulent Prandtl number value of 0.7, about 36.15 % for the case of 0.8 and 27.09 % for the turbulent Prandtl number 0.9. It would be observed that the prediction of the heat flux was improved by using the unsteady approach in contrast to the simulated results obtained from the quasi-steady heat transfer models discussed in chapter 6.

More improvement was achieved when variable turbulent Prandtl number models were applied. Five different formulae for the turbulent Prandtl number were examined. The heat flux estimation was better predicted with those models and the error in the peaks was found to be lower than that obtained from the constant turbulent Prandtl number values. The model proposed by Reynolds [74] and the model proposed by Myong [69] provided the lowest errors of all models. In the WOT case the errors were found to be 6.03% and 25.63%, for the FCT case the errors were 35.01% and 68.95 % and for the fired test case the errors at the peak were 9.04 % and 19.32 % for these two turbulent Prandtl number models respectively. It can be concluded that the heat transfer model developed in this study using the unsteady approach, provides a very good agreement with measured results in contrast to the existing quasi-steady models. Moreover, the implementation of an effective variable thermal conductivity adds a reasonable level of improvement to the simulation of engine heat transfer compared with previous studies using a constant thermal conductivity model. Furthermore, it

is also concluded that the turbulent thermal conductivity model with a variable turbulent Prandtl number using Reynolds' formula, gives better estimation than the other models examined. Although, a fixed single value was assumed for the thermal boundary layer thickness, the study showed that, the simulation results have only a small sensitivity to the boundary layer thickness and that the assumed thickness value was close to the values simulated near TDC.

The current approach has some limitations. Although an unsteady thermal boundary layer equation is being solved, the models for turbulent Prandtl number and turbulent viscosity are derived from quasi-steady flow data which might not be generally applicable in the internal combustion engine environment. Furthermore, the choice of the model can have a significant impact on the simulated heat flux values depending on the conditions.

Chapter 8

Conclusions and future suggestions

8.1 Summary

The lack of studies which provide sufficient details on pressure history and heat flux data in engines and the uncertainty in the captured mass values, provides the necessary stimulation to perform experiments to obtain the pressure history and heat flux data, in order to improve the unsteady heat transfer modelling in internal combustion engines.

An experimental and computational study on heat transfer in internal combustion engines has been conducted on a spark ignition engine. The experiments were performed under motored and fired conditions. The engine simulation was performed using a quasi one-dimensional spark ignition engine Matlab simulation program. This program was run using some of the essential engine parameters such as, bore, stroke, compression ratio and connecting rod length, in addition to the operating parameters from the experiments. Those parameters include intake pressure and temperature, air flow rate and the engine speed.

In the experimental process the engine surface temperatures were collected, using a set of E-type coaxial thermocouples. Those thermocouple probes were designed and fabricated by the author in the laboratories of the University of Southern Queensland. The surface temperature history was used to calculate the heat transfer rates from the gases to the cylinder walls. In this experiment, the engine was tested under wide open and fully closed throttle motored engine conditions and under fired engine condition.

In the engine simulation, different quasi-steady heat transfer models were implemented in order to investigate the difference in heat transfer rates from each model. In this study, an unsteady heat transfer model with emphasis on thermal boundary layer modelling to improve the prediction of heat transfer in internal combustion engines was investigated. The heat transfer model was developed, based on the unsteady thermal boundary layer with the implementation of variable turbulent thermal conductivity. For the calculations of the turbulent thermal conductivity, different turbulent Prandtl number and turbulent viscosity models were applied. The heat transfer rates from those models were obtained and compared with the experimental results.

8.2 Conclusions

The following conclusions were drawn from this study:

- The simulation of engine heat flux, using some of the existing convective heat transfer models, shows no agreement with the measured heat fluxes for all of the cases studied when the heat flux model is tuned so that the simulated pressure history matches the experimental results.
- All of the turbulent viscosity models examined in this study provide nearly identical heat flux results in the unsteady model.

- Different heat flux values have been obtained from different turbulent Prandtl number models, and a significant effect of the turbulent Prandtl number on the simulation of engine heat flux has been observed.
- Using the turbulent Prandtl number formula proposed by Reynolds [74] in the turbulent conductivity model, has shown a very good agreement between the measured and the simulated heat flux.
- The simulation results have only a small sensitivity to the boundary layer thickness.
- The thermal boundary layer thicknesses in the unsteady model are relative significant to the internal combustion engine clearance height and therefore, no isothermal core can be assumed.

8.3 Suggestions for future work

In this study, a heat transfer model based on the unsteady approach which might improve the prediction of heat transfer in internal combustion engines was presented. Future efforts relating to this work might consider the following directions.

- Further experimental studies for complete reporting of engine parameters and instantaneous heat flux data.
- Additional studies on a range of different engines operated over a wide range of conditions.
- Investigation of the applicability of turbulence models in the unsteady environments associated with internal combustion engines.
- Further investigations into the appropriate choice of existing turbulent Prandtl number and turbulent viscosity models for internal combustion engine applications.

- The implementation of variable thermal boundary layer thickness.
- Coupled unsteady simulations to account for heat loss from the entire volume of the gas.

References

[1] G. Horrocks, "A numerical study of a rotary valve internal combustion engine," Ph.D. dissertation, The University oF Technology, Sydney, 2001.

[2] W. Pulkrabek, *Engineering fundamentals of the internal combustion engine.* Upper Saddle River, New Jersey: Prentice Hall, 1997.

[3] J. Heywood, *Internal Combustion Engine Fundamentals*, 1st ed. New York, NY: McGraw-Hill, 1988.

[4] J. Demuynck, S. Pauwels, S. Verhelst, M. De Paepe, and R. Sierens, "Experimental research on the heat transfer inside a hydrogen combustion engine: evaluation and construction of measurement methods," *Proceedings of the FISITA 2008 World Automotive Congress (F2008-SC-037)*, 2008.

[5] Y. Wu, B. Chen, F. Hsieh, and C. Ke, "Heat transfer model for small-scale spark-ignition engines," *International Journal of Heat and Mass Transfer*, vol. 52, pp. 1875–1886, 2009.

[6] Y. Wu, B. Chen, and F. Hsieh, "Heat transfer model for small-scale air cooled spark-ignition four-stroke engines," *International Journal of Heat and Mass Transfer*, vol. 49, pp. 3895–3905, 2006.

[7] A. Alkidas, P. Puzinauskas, and R. Peterson, "Combustion and heat transfer studies in a spark-ignition multivalve optical engine," *SAE paper*, no. 900353, 1990.

[8] Thermo Alloys, "Thermo Alloys - Data Sheets," [Online]. Available:http://www.thermo-alloys.com/datasheets.html.

[9] B. Hollis, "User's manual for the one-dimensional hypersonic aerothermodynamic (1DHEAT) data reduction code," *NASA CR*, vol. 4691, 1995.

[10] R. Stone, *Introduction to internal combustion engines*, 3rd ed. Chippenham, Wiltshire: Antony Rowe Ltd, 1999.

[11] D. Nijeweme, J. Kok, C. Stone, and L. Wyszynski, "Unsteady in-cylinder heat transfer in a spark ignition engine: experiments and modelling," *Proc Instn Mech Engrs*, vol. 215, no. Part D, pp. 747–760, 2001.

[12] G. Borman and K. Nishiwaki, "Internal combustion engine heat transfer," *Prog. Energy Combust. Sci.*, vol. 133, pp. 1–46, 1987.

[13] W. Annand, "Heat transfer in cylinders of reciprocating internal combustion engines," *Proc Instn Mech Engrs*, vol. 177, no. 36, pp. 973–990, 1963.

[14] G. Woschni, "A universally applicable equation for the instantaneous heat transfer coefficient in the internal combustion engine," *SAE paper*, no. 670931, 1967.

[15] C. A. Finol and K. Robinson, "Thermal modelling of modern engines: a review of empirical correlations to estimate the in-cylinder heat transfer coefficient," *Proc. IMechE*, vol. 220, no. D, pp. 1765–1781, 2006.

[16] A. Torregrosa, P. Olmeda, and C. Romero, "Revising engine heat transfer," *Annals of Faculty of Engineering Hunedoara Journal of Engineering*, vol. 6, 2008.

[17] G. Sitkei, G. Ramanaiah, and S. O. A. Engineers, "A rational approach for calculation of heat transfer in diesel engines," *Society of Automotive Engineers, 400 Commonwealth Dr, Warrendale, PA, 15096, USA*, 1972.

[18] S. Han, Y. Chung, Y. Kwon, and S. Lee, "Empirical formula for instantaneous heat transfer coefficient in spark ignition engine," *SAE paper*, no. 972995, 1997.

[19] P. Shayler, S. May, and T. Ma, "Heat transfer to the combustion chamber walls in spark ignition engines," *SAE paper*, no. 950686, 1995.

[20] A. Sharief, T. Chandrashekar, A. Antony, and B. Samaga, "Study on heat transfer correlation in IC engines," *SAE paper*, no. 2008-01-1816, 2008.

[21] V. Rao and M. Bardon, "Convective heat transfer in reciprocating engines," *Proc Instn Mech. Engrs*, vol. 199, no. D3, pp. 221–226, 1985.

[22] T. Oguri, "On the coefficient of heat transfer between gases and cylinder walls of the spark-ignition engine," *Bulletin of JSME*, vol. 3, no. 11, pp. 363–369, 1960.

[23] H. Hassan, "Unsteady heat transfer in a motored IC engine cylinder," *Proceedings of the Institution of Mechanical Engineers*, vol. 185, no. 1, pp. 1139–1148, 1970.

[24] Y. Enomoto and S. Furuhama, "A study of the local heat transfer coefficient on the combustion chamber walls of a four-stroke gasoline engine," *JSME*, vol. 32, no. 1, pp. 107–114, 1989.

[25] A. Sanli, C. Sayin, M. Gumus, I. Kilicaslan, and M. Canakci, "Numerical evaluation by models of load and spark timing effects on the in-cylinder heat transfer of a SI engine," *Numerical Heat Transfer*, vol. 56, pp. 444–458, 2009.

[26] X. Wang, P. Price, R. Stone, C, and D. Richardson, "Heat release and heat transfer in a spray-guided direct-injection gasoline engine," *Proceedings of the Institution of Mechanical Engineers*, vol. 221 Part D, no. 11, pp. 1441–1452, 2007.

[27] T. Uchimi, K. Taya, Y. Hagihara, S. Kimura, and Y. Enomoto, "Heat loss

to combustion chamber wall in a D.I diesel engine - first report: Tendency of heat loss to piston surface," *JSAE*, vol. 21, pp. 133–135, 2000.

[28] K. Hoag, "Measurements and analysis of the effect of wall temperature on instantaneous heat flux," *SAE paper*, no. 860312, 1986.

[29] A. Alkidas, "Heat transfer characteristics of a spark-ignition engine," *ASME-Journal of Heat transfer*, vol. 102, pp. 189–193, 1980.

[30] A. Alkidas and J. P. Myers, "Transient heat-flux measurements in the combustion chamber of a spark-ignition engine," *ASME- Journal of Heat transfer*, vol. 104, pp. 62–67, 1982.

[31] Y. Harigaya, F. Toda, and M. Suzuki, "Local heat transfer on a combustion chamber wall of a spark-ignition engine," *SAE paper*, no. 931130, 1993.

[32] P. Gialber and P. Pinchon, "Measurements and multidimensional modelling of gas-wall heat transfer in S.I. engine," *SAE paper*, no. 880516, 1989.

[33] R. Prasad and N. K. Samria, "Transient heat transfer analysis in an internal combustion engine piston," *Computers and Structures*, vol. 34, no. 5, pp. 787–793, 1990.

[34] Y. Enomoto, N. Kitahara, and M. Takai, "Heat losses during knocking in a four-stroke gasoline engine," *JSME Internaltional Journal*, vol. 37, no. 3, pp. 668–676, 1994.

[35] S. Kimura, M. Koike, Y. Matsui, and Y. Enomoto, "Effects of combustion chamber specifications and swirl ratio on transient heat transfer and combustion in a DI diesel engine," *Proceedings of the International Symposium (COMODIA) 94*, 1994.

[36] Y. Hagihara, F. Toda, S. Ohyagi, and H. Tsuji, "Surface temperature and wall heat flux in a spark-ignition engine under knocking and non-knocking conditions," *SAE paper*, no. 981795, pp. 369–378, 1989.

[37] X. Wang, P. Price, R. Stone, and D. Richardson, "Burn rate and instantaneous heat flux study of iso-octane, toluene and gasoline in a spray-guided direct-injection spark ignition engine." *SAE International*, no. 2008-01-0469, 2008.

[38] J. M. Desantes, A. J. Torregrosa, A. Broatch, and P. Olmeda, "Experiments on the influence of intake conditions on local instantaneous heat flux in reciprocating internal combustion engines," *Energy*, vol. 36, no. 1, pp. 60–69, 2011.

[39] Y. Enomoto, S. Furuhama, and K. Minakami, "Heat loss to combustion chamber wall of 4-stroke gasoline engine (1st report, heat loss to piston and cylinder)," *Bulletin of JSME*, vol. 28, no. 238, pp. 647–655, 1985.

[40] Y. Enomoto and S. Furuhama, "Heat loss into combustion chamber wall of 4-stroke gasoline engine (2nd report, heat loss into cylinder head, intake and exhaust valves)," *Bulletin of JSME*, vol. 29, no. 253, pp. 2196–2203, 1986.

[41] A. Sanli, A. Ozsezen, I. Kilicaslan, and M. Canakci, "The influence of engine speed and load on the heat transfer between gases and in-cylinder walls at fired and motored conditions of an IDI diesel engine," *Applied Thermal Engineering*, vol. 28, pp. 1395–1404, 2008.

[42] C. Depcik and D. Assanis, "A universal heat transfer correlation for intake and exhaust flows in a spark-ignition internal combustion engine," *SAE paper*, no. 2002-01-0372, 2002.

[43] B. Lawton, "Effect of compression and expansion on instantaneous heat transfer in reciprocating internal combustion engine," *Proc Instn Mech. Engrs*, vol. 201, no. A3, pp. 175–186, 1987.

[44] A. Mohammadi, M. Yaghoubi, and M. Rashidi, "Analysis of local convective heat transfer in a spark ignition engine," *International Communication in Heat and Mass Transfer*, vol. 35, pp. 215–224, 2008.

[45] A. R. Noori and M. Rashidi, "Computational fluid dynamics study of heat transfer in a spark-ignition engine combustion chamber," *Journal of Heat Transfer*, vol. 129, pp. 609–616, 2007.

[46] W. Annand, "Instantaneous heat transfer rates to the cylinder head surface of a small compression-ignition engine," *Proc Instn Mech Engrs*, vol. 185, no. 72, pp. 976–987, 1971.

[47] J. Dent and S. Suliaman, "Convective and radiative heat transfer in a high swirl direct injection diesel engine," *SAE paper*, no. 770407, 1977.

[48] G. Hohenberg, "Advanced approaches for heat transfer calculations," *SAE paper*, no. 790825, 1979.

[49] A. Wimmer and T. Sams, "Heat transfer to the combustion chamber and port walls of IC engines- measurement and prediction," *SAE paper*, no. 2000-01-0568, 2000.

[50] D. Buttsworth, "Transient response of an erodable heat flux gauge using finite element analysis," *Proc Instn Mech. Engrs*, vol. 216, no. D, pp. 701–706, 2002.

[51] D. Bendersky, "A special thermocouple for measuring transient temperatures," *Mechanical Engineering*, vol. 75, pp. 117–121, 1953.

[52] T. LeFeuvre, P. Myers, and O. Uyehara, "Experimental instantaneous heat fluxes in a diesel engine and their correlation," *SAE paper*, no. 690464, 1969.

[53] T. Oguri and T. Aizawa, "Radiant heat transfer in the cylinder of a diesel engine," *JARI Tech. Memo*, vol. 10, pp. 357–369, 1972.

[54] K. Sihling and G. Woschni, "Experimental investigation of the instantaneous heat transfer in the cylinder of a high speed diesel engine," *SAE paper*, no. 790833, 1979.

[55] M. Yoshida, Y. Harigaya, and K. Sato, "Variation of heat-flux through a combustion-chamber wall of prechamber type diesel engine (heat-flux

through piston crown, cylinder head, suction valve, exhaust valve, pre-combustion chamber and exhaust port wall)," *Bulletin of the JSME-Japan Society of Mechanical Engineers*, vol. 25, no. 201, pp. 426–437, 1982.

[56] P. Childs, J. Greenwood, and C. Long, "Heat flux measurement techniques," *Proceedings of the Institution of Mechanical Engineers, Part C: Journal of Mechanical Engineering Science*, vol. 213, no. 7, pp. 655–677, 1999.

[57] A. Guelhan, "Heat flux measurements in high enthalpy flows," *DTIC Document*, 2000.

[58] J. Yang and J. Martin, "Approximate solution - one-dimensional energy equation for transient, compressible, low mach number turbulent boundary layer flows," *Journal of Heat Transfer*, vol. 111, p. 619, 1989.

[59] Z. Han and R. Reitz, "A temperature wall function formulation for variable-density turbulent flows with application to engine convective heat transfer modelling," *International Journal of Heat and Mass Transfer*, vol. 40, no. 3, pp. 613–625, 1997.

[60] A. Amsden, "KIVA-3V: A block-structured KIVA program for engines with vertical or canted valves," Los Alamos National Lab., NM (United States), United States, Technical report LA 13313-MS, July 1997.

[61] D. Buttsworth, A. Agrira, R. Malpress, and T. Yusaf, "Simulation of instantaneous heat transfer in spark ignition internal combustion engines: unsteady thermal boundary layer modelling," *Journal of Engineering for Gas Turbines and Power*, vol. 133, p. 022802, 2011.

[62] F. M. White, *Viscous Fluid Flow.* McGraw-Hill in Mechanical Engineering, Second Edition, ISBN 0-07-069712-4, 1991.

[63] J. Anderson, *Modern compressible flow: with historical perspective.* McGraw-Hill, 1990, vol. 2.

[64] H. Park, D. Assanis, and D. Jung, "Development of an in-cylinder heat transfer model with compressibility effects on turbulent Prandtl number, eddy viscosity ratio and kinematic viscosity variation," *SAE Technical Paper*, pp. 01–0702, 2009.

[65] V. Yakhot, S. Orszag, and A. Yakhot, "Heat transfer in turbulent fluids-I. pipe flow," *International Journal of Heat and Mass Transfer*, vol. 30, no. 1, pp. 15–22, 1987.

[66] M. Molla, M. Salit, M. Bin, F. Megat Ahmed, and W. Asrar, "Intake valve modelling and study of the suction air pressure and volumetric efficiency in a four stroke internal combustion engine," *Suranaree J. Sci. Technol.*, vol. 12, no. 4, 2005.

[67] S. Churchill, "A reinterpretation of the turbulent Prandtl number," *Industrial and Engineering Chemistry Research*, vol. 41, no. 25, pp. 6393–6401, 2002.

[68] M. Jischa and H. Rieke, "About the prediction of turbulent Prandtl and Schmidt numbers from modeled transport equations," *International Journal of Heat and Mass Transfer*, vol. 22, no. 11, pp. 1547–1555, 1979.

[69] H. Myong, N. Kasagi, and M. Hirata, "Numerical prediction of turbulent pipe flow heat transfer for various Prandtl number fluids with the improved $k-\epsilon$ turbulence model," *JSME Int. J*, pp. 613–622, 1989.

[70] H. Graber, "Heat transfer in smooth tubes, between parallel plates, in annuli and tube bundles with exponential heat flux distributions in forced laminar or turbulent flow," *International Journal of Heat and Mass Transfer*, vol. 13, no. 11, pp. 1645 – 1703, 1970.

[71] W. Kays, "Turbulent prandtl number. Where are we?" *ASME Transactions Journal of Heat Transfer*, vol. 116, pp. 284–295, 1994.

[72] W. Kays, M. Crawford, and B. Weigand, *Convective heat and mass transfer*. McGrow-Hill, 1993.

[73] R. Notter and C. Sleicher, "A solution to the turbulent graetz problem-III fully developed and entry region heat transfer rates," *Chemical Engineering Science*, vol. 27, no. 11, pp. 2073–2093, 1972.

[74] A. Reynolds, "The prediction of turbulent Prandtl and Schmidt numbers," *International Journal of Heat and Mass Transfer*, vol. 18, no. 9, pp. 1055–1069, 1975.

[75] D. Wilcox, *Turbulence modelling for* CFD. DCW industries La Canada, CA, 1998, vol. 2.

[76] J. Smits, "Modelling of a fluid flow in an internal combustion engine," *Graduation report TU/e, Report number WVT*, 2006.

[77] S. Peng, L. Davidson, and S. Holmberg, "A modified low-Reynolds-number $k-\omega$ model for recirculating flows," *Journal of fluids engineering*, vol. 119, p. 867, 1997.

[78] J. Bredberg, "On two equation eddy-viscosity models," *Department of Thermo and Fluid Dynamics, Chalmers University of Technology, Göteborg, Sweden*, 2001.

[79] J. Bredberg, S. Peng, and L. Davidson, "An improved $k-\omega$ turbulence model applied to recirculating flows," *International journal of heat and fluid flow*, vol. 23, no. 6, pp. 731–743, 2002.

[80] J. Lumley, *Engines: an introduction*. Cambridge Univ Pr, 1999.

[81] R. Diwakar, "Assessment of the ability of a multidimensional computer code to model combustion in a homogeneous-charge engine," Society of Automotive Engineers, Inc., Warrendale, PA, Tech. Rep., 1984.

[82] D. Buttsworth, "Spark ignition internal combustion engine modelling using matlab," University of Southern Queensland, Technical report TR-2002-02, 2002.

[83] C. Ferguson, *Internal combustion engines, Applied thermosciences.* New York: John Wiley and Sons, 1986.

[84] C. Olikara and G. Borman, "Calculating properties of equilibrium combustion products with some applications to I.C. engines," *SAE Paper*, no. 750468, 1975.

[85] H. Olivier, "Thin film gauges and coaxial thermocouples for measuring transient temperatures," *Shock Wave Laboratory, RWTH Aachen, Germany*, 2009.

[86] Z. Barbouchi and J. Bessrour, "Turbulence study in the internal combustion engine," *Journal of Engineering and Technology Research*, vol. 1, no. 9, pp. 194–202, 2009.

Appendix A

Governing equations and the simulation model

In order to define the heat transfer rates from the gases to the combustion chamber walls during the combustion process, the heat transfer will be expressed as a function of the crank angle in terms of the heat loss from the burned and unburned gases [83] as follows:

$$dQ/d\theta = -\dot{Q}_1/\omega = (-\dot{Q}_b - \dot{Q}_u)/\omega \tag{A.1}$$

In this model the combustion gases are defined as two zones, burned and unburned,from which the heat transfer rates $\dot{Q}_b$ and $\dot{Q}_u$ are obtained respectively. The heat flux for both zones is expressed as a function of temperature:

$$\dot{Q}_b = h\ A_b\ (T_b - \ T_w) \tag{A.2}$$

$$\dot{Q}_u = \ h\ A_u\ (T_u - \ T_w) \tag{A.3}$$

A_b and A_u are the areas of burned and unburned gas respectively contacted with the cylinder walls. They can be calculated from the following equations.

$$A_b = \left(\frac{\pi\ b^2}{2} + \frac{4V}{b}\right)\ x^{\frac{1}{2}} \tag{A.4}$$

$$A_u = \left(\frac{\pi\ b^2}{2} + \frac{4V}{b}\right)\ \left(1 - \ x^{\frac{1}{2}}\right) \tag{A.5}$$

The above two equations are empirical functions that have the correct limits in the case of a cylinder where $x \to 0$ and when $x \to 0$. Where x is the mass fraction of the cylinder content, it can be presented as:

Before the ignition/compression, $x = 0$

During the combustion,

$$x = \frac{1}{2}\ \left\{1 - cos\left[\frac{\pi\ (\theta - \ \theta_s)}{\theta_b}\right]\right\} \tag{A.6}$$

Where θ is the crank angle at any angle of the cycle and θ_s and θ_b are the start and duration of combustion in crank angle degrees respectively.

The following two parameters are the mass and the volume at any angle of the cycle and they can be written as:

$$m = m_1\ exp\left[\frac{-C\,(\theta - \ \theta_1)}{\omega}\ \right] \tag{A.7}$$

m_1 is the initial mass at the start of compression. The cylinder volume can be given by:

$$V = \ V_0\left[1 + \ \frac{r-1}{2}\ \left\{1 - cos\theta + \ \frac{1}{\epsilon}\ \left[1 - \ \left(1 - \ \epsilon^2\ sin^2\theta\right)^{\frac{1}{2}}\right]\right\}\right] \tag{A.8}$$

The differential form of the first law of thermodynamics will be presented for a control volume encasing the cylinder content.

$$m\,\frac{du}{d\theta} + u\,\frac{dm}{d\theta} = \frac{dQ}{d\theta} - P\,\frac{dV}{d\theta} - \frac{\dot{m}_1\,h_1}{\omega} \tag{A.9}$$

The pressure and the temperature histories throughout the cycle are required to determine the average gas velocity and they are functions of the thermodynamic properties of the gases, hence those thermodynamic properties will be described as follows:

Two Matlab subroutines (FARG and ECP) were programmed to return the thermodynamic properties throughout the engine cycle, see ([82]). The energy of the system is assumed to be:

$$u = \frac{U}{m} = x\,u_b + (1-x)\,u_u \tag{A.10}$$

u_b is the energy of the burned gas at the temperature T_b and u_u is the energy of the unburned gas at the temperature T_u. The energy of the burned gas is expressed as a function of the temperature T_b and the pressure P,

$$u_b = u_b\,(T_b\ ,\ P) \tag{A.11}$$

and

$$\frac{du_b}{d\theta} = \frac{\partial u_b}{\partial T_b}\,\frac{dT_b}{d\theta} + \frac{\partial u_b}{\partial P}\,\frac{dP}{d\theta} \tag{A.12}$$

Substitution of the partial derivatives returned by the subroutine ECP [83] the

above equation becomes:

$$\frac{du_b}{d\theta} = \left(c_{pb} - \frac{Pv_p}{T_b}\frac{\partial \ln v_b}{\partial \ln T_b}\right)\frac{dT_b}{d\theta} - v_b\left(\frac{\partial \ln v_b}{\partial \ln T_b} + \frac{\partial \ln v_b}{\partial \ln P}\right)\frac{dP}{d\theta} \tag{A.13}$$

And for the unburned gases

$$\frac{du_u}{d\theta} = \left(c_{pu} - \frac{Pv_u}{T_u}\frac{\partial \ln v_u}{\partial \ln T_u}\right)\frac{dT_u}{d\theta} - v_u\left(\frac{\partial \ln v_u}{\partial \ln T_u} + \frac{\partial \ln v_u}{\partial \ln P}\right)\frac{dP}{d\theta} \tag{A.14}$$

Equation (A.10) can be expressed in the derivatives form as:

$$m\frac{du}{d\theta} = \left[x\frac{du_b}{d\theta} + (1-x)\frac{du_u}{d\theta} + (u_b - u_u)\frac{dx}{d\theta}\right]m \tag{A.15}$$

Substituting the equations (A.13 and A.14) into the above equation gives:

$$\begin{aligned} m\frac{du}{d\theta} = {} & mx\left(c_{pb} - \frac{Pv_p}{T_b}\frac{\partial \ln v_b}{\partial \ln T_b}\right)\frac{dT_b}{d\theta} + m(1-x)\left(c_{pu} - \frac{Pv_u}{T_u}\frac{\partial \ln v_u}{\partial \ln T_u}\right)\frac{dT_u}{d\theta} \\ & - \left[mxv_b\left(\frac{\partial \ln v_b}{\partial \ln T_b} + \frac{\partial \ln v_b}{\partial \ln P}\right) + m(1-x)v_u\left(\frac{\partial \ln v_u}{\partial \ln T_u} + \frac{\partial \ln v_u}{\partial \ln P}\right)\right]\frac{dP}{d\theta} \\ & + m(u_b - u_u)\frac{dx}{d\theta} \end{aligned} \tag{A.16}$$

The above equation represents the first term on the left hand side of the equation (A.9). The same approach will be followed to define the specific volume of the system where the specific volume is expressed as a function of the temperature and the pressure.

$$v_b = v_b(T_b, P) \tag{A.17}$$

$$v = \frac{V}{m} = x\, v_b + (1-x)\, v_u \tag{A.18}$$

The derivatives form of the above equation is given as:

$$\frac{dv_b}{d\theta} = \frac{\partial v_b}{\partial T_b}\frac{dT_b}{d\theta} + \frac{\partial v_b}{\partial P}\frac{dP}{d\theta} \tag{A.19}$$

Substituting of the partial derivatives returned by the subroutine ECP [83] into the above equation gives:

$$\frac{dv_b}{d\theta} = \frac{v_b}{T_b}\frac{\partial \ln v_b}{\partial \ln T_b}\frac{dT_b}{d\theta} + \frac{v_b}{P}\frac{\partial \ln v_b}{\partial \ln P}\frac{dP}{d\theta} \tag{A.20}$$

And for the unburned gases, the specific volume is expressed as follows:

$$\frac{dv_u}{d\theta} = \frac{v_u}{T_u}\frac{\partial \ln v_u}{\partial \ln T_u}\frac{dT_u}{d\theta} + \frac{v_u}{P}\frac{\partial \ln v_u}{\partial \ln P}\frac{dP}{d\theta} \tag{A.21}$$

The derivatives expression of the equation A.18 is given by:

$$\frac{1}{m}\frac{dV}{d\theta} - \frac{V}{m^2}\frac{dm}{d\theta} = x\frac{dv_b}{d\theta} + (1-x)\frac{dv_u}{d\theta} + (v_b - v_u)\frac{dx}{d\theta} \tag{A.22}$$

By substituting the equations A.20 and A.21 into the above equation gives:

$$\begin{aligned}\frac{1}{m}\frac{dV}{d\theta} + \frac{VC}{m\omega} = {} & x\frac{v_b}{T_b}\frac{\partial \ln v_b}{\partial \ln T_b}\frac{dT_b}{d\theta} + (1-x)\frac{v_u}{T_u}\frac{\partial \ln v_u}{\partial \ln T_u}\frac{dT_u}{d\theta} - \\ & \left[x\frac{v_b}{P}\frac{\partial \ln v_b}{\partial \ln P} + (1-x)\frac{v_u}{P}\frac{\partial \ln v_u}{\partial \ln P}\right]\frac{dP}{d\theta} + (v_b - v_u)\frac{dx}{d\theta}\end{aligned} \tag{A.23}$$

The entropy of the unburned gas is introduced into this analysis since the unburned gas is treated as an open system losing mass via leakage and during the

combustion. The equation relating the entropy to the temperature and pressure is given by:

$$s_u = s_u(T_u, P) \tag{A.24}$$

From the above equation the derivatives form is:

$$\frac{ds_u}{d\theta} = \left(\frac{\partial s_u}{\partial T_u}\right)\frac{dT_u}{d\theta} + \left(\frac{\partial s_u}{\partial P}\right)\frac{dP}{d\theta} \tag{A.25}$$

Substituting the partial derivatives returned by the subroutine FARG [83] into the above equation yields:

$$\frac{ds_u}{d\theta} = \left(\frac{c_{pu}}{T_u}\right)\frac{dT_u}{d\theta} - \frac{v_u}{T_u}\,\frac{\partial \ln v_u}{\partial \ln T_u}\frac{dP}{d\theta} \tag{A.26}$$

To define the first term on the right hand side of equation A.9 (work term), the enthalpy of the mass loss due to blowby needs to be specified [83]. The unburned gas leaks past the rings in the early stage of the combustion process, and in the late stage the burned gas leaks past the rings. Those leaks need to be considered in order to accurately perform the calculations. The relationship between the enthalpy of unburned and burned gases can be presented in the presence of the mass fraction as follows:

$$h_l = \left(1 - x^2\right) h_u + x^2 h_b \tag{A.27}$$

The functional form of the enthalpy of unburned and burned gases will be followed respectively,

$$h_u = h_u(T_u, P) \tag{A.28}$$

$$h_b = h_b(T_b, P) \tag{A.29}$$

They are computed by subroutines FARG and ECP for unburned and burned gases respectively [83], and the values will be returned for the further calculations throughout the engine cycle.

Appendix B

Calibration

B.1 Pressure transducer calibration curve

This appendix presents the calibration curve for the PCB piezoelectric pressure transducer. This pressure transducer was calibrated in the laboratories of the University of Southern Queensland, using a dead weight tester. The pressure transducer was installed in the dead weight tester and calibrated using a Bruel & Kjaer charger amplifier. The large input resistance of the charge amplifier makes it suitable to calibrate this type of pressure transducers. A LabVIEW data acquisition program was used to record the voltage signals provided by the charge amplifier, which will be used to make the calibration curve, along with pressure values from the tester. An oscilloscope was also used to monitor the change in the pressure during the test. The calibration range of the pressure is between 10-90 psi.

After the preliminary installation and setting up of the system were completed, the dead weight tester was loaded with known weights. Those weights provide a hydraulic pressure on the pressure transducer which gives voltage output signals. The voltage values corresponding to known pressure values were collected. Those

voltage values were then used to make a plot versus the known pressure applied. The best fitting straight line was then drawn through the points and the slope of the line gave the sensitivity of the pressure transducer. A linear relationship between the pressure and the voltage was resulted from this calibration, see figure B.1 and the following formula was obtained:

$$P = C_1 V + C_2 \tag{B.1}$$

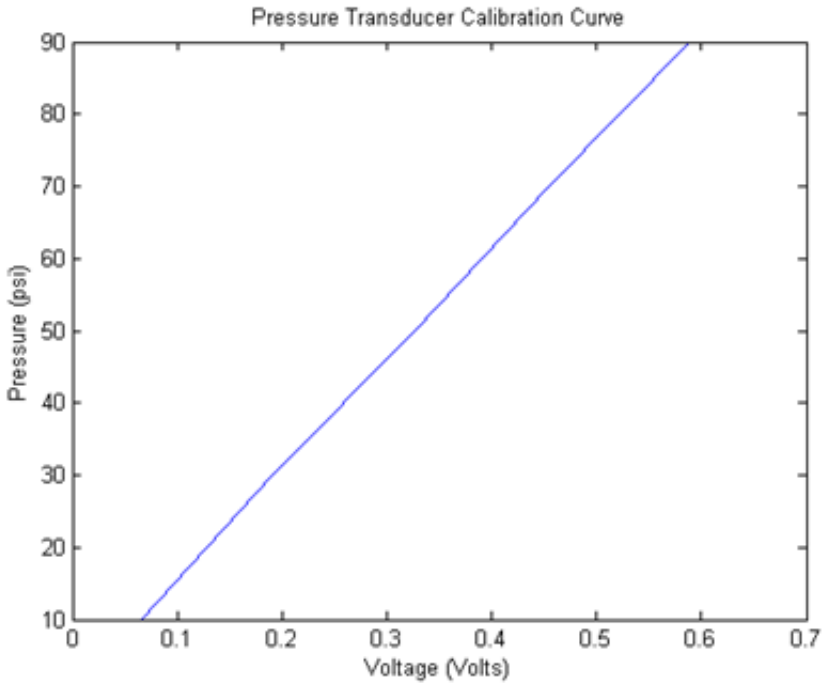

Figure B.1: Pressure transducer calibration curve.

Where P is the pressure, C_1 is calibration constant (the slope of the curve), V is the voltage readings in volt and C_2 is the intercept of the curve on the pressure axis.

B.2 Thermocouple calibration

This section presents the calibration process of the E-type coaxial thermocouple used in this study. This calibration was conducted in the laboratories of the University of Southern Queensland, using the hot water bath technique. The fabricated thermocouple was placed into a hot water bath at about 55°C. The thermocouple probe was connected to the multimeter to record the change in the voltage output from the thermocouple, according to the change in the water temperature. The water was then left to cool down and the temperature values were recorded from the thermometer, along with the output voltage values from the multimeter. Based on this measurement, the output was found to be 62.5 mV/°C which is about 9 % lower than the standard value of this type of thermocouple (68 mV/°C). The collected set of data was then used to plot the calibration curve. The temperature values and the output voltage readings from the calibration are presented in the table below.

Change in water temperature (°C)	Voltage output (mV)
52	1.9
41	1.16
35	0.803
31.5	0.59
29	0.423
26	0.25

Table B.1: Thermocouple calibration